Preparation and Applications of Macroscopic Metal-Organic Framework Materials

DISSERTATION

zur Erlangung des akademischen Grades einer Doktorin

der Naturwissenschaften (Dr. rer. nat.)

in der Bayreuther Graduiertenschule für Mathematik und

Naturwissenschaften (BayNAT)

der Universität Bayreuth

vorgelegt von

Yingying Du

Lingyuan City, Liaoning Province, China

Bayreuth, August 2024

The doctoral thesis was prepared at the chair of Macromolecular Chemistry II at the University of Bayreuth from 12/2020 until 08/2024 and was supervised by Prof. Dr. Seema Agarwal.

This is a full reprint of the thesis submitted to obtain the academic degree of Doctor of Natural Sciences (Dr. ret. nat.) and approved by the Bayreuth Graduate School of Mathematical and Natural Sciences (BayNAT) of the University of Bayreuth.

From of the dissertation: cumulative dissertation

Date of submission: 27.08.2024

Admission by the executive board: 11.09.2024

Date of defense: 06.11.2024

Acting director: Prof. Dr. Jürgen Köhler

Doctoral committee:

Prof. Dr. Seema Agarwal (reviewer)

Prof. Dr. Shoubhik Das (reviewer)

Prof. Dr. André Gröschel (chair)

Prof. Dr. Anna Schenk

This is a cumulative dissertation with the following list of publications:

(1) Yingying Du, Chenhui Ding, Chao Deng, Susanta Banerjee, Seema Agarwal. In-situ constructed magnetic core-shell (hydrogen-bonded organic framework-on-metal-organic framework) structure: an efficient catalyst for peroxymonosulfate activation.

Manuscript ready for submission.

Discussion in **section 2.1**, reprinted in **section 4.1**.

(2) Yingying Du, Chenhui Ding, Jana Timm, Roland Marschall, Seema Agarwal. Template-assisted Preparation of Self-standing 2D-MOF Membranes for Application in Cascade Reactions. ChemCatChem, **2022**, 14(22), e202201040.
DOI: 10.1002/cctc.202201040

Discussion in **section 2.2**, reprinted in **section 4.2**.

(3) Yingying Du, Chenhui Ding, Seema Agarwal. Sustainable Hierarchically Porous Reusable Metal-Organic Framework Sponge as a Heterogeneous Catalyst and Catalytic Filter for Degradation of Organic Dyes. Advanced Energy and Sustainability Research, **2023**, 5(4), 2300218.
DOI: 10.1002/aesr.202300218

Discussion in **section 2.3**, reprinted in **section 4.3**.

Other peer-reviewed publications originated during this time but were not a part of the cumulative thesis:

(1) Chenhui Ding, **Yingying Du**, Seema Agarwal. Open-Cell Robust COF-Nanowire Network Sponges as Sustainable Adsorbent and Filter. Advanced Functional Materials, **2023**, 34(3), 2309938.
DOI: 10.1002/adfm.202309938

(2) Chenhui Ding, **Yingying Du**, Tamara Fischer, Jana Timm, Roland Marschall, Jürgen Senker, Seema Agarwal. Self-standing flexible large-sized covalent organic framework hollow fiber membranes.
Manuscript ready for submission.

Table of Contents

List of Symbols and Abbreviations

MOFs	Metal-organic frameworks
SBUs	Secondary building units
UiO	University of Oslo
ZIF	Zeolite imidazolate framework
NU	Northwestern university
MIL	Materials of institute Lavoisier
IRMOF	Iso-reticular metal-organic framework
HKUST	Hong Kong university of science and technology
0D	Zero-dimensional
1D	One-dimensional
2D	Two-dimensional
3D	Three-dimensional
Al	Aluminium
Cr	Chromium
Mn	Manganese
Fe	Iron
Co	Cobalt
Zn	Zinc
Cu	Copper
Eu	Europium
Nd	Neodymium
Zr	Zirconium
SOD	Sodalite
C	Carbon
H	Hydrogen
S	Sulfur
N	Nitrogen

List of Symbols and Abbreviations

O	Oxygen
Cl	Chlorine
NH_2	Amine
NO_2	Nitrogen dioxide
Br	Bromine
H_3BTTri	1,3,5-tris(1H-1,2,3-triazol-5-yl)benzene
$CuCl_2 \cdot 2H_2O$	Copper(II) chloride dihydrate
DMF	Dimethylformamide
HCl	Hydrochloric acid
MIP	Materials of the institute of porous materials
H_4mdip	3,3′,5,5′-tetracarboxydiphenylmethane
HNO_3	Nitric acid
H_2SO_4	Sulfuric acid
H_3PO_4	Phosphoric acid
NH_4OH	Ammonium hydroxide
KOH	Potassium hydroxide
DEF	Diethyl formamide
NMP	1-methyl-2-pyrrolidone
DMSO	Dimethyl sulfoxide
H_2BDC	1,4-benzene dicarboxylate
HSAB	Hard and soft acids and bases
MHT	Modulated hydrothermal
LbL	Layer-by-layer
ATA	Amino terephthalic acid
$ZrCl_4$	Zirconium tetrachloride
ALD	Atomic layer deposition
Al_2O_3	Aluminum oxide
ZnO	Zinc oxide
TiO_2	Titanium dioxide

List of Symbols and Abbreviations

PP	Polypropylene
BET	Brunauer-Emmett-Teller
CWAs	Chemical warfare agents
CF	Cotton fabric
PU	Polyurethane
PS	Polystyrene
PAN	Polyacrylonitrile
PVP	Poly(vinyl pyrrolidone)
PVDF	Poly(vinylidene fluoride)
H_3BTC	1, 3, 5-tricarboxylic acid
$FeCl_3$	Iron(III) chloride
$Co(acac)_2$	Cobalt(II) acetylacetonate
2-MeIM	2-methyl imidazole
$Co(NO_3)_2 \cdot 6H_2O$	Cobalt(II) nitrate hexahydrate
CNT	Carbon nanotube
MAH	Maleic anhydride
CS	Cellulose sponge
CNF	Cellulose nanofiber
NF	Nickel foam
DCM	Dichloromethane
PE	Polyethylene
PLA	Poly(lactic acid)
CO_2	Carbon dioxide
TON	Turnover number
H_3TCBA	Tris(3-carboxy biphenyl)amine
PET	Poly(ethylene terephthalate)
MB	Methylene blue
U	Uranium
AO	Amidoxime

List of Symbols and Abbreviations

PCN	Porous coordination network
MO	Methyl orange
PMS	Peroxymonosulfate
Rh B	Rhodamine B
Fe_3O_4	Iron oxide
HOF	Hydrogen-bonded organic framework
$BDC-NH_2$	2-aminobenzenedicarboxylic acid
$BDC-SO_3Na$	2-sulfobenzenedicarboxylic acid monosodium salt
COF	Covalent organic framework
AuNPs	Gold nanoparticles
SR-AOPs	Sulfate radical based advanced oxidation processes
MeOH	Methanol
TBA	Tert-butanol
FFA	Furfuryl alcohol
NaN_3	Sodium azide
KI	Potassium iodide
NaOH	Sodium hydroxide
MB	Methylene blue
TC	Tetracycline
BPA	Bisphenol A
$\cdot OH$	Hydroxyl radical
$SO_4^{\cdot-}$	Sulfate radical
PS	Persulfate
Co_3O_4	Tricobalt tetraoxide
TEMP	2, 6, 6-tetramethyl-4-piperidone
DMPO	5, 5-dimethyl-1-pyrroline
DMPOX	5,5-dimethyl-2-oxo-pyrrolidine-1-oxy
H_4TNAPy	4,4',4'',4'''-(Pyrene-1,3,6,8-tetrayl)tetrabenzoic acid
Mn_3O_4	Manganese oxide

List of Symbols and Abbreviations

PI	Polyimide
GC	Gas chromatography
ICP-OES	Inductively coupled plasma-optical emission spectrometry
VSM	Vibrating sample magnetometer
EIS	Electrochemical impedance spectroscopy
TEM	Transmission electron microscopy
SEM	Scanning electron microscopy
XRD	X-ray diffraction
FT-IR	Fourier-transform infrared spectroscopy
EPR	Electron paramagnetic resonance
HPLC-Ms	High-performance liquid chromatography-mass spectrometry
wt%	Weight percent
r.t.	Room temperature
°C	Degrees celsius
μm	Micrometer
nm	Nanometer
kPa	Kilopascal
h	Hour
min	Minute
$m^2\ g^{-1}$	Square meters per gram
K	Kelvin
%	Percent
$g\ cm^{-3}$	Grams per cubic centimeter
Mw	Molecular weight
mmol	Millimole
mM	Millimoles per liter
mL	Milliliter

List of Symbols and Abbreviations

mg L^{-1}	Milligrams per liter
min^{-1}	Per minute
mg g^{-1}	Milligrams per gram
g	Gram
L	Liter
pH	Potential of hydrogen
Å	Angstrom

Summary/Zusammenfassung

Summary

In the past two decades, metal-organic frameworks (MOFs), as a new class of porous crystalline materials, have had a significant impact in catalysis, environmental science, biomedicine, energy storage, and other fields due to their large specific surface area, diversified structure, and adjustable porosity characteristics. However, the insolubility associated with MOF powder form, and processing challenges make their recovery difficult and greatly hinder their practical application. Therefore, the aim of my work is to develop reproducible methods to create zero-dimensional (0D), one/two-dimensional (1D/2D), and three-dimensional (3D) functional macroscopic MOF materials that can be reused and easily separated from the reaction medium after use. A proof of concept demonstrated its applicability as a catalyst for multiple uses in a one-pot reaction and water purification.

0D MOF particles are widely used, especially as catalysts, because of their larger specific surface area, favorable for abundant ion adsorption, high exposure of active sites, and short ion transport distances. The core-shell structure is one of the main methods for constructing functional 0D MOF particles. Although many methods for preparing core-shell structures have been developed in recent years, it is still a great challenge to prepare 0D MOF particles with high accessibility and recyclability. Therefore, in my work, the magnetic core-shell hydrogen-bonded organic framework (HOF)-on-MOF catalyst was successfully prepared through a simple solvothermal method, using MOF as the core, incorporating magnetic Fe_3O_4, and porous crystalline HOF as the shell. The crystalline porous HOF shell minimizes mass transfer restrictions and protects the active site. This work effectively addresses the limitations of the traditional core-shell structure, where the core serves as a catalyst and the shell primarily acts as protection, leading to a limited number of active catalytic sites.

Compared with 0D MOF particles, 2D membranes are easier to handle and have higher

accessibility in practical applications. However, preparing structurally stable and self-standing MOF membranes remains a significant challenge. Based on the electrospinning process, two kinds of independent self-standing MOF membranes with different functions (acid and base functionalities) have been successfully prepared by the template-assisted method. This is done by growing MOFs on a 2D electrospun polymer template membrane. Subsequent removal of the template polymer provides self-standing, highly stable MOF membranes with hollow fibers. These membranes are used as acid-base catalysts in a teabag-style one-pot cascade reaction. After use, the membranes can be easily removed and reused for several cycles without losing efficiency.

Furthermore, a mechanically stable, hierarchically porous 3D MOF sponge was successfully prepared by growing the MOF in situ on a polymer sponge, which was itself created by self-assembly of short electrospun fibers during freeze-drying. The resulting 3D MOF sponge possesses a hierarchically porous structure, high porosity, and substantial pore volume, enabling efficient water flux and enhanced mass transfer between molecules in the solution. Owing to these advantageous characteristics, the prepared 3D MOF sponge demonstrated excellent practicality and recyclability as a filter for the continuous removal of organic model pollutants from water.

The findings from this study have been successfully published in two peer-reviewed journals (ChemCatChem, 2022, 14(22), e202201040; Advanced Energy and Sustainability Research, 2023, 5(4), 2300218), and a third manuscript is currently prepared and ready for submission.

Zusammenfassung

In den letzten zwei Jahrzehnten hatten metallorganische Gerüste (MOFs) als neue Klasse poröser kristalliner Materialien aufgrund ihrer großen spezifischen Oberfläche erhebliche Auswirkungen auf die Katalyse, die Umweltwissenschaften, die Biomedizin, die Energiespeicherung und andere Bereiche durch ihre abwechslungsreiche Struktur und einstellbare Porositätseigenschaften. Allerdings erschwert die mit MOF-Partikelpulvern verbundene Unlöslichkeit, und die Herausforderungen bei der Verarbeitung ihre Gewinnung und behindern ihre praktische Anwendung erheblich. Ziel meiner Arbeit ist daher die Entwicklung reproduzierbarer Methoden zur Herstellung nulldimensionaler (0D), ein-/zweidimensionaler (1D/2D) und dreidimensionaler (3D) funktionaler makroskopischer MOF-Materialien, die wiederverwendet und nach dem Gebrauch wieder leicht vom Reaktionsmedium getrennt werden können. Ein Machbarkeitsnachweis demonstrierte seine Anwendbarkeit als Katalysator für vielfältige Anwendungen in einer Eintopfreaktion und zur Wasserreinigung.

0D MOF-Partikel werden häufig verwendet, insbesondere als Katalysatoren, da sie eine größere Oberfläche haben, die eine reichliche Ionenadsorption begünstigt, eine hohe Exposition aktiver Zentren besitzt und kurze Ionentransportentfernungen aufweist. Die Kern-Schale-Struktur ist eine der Hauptmethoden zum Aufbau funktioneller 0D MOF Partikel. Obwohl in den letzten Jahren viele Methoden zur Herstellung von Kern-Schale-Strukturen entwickelt wurden, ist es immer noch eine große Herausforderung 0D MOF-Partikel mit hoher Zugänglichkeit und Recyclingfähigkeit herzustellen. Daher wurde in meiner Arbeit der magnetische Kern-Schale-Katalysator mit wasserstoffgebundenem organischem Gerüst (HOF) auf MOF erfolgreich durch eine einfache Solvothermalmethode hergestellt, wobei MOF als Kern, magnetisches Fe_3O_4 und poröses kristallines HOF als Schale verwendet wurden. Die kristalline poröse HOF-Hülle minimiert Stofftransportbeschränkungen und schützt das aktive Zentrum. Diese Arbeit befasst sich effektiv mit den Einschränkungen der traditionellen Kern-Schale-Struktur, bei der der Kern als Katalysator und die Schale in erster Linie als

Summary/Zusammenfassung

Schutz fungiert, was zu einer begrenzten Anzahl aktiver katalytischer Zentren führt.

Im Vergleich zu 0D MOF Partikeln sind 2D Membranen einfacher zu handhaben und in praktischen Anwendungen besser zugänglich. Die Herstellung strukturell stabiler und eigenständig stehender MOF-Membranen bleibt jedoch eine große Herausforderung. Basierend auf dem Elektrospinning-Prozess wurden zwei Arten eigenständig stehender MOF-Membranen mit unterschiedlichen Funktionen (Säure- und Basenfunktionalitäten) erfolgreich durch eine templatunterstützte Methode hergestellt. Dies geschieht durch das Züchten von MOFs auf einer 2D elektrogesponnenen Polymer-Templatmembran. Durch die anschließende Entfernung des Templatpolymers entstehen selbststehende, hochstabile MOF-Membranen mit Hohlfasern. Diese Membranen werden als Säure-Base-Katalysatoren im Teebeutel-Stil in einer Eintopf-Kaskadenreaktion eingesetzt. Nach dem Gebrauch können die Membranen problemlos entfernt und für mehrere Zyklen wiederverwendet werden, ohne dass Effizienz verloren geht.

Darüber hinaus wurde ein mechanisch stabiler, hierarchisch poröser 3D MOF-Schwamm erfolgreich hergestellt, indem das MOF in situ auf einem Polymerschwamm gezüchtet wurde, der seinerseits durch Selbstorganisation kurzer elektrogesponnener Fasern während der Gefriertrocknung entstand. Der resultierende 3D MOF-Schwamm besitzt eine hierarchisch poröse Struktur, eine hohe Porosität und ein beträchtliches Porenvolumen, was einen effizienten Wasserfluss und einen verbesserten Stofftransfer zwischen Molekülen in der Lösung ermöglicht. Aufgrund dieser vorteilhaften Eigenschaften zeigte der hergestellte 3D MOF-Schwamm eine hervorragende Praktikabilität und Recyclingfähigkeit als Filter für die kontinuierliche Entfernung organischer Modellschadstoffe aus Wasser.

Die Ergebnisse dieser Studie wurden erfolgreich in zwei von Experten begutachteten Fachzeitschriften veröffentlicht (ChemCatChem, 2022, 14(22), e202201040; Advanced Energy and Sustainability Research, 2023, 5(4), 2300218), und ein drittes Manuskript ist derzeit vorbereitet und zur Einreichung bereit.

1. Introduction

1.1 Motivation

With the development and progress of modern society, porous materials play an indispensable role in our daily lives. From structural materials to functions, they have covered various fields such as adsorption, catalysis, biomedicine, and energy.[1-5] Metal-organic frameworks (MOFs), also known as porous coordination polymers, are an emerging class of porous crystalline materials, with a periodic network structure formed by inorganic metal centers (metal clusters/metal ions) and bridging organic ligands connected through self-assembly.[6-10] Since Prof. Yaghi[11] first proposed the concept of MOFs in the 1990s, the field has attracted significant attention and developed rapidly. Over the past two decades, thousands of articles about MOFs have been published annually (**Figure 1-1**). Compared with traditional porous materials, MOFs offer diverse structures (with more than 80,000 reported so far), high specific surface areas (up to 10,000 m^2 g^{-1}), high porosity (up to 90%), and multi-functionality.[12-15] These properties have had a significant impact on various fields, such as chemistry, physics, biology, and materials science. The production scale of some MOFs has even reached industrial levels.[16-17]

Despite all their advantages, the industrial application of MOFs in powder form is restricted. Converting brittle MOF crystals into stable, robust, and flexible usable forms such as membranes, films, or composites without losing their intrinsic properties is challenging and requires innovative approaches. Additionally, recycling is limited when MOF powders are used.[18-21] In order to make full use of the advantages of MOFs and overcome the shortcomings of their powder form, it is considered a feasible strategy to construct microcrystalline MOF materials into macroscopic structures.[22-27] This is the topic of my research.

In this chapter, the characteristics, types and synthesis methods of MOFs are introduced in detail. Next, the construction strategies of macroscopic MOF materials are discussed. Finally, the new topics and future development directions of this field are prospected.
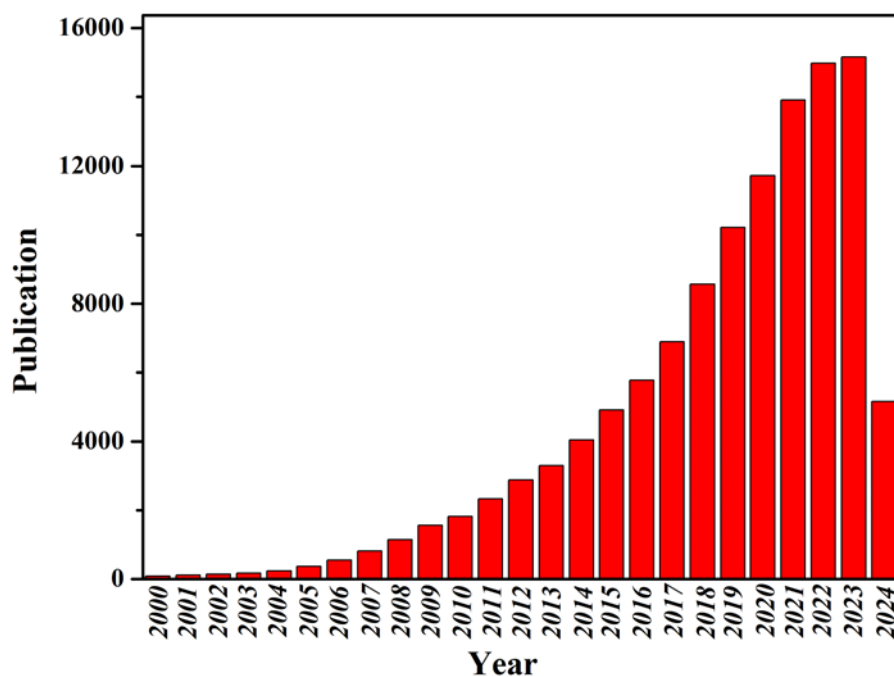
Figure 1-1. Articles published annually from 01. 2000 to 06. 2024. The keyword used is metal-organic frameworks. (Web of Science database)

1.2 Introduction to MOFs

1.2.1 Characteristics of MOFs

In the structure of MOFs, there are both organic ligands and metal centers. The organic ligands act as "backbones" in the MOF structure, while the metal centers are regarded as inorganic secondary building units (SBUs), which act as "joints" in the structure (**Figure 1-2**).[28] Generally speaking, by selecting appropriate inorganic metal centers and organic ligands, and rationally designing the topology (assembly method), the framework structure, channel environment, and functionality can be finely adjusted. This provides MOF crystal materials with many unique physical and chemical properties, such as diverse structures, large specific surface areas, and high porosity.
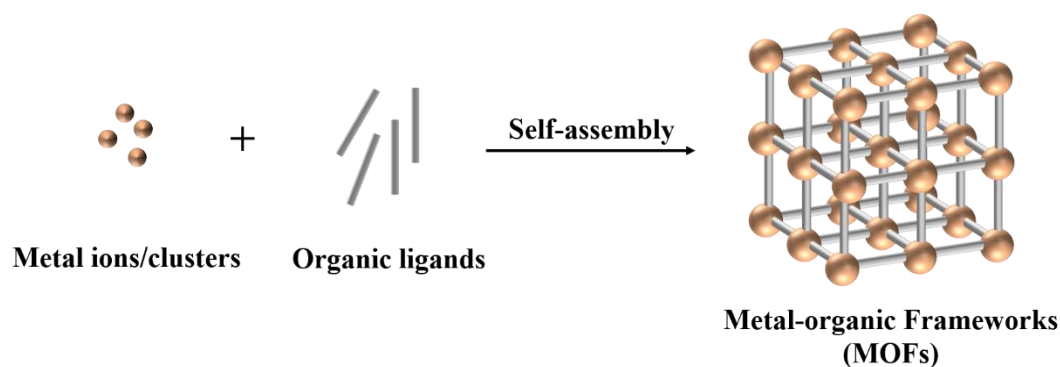
Figure 1-2. Schematic representation of MOFs.

a) Diverse structures

A wide variety of metal ions complex and changeable organic ligand arrangements, and flexibility of synthesis strategies jointly create the diversity of MOF material structures. Most main group metal elements, some transition metal elements, alkaline earth metal elements, and lanthanide metal elements have been selected to synthesize MOF materials.[29-31] Common metal centers include transition elements such as aluminum (Al), chromium (Cr), manganese (Mn), iron (Fe), cobalt (Co), zinc (Zn) and copper (Cu), and rare earth elements such as europium (Eu) and neodymium (Nd).[32-36] **Figure 1-3a** shows the commonly used metal SBUs.[37] The coordination configuration of different metal ions is different. Its coordination configuration is not only determined by its electronic structure, but also by the type, size, shape, and concentration of the ligands.[38] The same organic ligands combined with different metal ions can also synthesize MOF materials with varying crystal structures. For example, using 1,4-benzene dicarboxylate (H$_2$BDC) as an organic ligand with different metal ions such as Zr^{4+}, Fe^{3+}, and Zn^{2+}, it is possible to create various distinct crystal morphologies, such as regular octahedrons, hexagonal prisms, and rhombohedral dodecahedrons.[39-41]

Figure 1-3. Some representative (a) metal SBUs, and (b) organic ligands for MOFs. Reprinted with permission from ref. [37]. Copyright (2019) Elsevier.

Common organic ligands include oxygen-containing and nitrogen-containing ligands, including carboxylic acids, imidazole, and pyridines (**Figure 1-3b**).[37] The structure and physical properties of MOF materials can also be influenced to varying degrees by using the same metal ion while introducing different functional groups (such as hydroxyl, amino, sulfonic acid, halogen, etc.) into the organic ligand or by increasing

the number of benzene rings in the organic ligand.

For example, Cavka's research group[42] synthesized a series of UiO-66 (UiO stands for University of Oslo) structures centered on Zr by changing the length of the ligand. The results show that as the length of the ligand increases, the specific surface area of UiO-X increases from 1187 to 4170 m^2 g^{-1}, and the pore size of the UiO-X also increases from 6 angstroms (Å) to 10Å. The following year, Kandiah et al.[43] used Zr as the center and synthesized a series of UiO-66-X (X is -NH_2, -NO_2, -Br) extended structures with different functionalities by adjusting the substituents on the ligand benzene ring. In addition, with the same metal center and organic ligands, MOF materials with different topological structures and properties can be obtained by adjusting parameters such as raw material ratio, solvent type, synthesis temperature, pH value of solution, and reaction time during the synthesis process.[44-45]

b) High specific surface area and porosity

Compared with the pore structure of traditional porous materials, MOFs have a spatial structure constructed by metal nodes and organic ligands like a scaffold, so it has no wall structure. This structure allows MOFs to have higher specific surface area, pore volume, and lower density. There are often unreacted solvent small molecules in the pores of synthesized MOF materials, which can be removed through activation methods such as washing, purification, and vacuum drying so that MOFs can form a porous structure with larger porosity.[46-48] In 2010, Furukawa et al.[49] synthesized MOF-200, which had a pore volume of 90 % of the crystal volume, resulting in the lowest crystal density for a porous material (0.22 g cm^{-3}). Furthermore, the pore sizes in MOFs can range from a few Å to tens of nanometers (nm), and the same material can have pores of different sizes, both in microscale and mesoscale regions.[50-51] The porous structure and small particle size provide MOF materials with a large specific surface area, making them highly advantageous for applications in catalysis, gas adsorption and storage, gas separation, and many other fields.[52-55]

It is well known that the maximum specific surface area of zeolite materials is 904 m^2 g^{-1}, and that of activated carbon materials is 2030 m^2 g^{-1}.[56-57] In contrast, MOF materials exhibit an exceptionally large specific surface area. In 2012, Farha et al.[58]

synthesized NU-110E (NU stands for Northwestern University) MOF achieving a specific surface area as high as 7140 m^2 g^{-1}. The theoretical upper limit of the MOF surface area, measured by the Langmuir method, is about 14600 m^2 g^{-1}, or even higher.

c) Chemical and thermal stability

MOFs also show excellent chemical and thermal stability. For example, MIL-101(Al) (MIL stands for materials of institute Lavoisier) synthesized by Serra-Crespo et al. has high thermal and chemical stability and will only decompose in the air at temperatures above 650 K.[59] The triazole-based bridged framework Cu-BTTri MOF (reaction of $CuCl_2 \cdot 2H_2O$ with 1,3,5-tris(1H-1,2,3-triazol-5-yl)benzene (H_3BTTri) in dimethylformamide (DMF) at 100 °C) reported by Demessence et al.[60] showed excellent stability after being soaked in boiling water for 3 days or in hydrochloric acid (HCl) solution (pH = 3) for 1 day. Wang and co-workers obtained macro-porous MOF MIP-200 (MIP stands for materials of the institute of porous materials from Paris) via a reaction of Zr^{4+} and 3,3′,5,5′-tetracarboxydiphenylmethane (H_4mdip) that shows excellent stability under extremely harsh conditions such as concentrated acids (HCl and nitric acid (HNO_3)), high concentrations of phosphoric acid (H_3PO_4) and sulfuric acid (H_2SO_4), and ammonium hydroxide (NH_4OH) vapor.[61] Lu and co-workers synthesized the metal azolate framework MAF-X27-Cl, which can maintain its original crystalline state for at least 1 week in acidic (0.001 M HCl) or strongly alkaline (1.0 M potassium hydroxide (KOH)) solutions.[62] Stable MOF structures can be rationally designed based on the hard and soft acids and bases (HSAB) theory. For example, carboxylate-based ligands of hard bases can form stable MOFs with high-valent metal ions (hard acids, Ti^{4+}, Zr^{4+}, Al^{3+}, Fe^{3+}, and Cr^{3+}).[63-65] Similarly, the assembly of soft azole ligands (such as imidazole, pyrazole, triazole, and tetrazole) and soft divalent metal ions (such as Zn^{2+}, Cu^{2+}, Ni^{2+}, Mn^{2+}, and Ag^+) can also form a stable MOF framework.[66-67]

1.2.2 Typical MOF series

So far, more than tens of thousands of MOFs have been synthesized. Among them,

1. Introduction

IRMOF (iso-reticular metal-organic framework, refers to a series of MOFs with the same network topology but different pore sizes)[68], MIL (a class of porous metal carboxylate composed of different trivalent metal cations such as iron (III), aluminum (III), gallium (III), indium (III), vanadium (III) and chromium (III) with carboxylic acid ligands),[69-70] UiO, and ZIF (zeolite imidazolate framework) series are the most typical. Below I will introduce the typical MOF materials that I used in my research work.

a) UiO series

Among the many subclasses of MOFs, the UiO family (UiO-66, UiO-67, UiO-68) is cited most frequently. They are three-dimensional porous materials composed of Zr^{4+} and dicarboxylic acid, the most representative of which is UiO-66. Other UiOs are derived from the UiO-66 network.[71] MOFs based on zirconium clusters have received widespread attention since Cavka's research group at the University of Oslo first reported a Zr-MOF (molecular formula: $Zr_6O_4(OH)_4(BDC)_6$) in 2008. Compared with other MOFs, UiO-66 has extremely high stability. UiO-66 can remain stable in solvents such as water, DMF, benzene, or acetone, and has strong acid resistance and certain alkali resistance. In addition, its crystal structure can remain intact till about 500 °C. [42] The reason UiO-66 is so stable is that the cubic octahedral structure of the metal cluster provides 12 extension sites for coordination with terephthalic acid, which is the highest coordination number among MOFs.[72-73]

In addition, another attractive aspect of the UiO series is that it has a wide range of structures without requiring major changes to the synthesis program. For example, in 2013, Biswas et al.[74] synthesized a novel functionalized UiO-66-X framework (X = -SO_3H, -CO_2H, -I), using three linking groups containing BDC-X (BDC:1,4-benzene dicarboxylate). In 2014, Hu et al.[75] prepared a series of amino-functionalized Zr-MOFs through solvothermal synthesis, whose ideal structural formula is Zr_6O_4 $(OH)_4(BDC)_6$-6X$(ABDC)_6$X (where ABDC is 2-aminobenzene-1,4-dicarboxylic acid). In 2015, Hu et al.[76] used the modulated hydrothermal (MHT) synthesis method to synthesize other water-stable MOFs with the same structure as UiO-66, such as UiO-66-$(F)_4$, UiO-66-$(OCH_2CH_3)_2$ and UiO-66-$(COOH)_4$. The excellent chemical stability, easy functionalization, and wide range of structures of the UiO series provide them with

promising prospects in catalysis, separation, and adsorption.[77-82]

b) ZIF series

The ZIF series is an important subfamily of MOFs. It is composed of N atoms in the imidazolate ring and self-assembly of tetrahedrally coordinated divalent cations (structural formula: M-Im-M, M represents a metal cation, for example, Zn^{2+} or Co^{2+}, Im represents imidazolate ligands).[83] The structure of ZIF is very similar to that of traditional aluminosilicate zeolites, where typically Zn ions act as silicon, imidazolate anions form bridges, mimicking the role of oxygen in the zeolite, and metal-imidazole-metal (i.e. M-Im-M) bond angle is approximately 145°, similar to the Si-O-Si angle in zeolites.[84-85] As a result, ZIF has the properties of both MOFs and zeolites and is seen as an attractive porous material suitable for a variety of applications.[86-87] Because they combine the pore controllability, chemical stability, structural variability, thermal stability, and pore stability of zeolite sieves. For example, Küsgens et al.[88] initially reported the water vapor adsorption isotherm at 298 K for ZIF-8, a porous framework with sodalite (SOD) zeolite topology. This isotherm proves the strong hydrophobic properties and remarkable hydrothermal stability of the material. Bux et al.[89] prepared a zeolite imidazole framework (ZIF-8) membrane with molecular sieve properties with high selectivity for hydrogen.

In 2008, Yaghi's research group studied the impact of different influencing factors (such as the molar ratio of metal and ligand, solution concentration, temperature, reaction time, etc.) on the topology of the imidazole framework through high-throughput screening methods, and ZIF with ana, zni, dia, lcs, crb, frl, cag, sod, dft, gis, gme, lta, mer, rho zeolite topologies were synthesized (**Figure 1-4**).[90]
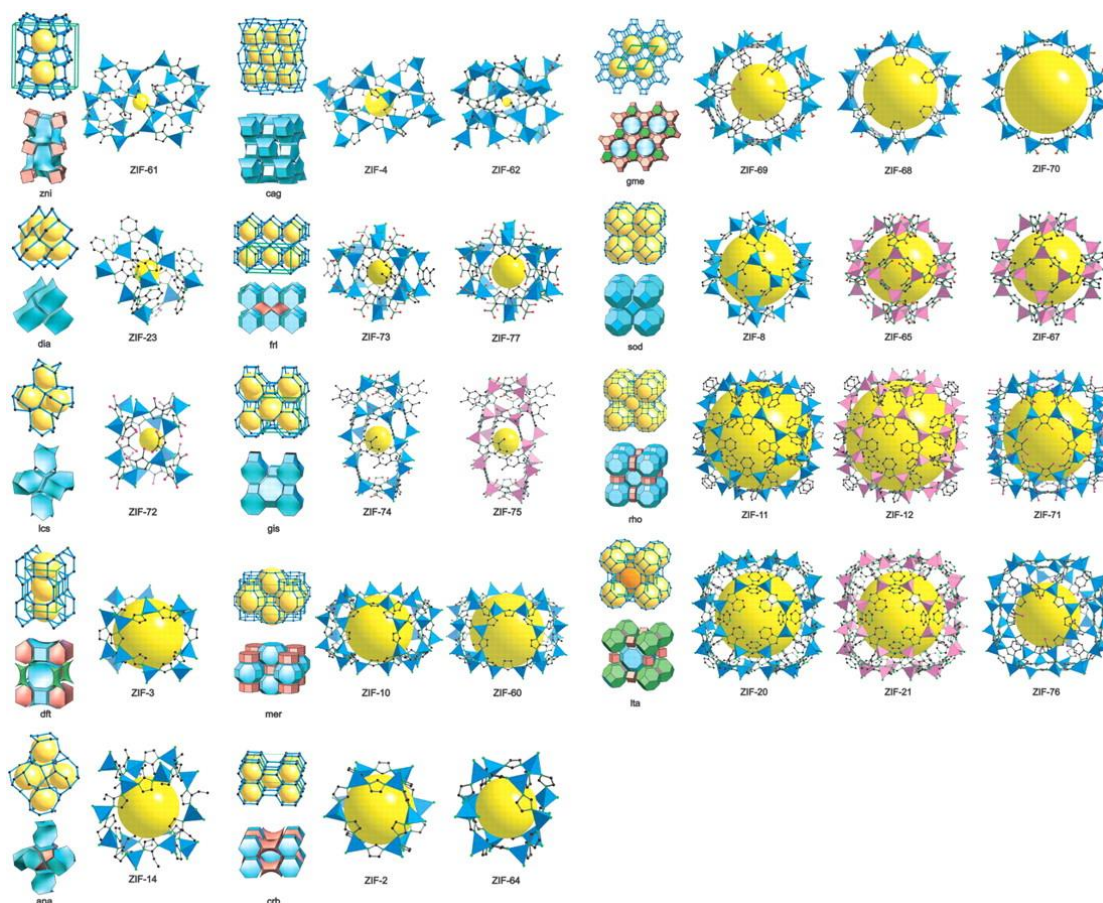
Figure 1-4. ZIF with different zeolite topologies. The largest cages in each ZIF are represented by ZnN_4 tetrahedra in blue and CoN_4 in pink. The yellow balls placed in the structure are to clearly show and indicate the spaces in the cage. H atoms have been omitted [IM and IM-type links are shown in ball-and-stick representation (C, black; N, green; O, red; Cl, pink)]. Reprinted with permission from AAAS ref. [90]. Copyright (2008) Science.

In addition to their similarities to zeolites, ZIFs also possess unique properties that set them apart from traditional zeolites. Such as larger specific surface area, flexible pore size, and simple and diverse designs.[91-93] ZIF consists of inorganic-organic framework types and may contain metals such as zinc and cobalt as well as non-metals such as nitrogen, carbon, and hydrogen. They also demonstrate strong thermal and chemical resistance in aqueous solutions and exhibit excellent compatibility with organic polymers.[94] A variety of ZIF-based compounds have been prepared, such as ZIF-8, ZIF-67, ZIF-95, $Zn(MIm)_2$, $Co(MIm)_2$, etc.[95-96] These different ZIF materials have

different physical and chemical properties and have different applications in different fields.[97-100]

1.2.3 Synthesis methods of MOFs

MOFs are usually formed by the self-assembly of metal clusters and organic ligands under specific conditions. From this perspective, the process can be viewed as an assembly of predefined elements rather than a traditional complete design process. Therefore, different synthesis methods are crucial for MOFs because of the complex pathways by which they are produced and the need to control their properties. Even starting from the same reaction mixture, using different synthesis methods will result in different MOF structures. This variation results from several factors influencing the synthesis process, including reaction conditions, reaction time, metal cluster to organic ligand ratio, and external stimuli.[101-102] So far, there are many synthesis methods for MOF materials, such as solvent/hydrothermal synthesis, microwave-assisted synthesis, mechanochemical synthesis, electrochemical synthesis, sonochemical methods, etc.[103-105] Appropriate methods can be selected for synthesis according to different raw materials and functional requirements. This thesis summarizes some important synthesis methods.

a) Solvent/hydrothermal synthesis

Among the various methods for synthesizing MOFs, the solvent/hydrothermal method is the most common and conventional approach used for synthesis. The solvothermal method is to dissolve or mix metal salts and organic ligands in aprotic or protic organic solvents, and then heat the mixture in a high-temperature Teflon-reactor to get high-quality single crystals (**Figure 1-5**).[106-109] Aprotic solvents commonly used to prepare MOFs include DMF, diethyl formamide (DEF), 1-methyl-2-pyrrolidone (NMP), dimethyl sulfoxide (DMSO), toluene, acetonitrile, etc. and commonly used protic solvents are ethanol, methanol, mixed solvents.[110-112] Hydrothermal methods are similar to solvothermal methods in that water is used as the solvent instead of organic solvents for the reaction. The nature of the solvent and the synthesis conditions such as

pH, surfactant, solubility of precursors, reaction time, etc. affect the growth of MOF crystals.[113-114]

This method has universal applicability in the synthesis of MOFs.[115-117] It is easy to use, simple to operate, and can obtain MOF materials with good crystallinity and large specific surface area.[118-119] However, solvent/hydrothermal methods also have some limitations, such as slow crystallization, low yield, and the high cost of the solvents and some organic ligands.[120] In addition, organic solvents are usually not friendly to the environment. For example, long-term use of DMF can cause harm to the human body.[121-122] Therefore, looking for green and environmentally friendly solvents to replace toxic solvents to synthesize MOFs is the future development trend.
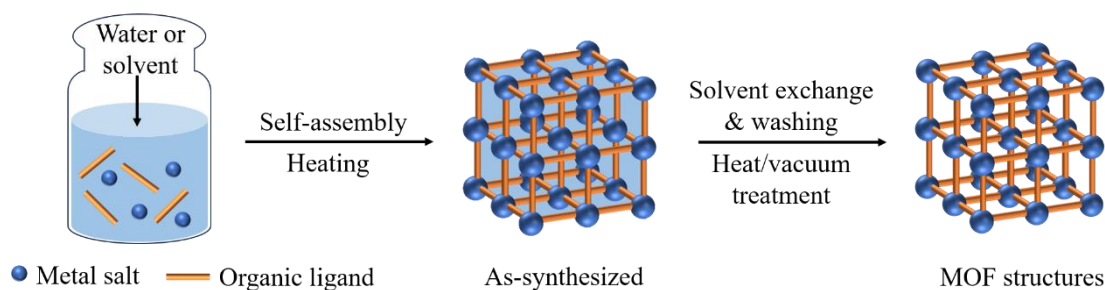
Figure 1-5. Solvent/hydrothermal synthesis of MOF structures.

b) Microwave-assisted synthesis

Microwave-assisted synthesis has been widely used in the rapid synthesis of nanomaterials and has also been used in the synthesis of MOFs.[123-124] Different from the traditional solvothermal method, the energy used for the reaction in the microwave-assisted method is obtained in the form of microwave radiation (**Figure 1-6**).[125] Using a microwave instead of a heat source to heat the mixture solution, the molecular rotation caused by the coupling of the electric field and molecular permanent dipole moment can heat the liquid medium quickly and uniformly, and the heating efficiency is higher.[126] Therefore, microwave synthesis can promote rapid nucleation and crystal growth of MOF network clusters, significantly reducing the reaction time, which is only a few minutes (min) to an hour (h).[127-128] The use of microwave-assisted synthesis of MOF materials can produce MOF materials with rich porous structures, smaller particle

sizes, and easily controllable morphologies.[129-131] However, the synthesized MOF crystals are of low quality are not suitable for fine structure analysis, and may require the design of specialized microwave devices. It is worth noting that since microwave synthesis uses the same reagents as solvothermal synthesis, it may have disadvantages such as low yields, toxic reagents, and high reaction temperatures.[132]
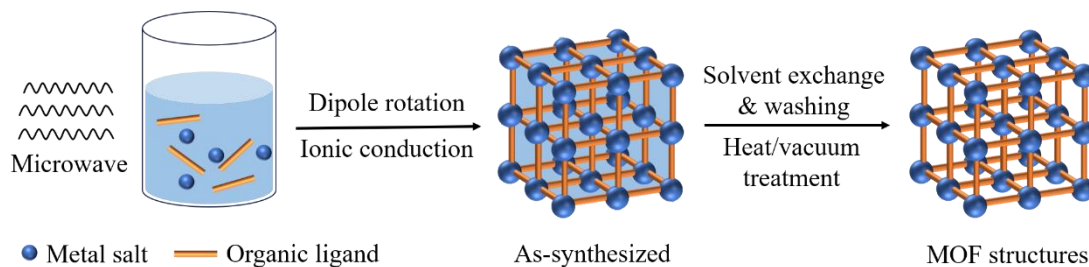
Figure 1-6. Microwave-assisted synthesis of MOF structures.

c) Mechanochemical synthesis

The mechanochemical method is a method that breaks intramolecular bonds by applying external mechanical force (i.e. grinding), followed by chemical transformation to generate the desired MOFs.[133] In this method, solid reactants such as ligand powder and metal salt are mainly added to a high-energy ball mill or mortar. During the rolling and rotating process of the mill ball, the solid reactant violently collides with the mill ball, causing the powder to break repeatedly in a cold sweat at high temperatures (**Figure 1-7**).[134-135] Therefore, this method does not require the use of solvents, does not produce any liquid waste after the reaction, and eliminates the tedious treatment process of later activation.[136] It is the most environmentally friendly preparation method so far. It is especially suitable for mass production and lays the foundation for the industrial preparation of MOF materials. In mechanochemical synthesis, since the solid-solid reaction is carried out under grinding conditions, the quality of the synthesized materials is not high and often contains more impurities.[137]
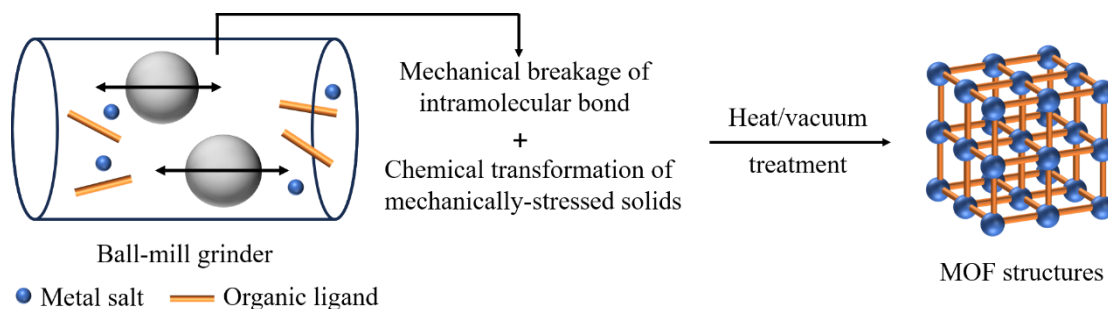
Figure 1-7. Mechanochemical synthesis of MOF structures.

d) Other methods

In addition to the above methods, MOFs synthesis methods also include electrochemical methods. Electrochemical synthesis uses the principle of electrolysis to convert a metal anode into metal ions and assembles MOFs with an electrolyte solution containing organic ligands.[138-139] This method is fast, requires low reaction temperature, and the final product has no residual anions (such as Cl^-, NO_3^-).[140] However, this method also has disadvantages such as dangerous reagents and high equipment and maintenance costs.

Furthermore, it also includes less commonly used sonochemical methods, diffusion methods, ionothermal methods, etc.[141-144] Different synthesis methods have their advantages and disadvantages. Therefore, when preparing different types of MOF materials, specific problems should be analyzed in detail and the appropriate synthesis method should be reasonably selected.

1.3 Construction strategies for macroscopic MOF materials

Over the past two decades, significant efforts have been dedicated to designing and synthesizing new MOF structures and exploring their various applications, some of which are now commercially available.[145-146] However, MOFs in nanoparticle form face challenges such as difficulty in recycling, poor processability, and clogging of pipelines during use, limiting their practical applications.[147] To address these issues, constructing MOF materials as macroscopic MOF materials is an effective solution.[148-151] Compared to individual MOF nanoparticles, macroscopic MOF materials can build

a bridge between the nanoscale and meso/macroscale worlds, producing unique and interesting properties.

Based on their morphology in different dimensions, the macroscopic MOF materials can be classified into zero-dimensional (0D) particles, one-dimensional (1D) nanofibers, two-dimensional (2D) membranes, and three-dimensional (3D) macrostructures (**Figure 1-8**).[23] Next, I will introduce the synthesis strategies for these different types of macroscopic MOF materials.

Structuring of macroscopic MOF materials

0 D particle   **1 D fiber**   **2 D membrane**   **3D macrostructure**
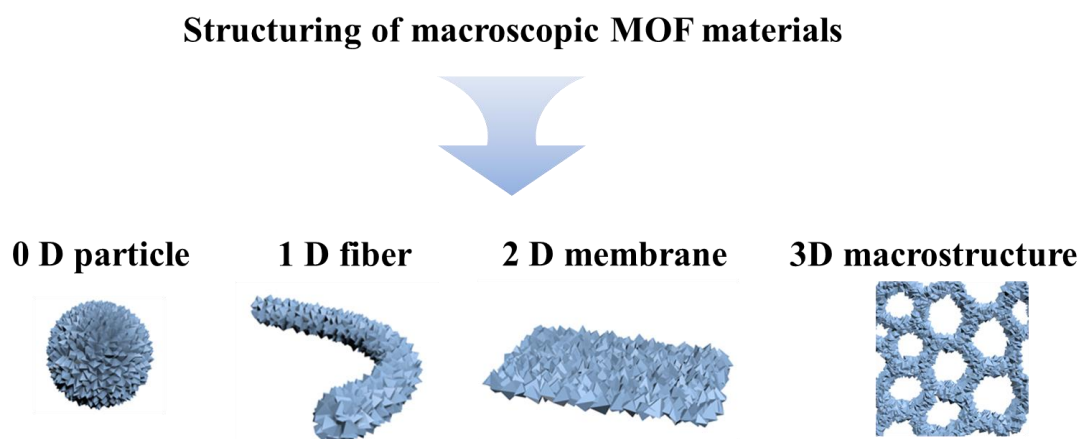
Figure 1-8. The morphology of macrostructures MOFs in different dimensions.

1.3.1 0D MOF particles

The size of 0D nanostructures varies from a few nanometers to a hundred nanometers, usually in the form of spheres, polyhedrons, ellipsoids, and quantum dots.[152] The most direct and simple strategy to construct 0D MOF materials is the macrostructure template method, which involves using a pre-existing structure to guide the formation of the desired MOF morphology. This method introduces preformed macrostructure templates into the reaction mixture solution during MOFs synthesis. In the second step, the template material can be removed through an etching process to obtain a pure MOF superstructure (**Figure 1-9a**).[153-156] For example, Shen et al.[157] demonstrated the growth of ZIF-8 MOF micro crystals on a polystyrene nanosphere monolithic template. Afterward, the polystyrene microspheres were removed through solvent extraction, resulting in a single crystal with a directional and ordered large microporous structure.

Compared to conventional polycrystalline hollow and disordered macro-porous ZIF-8, these hierarchical frameworks exhibit improved mass diffusion properties and a robust single-crystalline nature, which confer excellent catalytic activity and recyclability for macromolecular reactions.
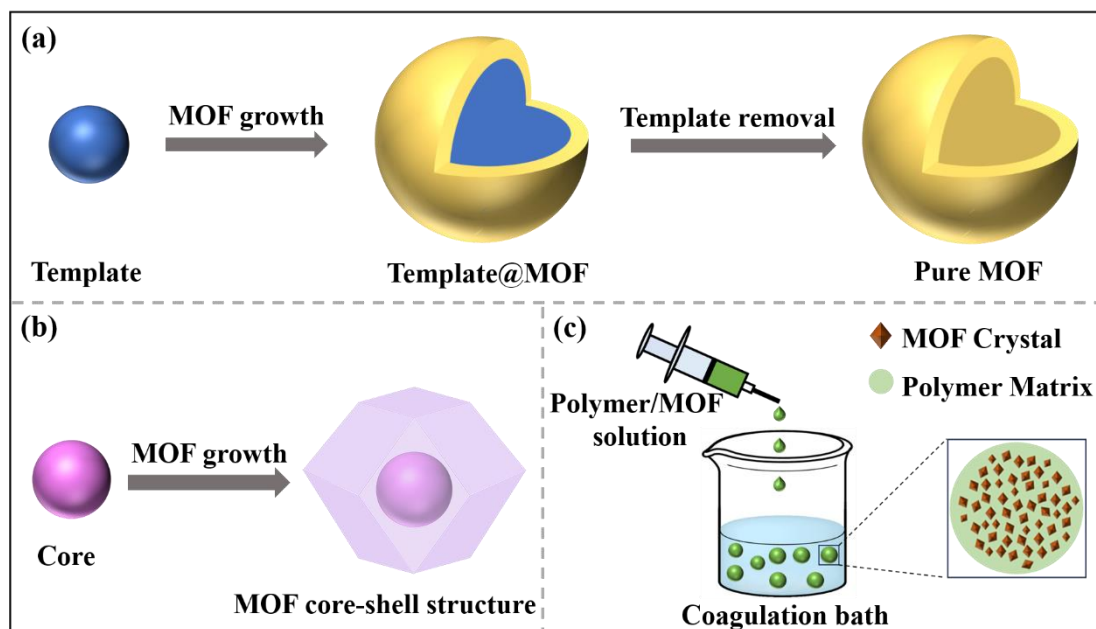
Figure 1-9. Construction of 0D MOF particles by (a) macrostructure template method; (b) core-shell structure; and (c) directly combined with macro-scale carriers.

Core-shell structures are also often used to construct 0D MOF particles (**Figure 1-9b**). The preparation of core-shell structures can give MOFs new physical and chemical properties, thereby broadening MOF's performance and practical applications.[158-160] There are many common core-shell structures, such as metal/non-metal nanoparticles@MOF, metal oxide nanoparticles@MOF, MOF@MOF, etc.[161-163] The combination of two MOFs was first reported by Tang et al.[164] They first synthesized ZIF-8 using a conventional method and then used the synthesized ZIF-8 as a hard template to uniformly grow ZIF-67 on the outer surface of ZIF-8. They used this core-shell structured (ZIF-8@ZIF-67) MOF as a carbon precursor and carbonized it in a nitrogen atmosphere at 800 °C to obtain a nanoporous carbon material with a unique specific capacitance of 270 F g^{-1}.

In addition, MOFs can also be directly combined with macro-scale carriers to obtain

0D MOF particles (**Figure 1-9c**).[152,165-166] For example, Zhao et al.[167] reported a general method to prepare MOF-chitosan composite beads through in-situ growth. Chitosan/metal hydroxide (or metal oxide) beads were used as substrates for MOF immobilization, in which metal hydroxide or metal oxide was the precursor template for MOF growth. Through the self-condensation of the corresponding metal hydroxides or metal oxides in the organic ligand solution MOFs were prepared and stably fixed in the chitosan substrate. The shape of the beads allows easy recycling of ZIF-8-chitosan composites.

1.3.2 1D MOF fibers

The synthesis strategies for preparing MOF-based fibers mainly include direct solvothermal growth, atomic layer deposition (ALD) metal oxide directional growth, and layer-by-layer (LbL) growth (**Figure 1-10**).
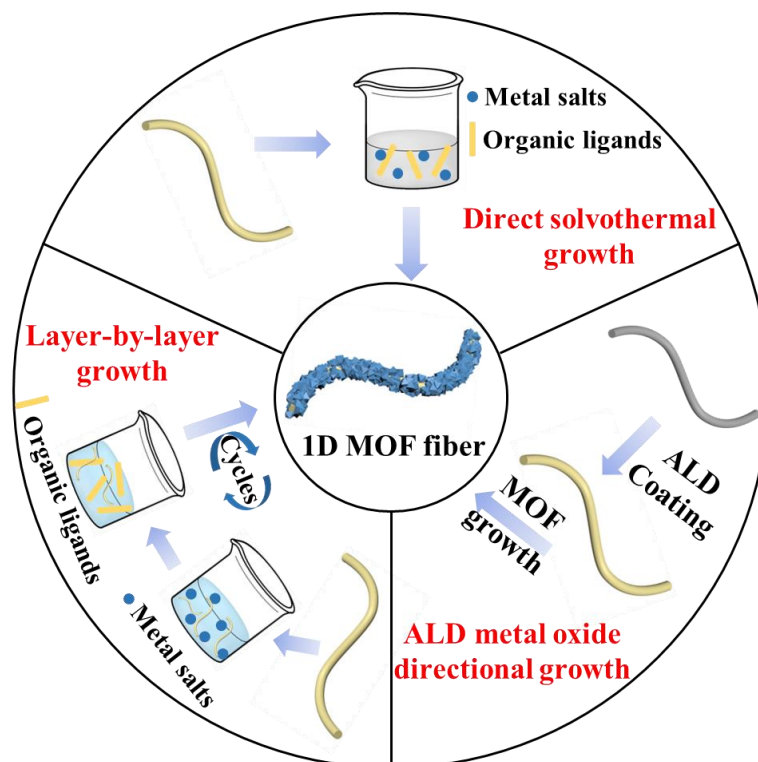
Figure 1-10. Synthesis diagram of 1D MOF fibers.

Direct solvothermal growth: MOF fibers can be grown directly on the fiber substrate through the solvothermal method. Lu et al.[168] successfully demonstrated the direct solvothermal growth of the MOF (UiO-66-NH₂) on the surface of electrospun polymer fibers. First, the ligand amino terephthalic acid (ATA) was electrospun with the polymer solution and acted as anchors or nucleation points for MOF growth on immersing the ATA-containing polymer fibers in an acetone solution of equimolar zirconium tetrachloride ($ZrCl_4$) and ATA.

ALD metal oxide directional growth: This method conformally deposits a metal oxide film (such as aluminum oxide (Al_2O_3), zinc oxide (ZnO), or titanium dioxide (TiO_2)) on the surface of the polymer fiber through ALD that is used further for the growth of MOF.[169-170] For example, Zhao and co-workers[171] used ALD to deposit Al_2O_3 nanoscale coating on the nonwoven fiber mat, enabling the growth of HKUST-1 [Cu_3(BTC)] on the Al_2O_3 coated fibers by a solvothermal method (HKUST stands for Hong Kong university of science and technology). The resulting MOF crystals maintain their functionality and adhere well to the fibers. Al_2O_3 ALD coating improves the macroscopic uniformity of the MOF and its coverage on the fiber surface. Compared with MOFs grown on untreated polypropylene (PP) fibers, MOF-PP/ALD fibers exhibit higher Brunauer-Emmett-Teller (BET) surface area, high MOF loading, and higher adsorption capacity. Lee et al.[172] deposited a TiO_2 film (thickness approximately 20 nm) on PP fibers through ALD and selected ALD TiO_2 as a heterogeneous nucleation site to generate Zr-based MOF fibers (PP@TiO₂@MOF). The overall MOF@fiber adhesion and uniformity of the TiO_2 ALD layer enable these fibers to have good detoxification activity against chemical warfare agents (CWAs), and their catalytic performance is 580 times higher than that of unmodified PP textiles.

LbL growth: Different from direct solvothermal synthesis, layer-by-layer assembly involves sequentially coating the fiber with a metal salt solution and a ligand solution, respectively. During the precursor coating process, the substrate was rinsed with pure solvent to remove any excess precursor. Using the discontinuous MOF crystallization process, the thickness can be precisely controlled. In addition, this method is carried out under mild conditions and is suitable for large-scale production. Morsali and

colleagues reported a sonication-assisted LbL method for growing HKUST-1 on the surface of silk fibers. First, the silk fibers were sequentially immersed in a metal salt solution and an organic ligand solution in sequence, and ultrasound was used to accelerate the growth reaction of LbL. Then, the crystallinity of the MOF was improved by increasing the number of HKUST-1 cycles of layer-by-layer coating on the silk fiber.[173]

Li and colleagues grafted -COOH onto cotton fabrics (CF) by carboxymethylation, providing coordination for Cu ions and promoting MOF growth. After 10 layer-by-layer growth cycles, CuBTC-MOF grew in situ on the CF, evenly and densely covering the surface of the CF-COOH fiber, and presenting a regular octahedron structure. In contrast, the pristine CF fiber surface showed only sparse and uneven MOF growth due to the lack of active carboxymethyl groups. Thus, MOF nucleation may occur and continue to grow on random defects in untreated fibers, resulting in a sparse and irregular coating of CuBTC crystals.[174]

1.3.3 2D MOF membranes

Electrospinning technology is a versatile method for preparing thin fibers with diameters ranging from 2D nanometers to several microns. In this method, a polymer solution is continuously pulled out from a spinning nozzle in the form of nanofibers under the application of a high voltage.[175] These fibers are then continuously collected on a collector in the form of a membrane in which fibers lay randomly onto each other.[176-177] The method has also been used for making 2D MOF-polymer membranes. Currently, there are two main approaches to preparing MOF-polymer fiber membranes based on electrospinning: direct electrospinning (**Figure 1-11a**) and surface in-situ growth (**Figure 1-11b**).

In the direct electrospinning method, a suspension of MOF particles in a polymer solution in an organic solvent is used for electrospinning. The most common polymers used for this purpose are polyurethane (PU), polystyrene (PS), polyacrylonitrile (PAN), poly(vinyl pyrrolidone) (PVP), and poly(vinylidene fluoride) (PVDF).[178-179]

Wang et al.[180] synthesized a series of MOFs (UiO-66-NH₂, ZIF-8, Mg-MOF-74, and MOF-199) and incorporated them into PAN, PS, and PVP spinning solutions. Nanofiber membranes were obtained by direct electrospinning and used for air filtration. By controlling the particle size and morphology of different MOF crystals, a high loading (up to 60 wt%) was achieved in the polymer matrix without particle aggregation. This method is suitable for preparing polymer membranes with all types of MOFs, and the MOF loading in the fiber membranes can be accurately controlled by changing the amount of MOFs added. Since MOF particles are embedded in the polymer nanofiber membrane, the internal pores of the original MOF crystals are often covered by the polymer matrix, which greatly limits the use of MOFs in most applications.[181] In addition, the method is restricted by a limited weight percentage loading of MOFs, issues during electrospinning due to the increased viscosity of the spinning suspension, and clogging of the spinning nozzles.[182]
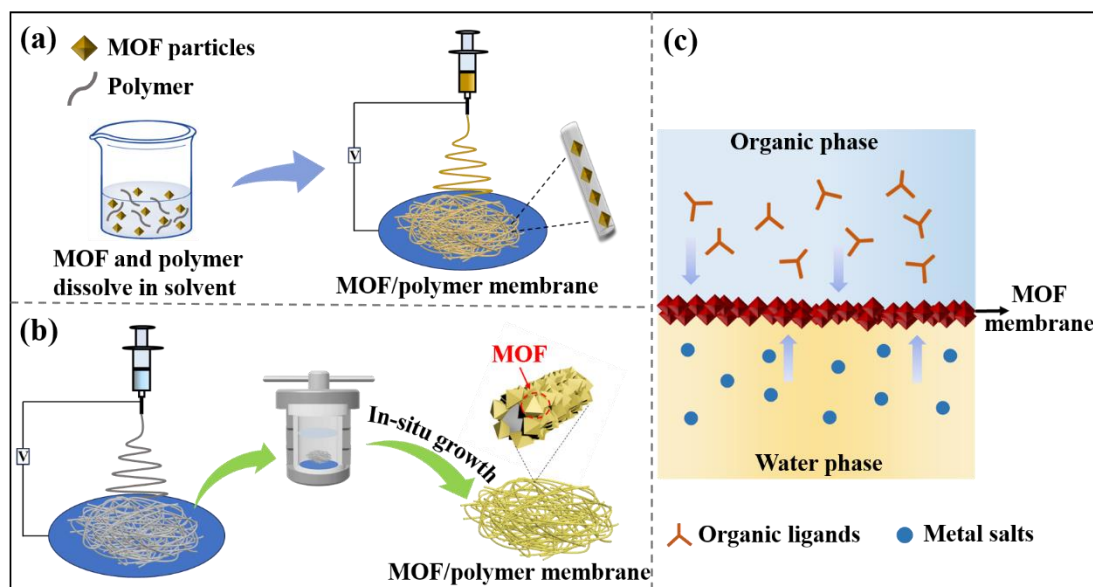
Figure 1-11. Schematic of preparation of 2D MOF membranes by 1) electrospinning: (a) direct electrospinning; (b) surface in-situ growth, and 2) liquid-liquid interface reaction (c).

The surface in-situ growth method can effectively overcome these shortcomings. In this method, MOFs are grown in situ on the surface of the polymer fiber membrane. The internal and surface pores of the original MOF particles are not covered by the polymer

matrix, which can well retain the surface area, pores, and physical and chemical properties of the MOFs. Zhao et al.[183] successfully prepared electrospun PAN fiber membranes (PAN@MIL-100(Fe) fiber membrane) from H_3BTC/PAN (H_3BTC is 1, 3, 5-tricarboxylic acid) precursor fiber membranes through electrospinning and hydrothermal processes. In this work, they added the organic ligand H_3BTC to the PAN spinning solution and electrospun the H_3BTC/PAN precursor fiber membrane. Then the fiber membrane was placed in the precursor solution of MIL-100(Fe) (an aqueous solution containing iron (III) chloride ($FeCl_3$) and H_3BTC for solvothermal reaction to obtain the PAN@MIL-100(Fe) fiber membrane. It is worth noting that during the spinning process, the addition of H_3BTC provides nucleation sites for the subsequent in-situ growth of MIL-100(Fe) on the electrospun PAN fiber, allowing the uniform growth of MIL-100(Fe) on the surface of PAN fiber, the loading of MIL-100(Fe) is as high as 58%. The fiber membrane has excellent removal efficiency for pollutants in wastewater treatment and also exhibits good recyclability and reusability. Wang and his colleagues[184] reported a method for in-situ growth preparation of MOF filters. First, the metal salt cobalt (II) acetylacetonate ($Co(acac)_2$) and PAN were dissolved in DMF to form an electrospinning solution. After electrospinning, a $Co(acac)_2$/PAN fiber membrane was obtained which was then used for the in situ growth of ZIF-67. In this case, ZIF-67 could retain its morphology, structure, and accessibility on the membrane. Unfortunately, in the in-situ growth method, MOF nucleation may occur in the solvent rather than on the surface of the preformed nanofiber membrane, thus causing waste of precursors.[185]

2D MOF membranes can also be achieved by the interfacial growth method, which typically occurs at the interface of two solvents (**Figure 1-11c**). One solvent contains the metal salt and the other solvent contains the ligand. According to a diffusion-mediated process, the metal and ligand will react at the interface of the solvent mixture to form a MOF ultrathin film.[186]

1.3.4 3D MOF macrostructures

3D MOF macroscopic materials are usually constructed by the growth of MOFs on a 3D matrix carrier (**Figure 1-12**). The 3D matrices commonly used to prepare 3D macroscopic MOF materials include sponge, wood, foam, etc.[187-188]
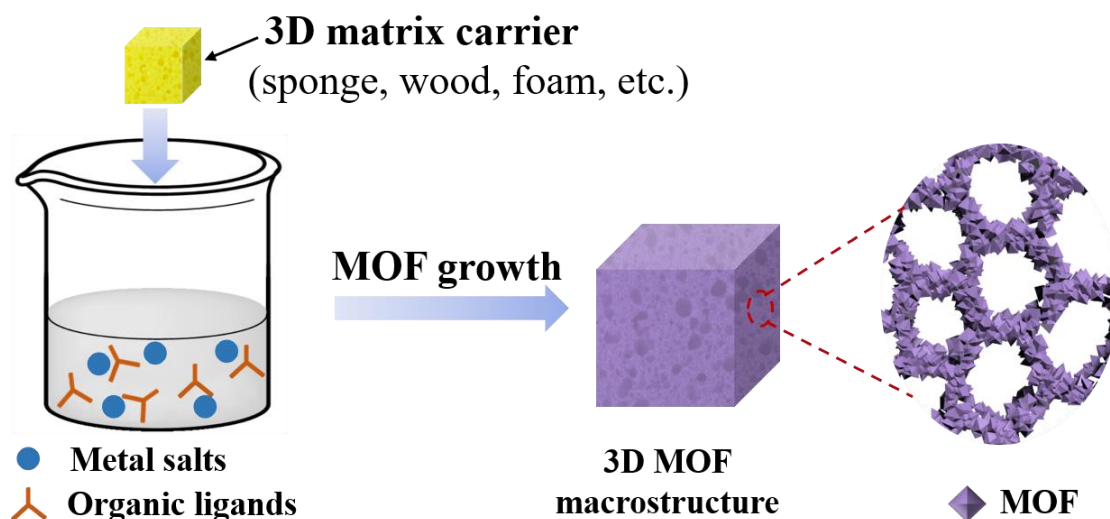
Figure 1-12. Schematic of preparation of 3D MOF macrostructures by growing MOFs on a 3D matrix carrier.

The most commonly used method for constructing 3D MOF macrostructure is the in situ growth method. The in-situ growth method refers to the direct preparation of MOF layers on the substrate using solvothermal or hydrothermal methods. Guo et al.[189] developed 3D Zr-MOF using natural wood as the carrier (UiO-66/wood). UiO-66 was grown in situ in a 3D low-tortuosity wood lumen via a facile solvothermal strategy. The resulting UiO-66/wood contains a highly mesoporous UiO-66 MOF structure as well as many elongated and open lumens along the wood growth direction. This unique structural feature improves the mass transfer of organic pollutants and increases the contact probability between organic pollutants and UiO-66 MOFs when water flows through the membrane, thereby improving the removal efficiency. Ren et al.[190] loaded ZIF materials on cellulose aerogels through in-situ growth. Aerogels are a unique class of ultralight materials that are filled with approximately 95% air volume, have large

void spaces, open porous structures, and very low density (0.004 - 0.005 g cm^{-3}).[191] The author soaked the prefabricated cellulose aerogel in a DMF solution of Co(NO$_3$)$_2\cdot$6H$_2$O for 24 h. This solution was then mixed with a DMF solution in which benzimidazole was dissolved, and allowed to stand for 24 h, allowing the formation of aerogel-supported ZIF.

In addition, to improve the adhesion and nucleation ability of MOFs on the substrate, functional groups are usually generated on the substrate through modification, and these functional groups can be combined with metal ions or ligands. The modified substrate is then subjected to solvothermal or hydrothermal treatment to grow a MOF layer. Cheung et al.[192] used a carbon nanotube (CNT) sponge composed of stacked multi-walled nanotubes as a template to successfully prepare a flexible and compressible CNT@MOF sponge by growing MOF particles in situ inside the sponge. In this process, the CNT sponge is first treated with HNO$_3$ to generate functional groups on the CNT surface as coordination sites, followed by ZIF-8 nucleation by forming Zn-O chemical bonds. Then the acid-treated CNT sponge is soaked in the precursor of ZIF-8 to perform a solvothermal reaction to obtain a CNT@ZIF-8 sponge. Yang et al.[193] used maleic anhydride (MAH) to modify the cellulose sponge (CS) and introduced carboxyl groups onto the CS to provide sites for the nucleation of MOF. The MOFs are firmly and evenly dispersed on the maleic anhydride-modified cellulose sponge surface. Porous MOF@modified cellulose sponge (MCS) composites were obtained by in situ growth of Zr MOFs on modified cellulose sponges. MOFs@MCS composites exhibit excellent water and dimensional stability when removing heavy metal ions and organic dyes from water.

In my work, I used a 3D polymer network carrier, created by the self-assembly of short electrospun fibers, for the in situ growth of MOF, as described in detail in Chapter 1.5.

1.4 Applications of MOFs

MOFs are a new class of porous and crystalline materials developed in recent years, formed by the self-assembly of inorganic metal centers and organic ligands through

coordination bonds. Their unique properties, including high permanent porosity, large specific surface area, abundant active sites, multifunctional frameworks, and adjustable pore sizes, make them excellent candidates for various applications, such as catalysis, adsorption and separation, water purification, energy storage, and other fields.[194-195] In the following sections, I describe the existing literature on the use of MOFs for catalysis and water treatment applications. In my research, I utilized self-synthesized macroscopic MOFs for these purposes.

1.4.1 Catalysis

A catalyst refers to a substance that can promote the reaction or speed up the reaction rate during a chemical reaction, and its own physical and chemical properties remain unchanged.[196] Porous materials play an indispensable role in the field of catalysis. Compared with traditional porous catalytic materials (zeolites, silica salts, molecular sieves, activated carbon, etc.), MOFs are easy to synthesize and have channels (pores) or cages that allow the free flow of reactants and products and catalytic sites with different spatial distributions. MOFs can also be diversified in structure by carefully selecting appropriate metal nodes and organic connectors. In addition, the metal centers and ligands of the MOF structures are modified or substituted through post-modification methods to give them rich and diverse physical and chemical properties.[197-198] So far, MOF materials have been used in various reactions such as cyanidation reactions, hydrogenation reactions of aromatic compounds, oxidation reactions of hydrocarbons and alcohols, esterification reactions, coupling reactions, and photocatalytic degradation reactions.[199-201]

Huo and colleagues designed a porous anionic framework material to catalyze the carboxyl cyclization reaction of propargyl alcohol with carbon dioxide (CO_2). It can be used as an effective catalyst for the cyclization of propargyl alcohol with CO_2 under mild, solvent-free conditions, with a record turnover number (TON) of 14,400. It is worth mentioning that this MOF catalyst also shows rare catalytic activity when using biomacromolecule alkynone as a substrate. This is the first example of the use of a non-

noble metal to directly catalyze the carboxyl cyclization of propargyl alcohol with CO_2.[202] Chen et al. used a solvothermal synthesis method to construct a novel 3D photoactive Zn-MOF using carefully designed propeller-shaped tris(3-carboxy biphenyl)amine (H_3TCBA) ligands and Zn_3O clusters. This Zn-MOF was utilized as a heterogeneous photocatalyst. The uniquely twisted triphenylamine photosensitive units and metal cluster quantum dots within the MOF channels not only facilitate light-induced charge separation, enabling oxygen activation and proton reduction but also provide abundant π interaction sites around the MOF channels. The photo-induced electron transfer process between it and guest molecules promotes Zn-TCBA to show good photocatalytic activity and stability in photocatalytic hydrogen production. In addition, the appropriate excited state potential and semiconductor-like properties of Zn-TCBA give Zn-TCBA the ability to activate double oxygen and achieve efficient photooxidation conversion.[203]

Lee et al.[204] prepared a highly porous and stable acid-base bifunctional metal-organic framework MIL-101 (MIL-NH_2-SO_3H) through direct solvothermal synthesis using two mixed (-NO_2, -SO_3H) terephthalate ligands. This framework exhibits excellent performance in one-pot tandem deacetalization-nitroaldol reactions. Zhou et al.[205] developed a new bifunctional MOF nano-catalyst UiO-66-OTf (OTf comes from organic ligand trimethylsilyl triflate) through post-synthetic modification. This catalyst has enhanced Lewis acid sites and photoredox sites, and can effectively catalyze the reduction of 2-aryloxybenzaldehyde into flavonoids using ethanol as the reducing agent. This is a new method that can efficiently synthesize flavonoids without excessively strong oxidants.

1.4.2 Wastewater treatment

MOF materials have become a promising wastewater treatment material due to their porosity, structural diversity, excellent chemical stability in water and acid-base solutions, and structural stability in a variety of organic solvents. MOFs and their macroscopic materials have excellent and efficient removal efficiency for a series of

organic and inorganic pollutants such as heavy metals such as mercury, lead, chromium or arsenic, organic dyes, antibacterial agents, antibiotics, and persistent chemicals in wastewater.[206-207]

For example, Nimbalkar et al.[208] synthesized low-cost UiO-66 MOF using 1,2,4, 5-benzoic acid as an organic ligand by one-pot hydrothermal method and used for the removal of methylene blue (MB) and heavy metals (lead and cadmium) from aqueous solutions. The results show that the adsorption capacities of the MOF materials for cadmium, lead, and MB are 37 mg g^{-1}, 100 mg g^{-1}, and 169 mg g^{-1}, respectively. MIL-101-AO (AO is amidoxime) demonstrated excellent adsorption performance and recyclability for Uranium (VI), with an initial adsorption capacity exceeding 500 mg g^{-1} and retaining over 450 mg g^{-1} after five cycles. In artificial seawater, in the presence of competing metal ions, the selective adsorption efficiency for U(VI) es reaches 96%.[209] Li and his colleagues synthesized the MOF PCN-222 (PCN is a porous coordination network) using a solvothermal method. PCN-222, a porous coordination network, effectively removes both anionic and cationic dyes from aqueous solutions. In a single dye system, PCN-222 demonstrated a maximum removal efficiency of 906 mg g^{-1} for the anionic dye MB and 589 mg g^{-1} for the cationic dye methyl orange (MO). Notably, when MB and MO coexist in the solution, their adsorption capacities are mutually enhanced by 36.8% (1239 mg g^{-1}) and 73.5% (1022 mg g^{-1}), respectively. Additionally, during the removal process, neither the crystal structure nor the removal capacity of PCN-222 showed significant changes after eight cycles.[210]

1.5 Electrospinning

In my research, I utilized the electrospinning method as a tool for fabricating macroscopic MOF structures. In this section, I provide a brief overview of the electrospinning technique.

1.5.1 Method of electrospinning

Electrospinning is a relatively robust and simple process that uses electrostatic forces

to produce continuous fibers from polymer solutions or melts.[211] The basic electrospinning equipment mainly includes a high-voltage power supply, a syringe pump, a spinneret (usually a blunt-ended injection needle), and a collector (a metal foil, plate, disc, or drum).[212-213] Before electrospinning, most polymers will be dissolved in certain solvents (such as DMF, DMSO, dichloromethane (DCM), chloroform, etc.). After complete dissolution, a polymer solution is formed, and then the polymer fluid is introduced into the syringe for electrospinning. During the electrospinning process, the polymer solution is extruded from the spinneret, producing pendant droplets under the action of surface tension. After energization, the electrostatic repulsion between surface charges of the same sign causes the droplets to form a Taylor cone, from which a charged jet is ejected.[214-215] Subsequently, the charged solution jet is ejected from the tip of the Taylor cone. In the space between the spinneret tip and the collector, the jet undergoes an unstable and violent whipping motion and is stretched to a smaller diameter. It is finally deposited in the form of solid fibers on a grounded collector.[216] **Figure 1-13** provides a brief explanation of the electrospinning process. By adjusting electrospinning solution parameters (viscosity/concentration, conductivity, molecular weight of polymer, solvent selection), process parameters (applied voltage, flow rate, distance between spinneret and collector), and environmental parameters (temperature, humidity), almost all soluble or fusible polymers, including various synthetic polymers (such as polylactic acid (PLA), PU, polyethylene (PE), copolymer poly(lactide-co-glycolic acid), etc.), natural polymers (such as collagen, chitosan, cellulose acetate, silk protein, etc.) or a mixture of the two, and even proteins, nucleic acids, polysaccharides, etc. can be used for electrospinning.[217-221]
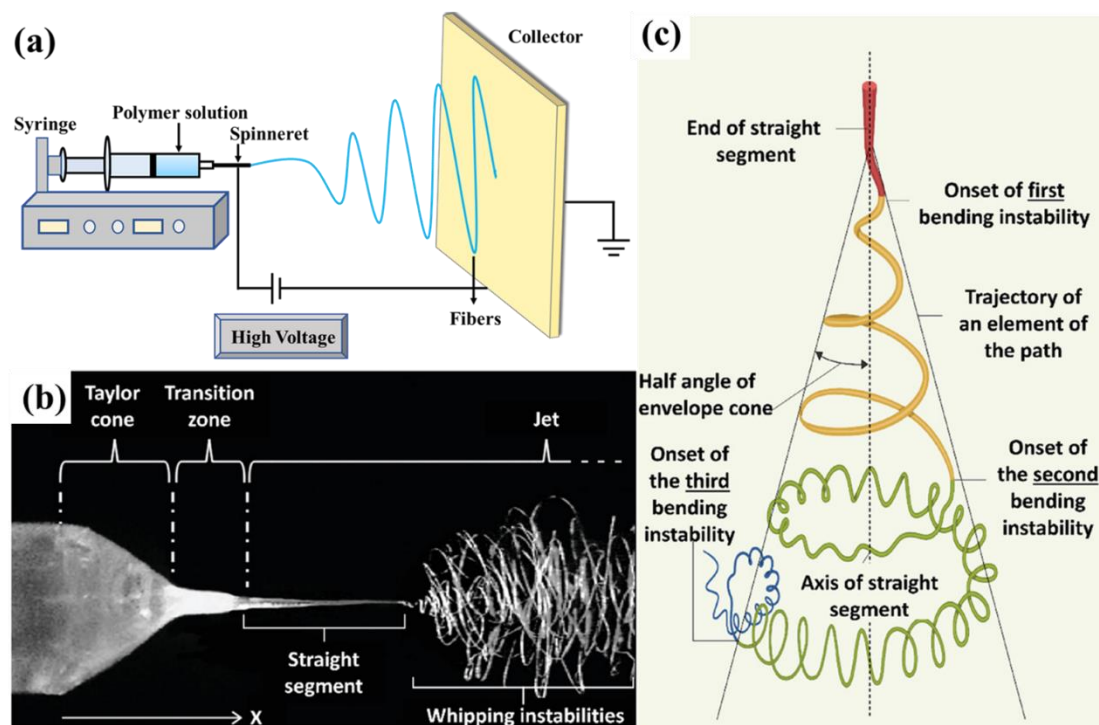
Figure 1-13. (a) Schematic diagram of the electrospinning process. (b) High-speed photograph outlining the Taylor cone formation, depicting the linear segment of the polymer jet, followed by the whipping jet region. (c) The prototypical instantaneous position of the jet path succeeding through the three sequential bending instabilities. Reprinted with permission from ref. [220]. Copyright (2023) Wiley-VCH.

1.5.2 Short electrospun fiber sponges

The fiber diameters produced by electrospinning range from nm to micrometers (µm), offering an extremely high specific surface area-to-volume ratio, adjustable porosity, controllable nanofiber composition, and other advantageous characteristics.[222] It has been widely studied by researchers and used in various fields, including protective clothing, filtration, biomedicine, nanocatalysis, defense and security, and environmental engineering.[223-224] However, electrospun fibers are usually assembled into 2D fiber membranes (thickness less than 100 µm). It is difficult for fibers to penetrate in the direction perpendicular to the deposition plane, and problems such as poor resilience and easy peeling between fiber layers greatly affect its practical

applications in many fields.[225] Compared to 2D electrospun fiber membrane materials, the interwoven and interconnected structure of a 3D fiber sponge provides a well-connected network with higher specific surface area and porosity.[226] Constructing 3D fiber sponges is a significant challenge in expanding the practical applications of electrospun fibers. To date, various methods, including hydrogel encapsulation, 3D printing, gas foaming, and freeze-drying, have been developed for this purpose.[227-228] Among these methods, the 3D fiber network structure, constructed by freeze-drying homogeneous short electrospun fibers, is widely used due to its simplicity, convenience, and controllable size and shape. Freeze-drying is a dehydration process where the frozen solvent sublimates directly from the solid phase to the gas phase under reduced ambient pressure.[229-230] In this method, a homogeneous dispersion of short electrospun fibers is first prepared by mechanically cutting long, continuous fiber membranes. The resulting short fiber dispersion is then freeze-dried to form a 3D fiber sponge. The size, shape, and microstructure of the sponge can be tailored by adjusting the mold type and freeze-drying conditions.[231] The 3D hierarchical porous network structure endows the fiber sponge with high porosity, making it highly effective in applications such as seawater desalination, oil-water separation, and supercapacitors.[232-235] The unique structure of electrospun 3D fiber sponges can effectively address challenges in MOF processing, recycling difficulties, and agglomeration tendencies. In my research work, I demonstrated the fabrication of hierarchical porous MOF sponges using 3D electrospun short fiber sponges as carriers and successfully applied them to activate peroxymonosulfate for the degradation of organic pollutants in wastewater.

1.6 References

[1] Davis M. Ordered porous materials for emerging applications[J]. Nature, 2002, 417(6891): 813-821.

[2] Chen Z, Kirlikovali K O, Idrees K B, et al. Porous materials for hydrogen storage[J]. Chem, 2022, 8(3): 693-716.

[3] Wang H, Wang X, Li M, et al. Porous materials applied in nonaqueous Li-O$_2$ batteries: status and perspectives[J]. Advanced Materials, 2020, 32(44): 2002559.

[4] Siegelman R L, Kim E J, Long J R. Porous materials for carbon dioxide separations[J]. Nature Materials, 2021, 20(8): 1060-1072.

[5] Zhu L, Shen D, Luo K, et al. A critical review on VOCs adsorption by different porous materials: Species, mechanisms and modification methods[J]. Journal of Hazardous Materials, 2020, 389: 122102.

[6] Zhou H C, Long J R, Yaghi O M. Introduction to metal-organic frameworks[J]. Chemical Reviews, 2012, 112: 673-674.

[7] Kitagawa S. Metal-organic frameworks (MOFs) [J]. Chemical Society Reviews, 2014, 43(16): 5415-5418.

[8] Furukawa H, Cordova K E, O'Keeffe M, et al. The chemistry and applications of metal-organic frameworks[J]. Science, 2013, 341(6149): 1230444.

[9] Dang S, Zhu Q L, Xu Q. Nanomaterials derived from metal-organic frameworks[J]. Nature Reviews Materials. 2017, 3(1): 1-14

[10] Chakraborty G, Park I H, Medishetty R, et al. Two-dimensional metal-organic framework materials: synthesis, structures, properties and applications[J]. Chemical Reviews, 2021, 121(7): 3751-3891.

[11] Yaghi O M, Li H. Hydrothermal synthesis of a metal-organic framework containing large rectangular channels[J]. Journal of the American Chemical Society, 1995, 117(41): 10401-10402.

[12] Chen Z, Kirlikovali K O, Li P, et al. Reticular chemistry for highly porous metal-organic frameworks: The chemistry and applications[J]. Accounts of chemical research, 2022, 55(4): 579-591.

[13] Furukawa H, Ko N, Go Y B, et al. Ultrahigh porosity in metal-organic frameworks[J]. Science, 2010, 329(5990): 424-428.

[14] Jiang H L, Xu Q. Porous metal-organic frameworks as platforms for functional applications[J]. Chemical Communications, 2011, 47(12): 3351-70.

[15] Lee J, Farha O K, Roberts J, et al. Metal-organic framework materials as catalysts. Chemical Society Reviews, 2009, 38(5): 1450-9.

[16] Firmino A D G, Mendes R F, Tomé J P C, et al. Synthesis of MOFs at the industrial scale[J]. Metal-Organic Frameworks: Applications in Separations and Catalysis, 2018, 57-80.

[17] Pobłocki K, Drzeżdżon J, Gawdzik B, et al. Latest trends in the large-scale production of MOFs in accordance with the principles of green chemistry[J]. Green Chemistry, 2022, 24(24): 9402-9427.

[18] Ullah S, Rehman A, Najam T, et al. Advances in metal-organic framework@ activated carbon (MOF@AC) composite materials: Synthesis, characteristics and applications[J]. Journal of Industrial and Engineering Chemistry, 2024, 137: 87-105.

[19] Chen Y, Li S, Pei X, et al. A solvent-free hot-pressing method for preparing metal-organic framework coatings[J]. Angewandte Chemie International Edition, 2016, 55(10): 3419-3423.

[20] Neves P, Gomes A C, Amarante T R, et al. Incorporation of a dioxomolybdenum (VI) complex in a ZrIV-based Metal-Organic Framework and its application in catalytic olefin epoxidation[J]. Microporous and Mesoporous Materials, 2015, 202: 106-114.

[21] Sun L, Campbell M G, Dincă M. Electrically conductive porous metal-organic frameworks[J]. Angewandte Chemie International Edition, 2016, 55(11): 3566-3579.

[22] Sculley J, Yuan D, Zhou H C. The current status of hydrogen storage in metal-organic frameworks updated[J]. Energy & Environmental Science, 2011, 4(8): 2721-2735.

[23] Lin H, Jie B, Ye J, et al. Recent advance of macroscopic metal-organic frameworks for water treatment: A review[J]. Surfaces and Interfaces, 2023, 36: 102564.

[24] Xiao W, Cheng M, Liu Y, et al. Functional metal/carbon composites derived from metal-organic frameworks: insight into structures, properties, performances, and

mechanisms[J]. ACS Catalysis, 2023, 13(3): 1759-1790.

[25] Peng R, Zhang S, Yao Y, et al. MOFs meet electrospinning: New opportunities for water treatment[J]. Chemical Engineering Journal, 2023, 453: 139669.

[26] Ma K, Cheung Y H, Kirlikovali K O, et al. Fibrous Zr-MOF Nanozyme Aerogels with Macro-Nanoporous Structure for Enhanced Catalytic Hydrolysis of Organophosphate Toxins[J]. Advanced Materials, 2024, 36(10): 2300951.

[27] Doan H V, Amer Hamzah H, Karikkethu Prabhakaran P, et al. Hierarchical metal-organic frameworks with macroporosity: synthesis, achievements, and challenges[J]. Nano-Micro Letters, 2019, 11: 1-33.

[28] Kitagawa S, Kitaura R, Noro S. Functional porous coordination polymers[J]. Angewandte Chemie International Edition, 2004, 43(18): 2334-2375.

[29] Shi X, Cao B, Liu J, et al. Rare-earth-based metal-organic frameworks as multifunctional platforms for catalytic conversion[J]. Small, 2021, 17(22): 2005371.

[30] Yang D X, Wang P F, Liu H Y, et al. Facile synthesis of ternary transition metal-organic framework and its stable lithium storage properties[J]. Journal of Solid State Chemistry, 2022, 309: 122947.

[31] Ghasempour H, Habibi B, Zarekarizi F, et al. Converting a Non-Porous Rare-Earth Metal-Organic Framework into a Porous Yttrium-Based NH_2-UiO-66 Network via a Linker Exchange Approach[J]. Inorganic Chemistry, 2022, 61(41): 16221-16227.

[32] Lu J, Yang L, Zhang W, et al. Photodynamic therapy for hypoxic solid tumors via Mn-MOF as a photosensitizer[J]. Chemical communications, 2019, 55(72): 10792-10795.

[33] Dou J, Zhu C, Wang H, et al. Synergistic effects of Eu-MOF on perovskite solar cells with improved stability[J]. Advanced Materials, 2021, 33(39): 2102947.

[34] Luo J, Liu B S, Cao C, et al. Neodymium (III) organic frameworks (Nd-MOF) as near infrared fluorescent probe for highly selectively sensing of Cu^{2+}[J]. Inorganic Chemistry Communications, 2017, 76: 18-21.

[35] Yan M, Ye J, Zhu Q, et al. Ultrasensitive immunosensor for cardiac troponin I detection based on the electrochemiluminescence of 2D Ru-MOF nanosheets[J]. Analytical chemistry, 2019, 91(15): 10156-10163.

[36] Guo Y, Wang W, Lei H, et al. Alternate Storage of Opposite Charges in Multisites for High-Energy-Density Al-MOF Batteries[J]. Advanced Materials, 2022, 34(13): 2110109.

[37] Jiao L, Seow J Y R, Skinner W S, et al. Metal-organic frameworks: Structures and functional applications[J]. Materials Today, 2019, 27: 43-68.

[38] Assen A H, Adil K, Cordova K E, et al. The chemistry of metal-organic frameworks with face-centered cubic topology[J]. Coordination Chemistry Reviews, 2022, 468: 214644.

[39] Zhao Z, Ma X, Li Z, et al. Synthesis, characterization and gas transport properties of MOF-5 membranes[J]. Journal of Membrane Science, 2011, 382: 82-90.

[40] Valenzano L, Civalleri B, Chavan S, et al. Disclosing the complex structure of UiO-66 metal organic framework: a synergic combination of experiment and theory[J]. Chemistry of Materials, 2011, 23(7): 1700-1718.

[41] Earnshaw A, Figgis B N, Lewis J. Chemistry of polynuclear compounds. Part VI. Magnetic properties of trimeric chromium and iron carboxylates[J]. Journal of the Chemical Society A: Inorganic, Physical, Theoretical, 1966, 1656-1663.

[42] Cavka J H, Jakobsen S, Olsbye U, et al. A new zirconium inorganic building brick forming metal organic frameworks with exceptional stability[J]. Journal of the American Chemical Society, 2008, 130(42): 13850-13851.

[43] Kandiah M, Nilsen M H, Usseglio S, et al. Synthesis and stability of tagged UiO-66 Zr-MOFs[J]. Chemistry of Materials, 2010, 22(24): 6632-6640.

[44] Shan B, McIntyre S M, Armstrong M R, et al. Investigation of missing-cluster defects in UiO-66 and ferrocene deposition into defect-induced cavities[J]. Industrial & Engineering Chemistry Research, 2018, 57(42): 14233-14241.

[45] Cox C S, Slavich E, Macreadie L K, et al. Understanding the role of synthetic parameters in the defect engineering of UiO-66: a review and meta-analysis[J]. Chemistry of Materials, 2023, 35(8): 3057-3072.

[46] Mondloch J E, Karagiaridi O, Farha O K, et al. Activation of metal-organic framework materials[J]. CrystEngComm, 2013, 15(45): 9258-9264.

[47] Lee E J, Bae J, Choi K M, et al. Exploiting microwave chemistry for activation of

metal-organic frameworks[J]. ACS Applied Materials & Interfaces, 2019, 11(38): 35155-35161.

[48] Lohe M R, Rose M, Kaskel S. Metal-organic framework (MOF) aerogels with high micro-and macroporosity[J]. Chemical Communications, 2009, 40: 6056-6058.

[49] Furukawa H, Ko N, Go Y B, et al. Ultrahigh porosity in metal-organic frameworks[J]. Science, 2010, 329(5990): 424-428.

[50] Dinca M, Long J R. Strong H_2 binding and selective gas adsorption within the microporous coordination solid $Mg_3(O_2C-C_{10}H_6-CO_2)_3$[J]. Journal of the American Chemical Society, 2005, 127(26): 9376-9377.

[51] Alhumaimess M S. Metal-organic frameworks and their catalytic applications[J]. Journal of Saudi Chemical Society, 2020, 24(6): 461-473.

[52] Szczęśniak B, Choma J, Jaroniec M. Gas adsorption properties of hybrid graphene-MOF materials[J]. Journal of colloid and interface science, 2018, 514: 801-813.

[53] Wu D, Zhang P F, Yang G P, et al. Supramolecular control of MOF pore properties for the tailored guest adsorption/separation applications[J]. Coordination Chemistry Reviews, 2021, 434: 213709.

[54] Connolly B M, Madden D G, Wheatley A E H, et al. Shaping the future of fuel: Monolithic metal-organic frameworks for high-density gas storage[J]. Journal of the American Chemical Society, 2020, 142(19): 8541-8549.

[55] Daglar H, Gulbalkan H C, Avci G, et al. Effect of metal-organic framework (MOF) database selection on the assessment of gas storage and separation potentials of MOFs[J]. Angewandte Chemie International Edition, 2021, 60(14): 7828-7837.

[56] Chae H K, Siberio-Pérez D Y, Kim J, et al. A route to high surface area, porosity and inclusion of large molecules in crystals[J]. Nature, 2004, 427(6974): 523-527.

[57] Nijkamp M G, Raaymakers J, Van Dillen A J, et al. Hydrogen storage using physisorption-materials demands[J]. Applied Physics A, 2001, 72: 619-623.

[58] Farha O K, Eryazici I, Jeong N C, et al. Metal-organic framework materials with ultrahigh surface areas: is the sky the limit[J]. Journal of the American Chemical Society, 2012, 134(36): 15016-15021.

[59] Serra-Crespo P, Ramos-Fernandez E V, Gascon J, et al. Synthesis and

characterization of an amino functionalized MIL-101 (Al): separation and catalytic properties[J]. Chemistry of Materials, 2011, 23(10): 2565-2572.

[60] Demessence A, D'Alessandro D M, Foo M L, et al. Strong CO_2 binding in a water-stable, triazolate-bridged metal-organic framework functionalized with ethylenediamine[J]. Journal of the American Chemical Society, 2009, 131(25): 8784-8786.

[61] Wang S, Lee J S, Wahiduzzaman M, et al. A robust large-pore zirconium carboxylate metal-organic framework for energy-efficient water-sorption-driven refrigeration[J]. Nature Energy, 2018, 3(11): 985-993.

[62] L u X F, Liao P Q, Wang J W, et al. An alkaline-stable, metal hydroxide mimicking metal-organic framework for efficient electrocatalytic oxygen evolution[J]. Journal of the American Chemical Society, 2016, 138(27): 8336-8339.

[63] Zhao H, Li Q, Wang Z, et al. Synthesis of MIL-101 (Cr) and its water adsorption performance[J]. Microporous and Mesoporous Materials, 2020, 297: 110044.

[64] Li Z, Liu X, Jin W, et al. Adsorption behavior of arsenicals on MIL-101 (Fe): the role of arsenic chemical structures[J]. Journal of colloid and interface science, 2019, 554: 692-704.

[65] Li S, Lei T, Jiang F, et al. Tuning the morphology and adsorption capacity of Al-MIL-101 analogues with Fe^{3+} for phosphorus removal from water[J]. Journal of Colloid and Interface Science, 2020, 560: 321-329.

[66] Yuan S, Feng L, Wang K, et al. Stable metal-organic frameworks: design, synthesis, and applications[J]. Advanced Materials, 2018, 30(37): 1704303.

[67] Ding M, Cai X, Jiang H L. Improving MOF stability: approaches and applications[J]. Chemical Science, 2019, 10(44): 10209-10230.

[68] Mai Z, Liu D. Synthesis and applications of iso-reticular metal-organic frameworks IRMOFs-n (n=1, 3, 6, 8)[J]. Crystal Growth & Design, 2019, 19(12): 7439-7462.

[69] Surblé S, Millange F, Serre C, et al. An EXAFS study of the formation of a nanoporous metal-organic framework: evidence for the retention of secondary building units during synthesis[J]. Chemical Communications, 2006, 14: 1518-1520.

[70] Janiak C, Vieth J K. MOFs, MILs and more: concepts, properties and applications for porous coordination networks (PCNs)[J]. New Journal of Chemistry, 2010, 34(11): 2366-2388.

[71] Winarta J, Shan B, Mcintyre S M, et al. A decade of UiO-66 research: a historic review of dynamic structure, synthesis mechanisms, and characterization techniques of an archetypal metal-organic framework[J]. Crystal Growth & Design, 2019, 20(2): 1347-1362.

[72] DeCoste J B, Peterson G W, Schindler B J, et al. The effect of water adsorption on the structure of the carboxylate containing metal-organic frameworks Cu-BTC, Mg-MOF-74, and UiO-66[J]. Journal of Materials Chemistry A, 2013, 1(38): 11922-11932.

[73] Ahmadijokani F, Mohammadkhani R, Ahmadipouya S, et al. Superior chemical stability of UiO-66 metal-organic frameworks (MOFs) for selective dye adsorption[J]. Chemical Engineering Journal, 2020, 399: 125346.

[74] Biswas S, Zhang J, Li Z, et al. Enhanced selectivity of CO_2 over CH_4 in sulphonate, carboxylate and iodo-functionalized UiO-66 frameworks[J]. Dalton Transactions, 2013, 42(13): 4730-4737.

[75] Chavan S M, Shearer G C, Svelle S, et al. Synthesis and characterization of amine-functionalized mixed-ligand metal-organic frameworks of UiO-66 topology[J]. Inorganic chemistry, 2014, 53(18): 9509-9515.

[76] Hu Z, Peng Y, Kang Z, et al. A modulated hydrothermal (MHT) approach for the facile synthesis of UiO-66-type MOFs[J]. Inorganic chemistry, 2015, 54(10): 4862-4868.

[77] Ahmadijokani F, Molavi H, Rezakazemi M, et al. UiO-66 metal-organic frameworks in water treatment: A critical review[J]. Progress in Materials Science, 2022, 125: 100904.

[78] Kadhom M, Al-Furaiji M, Salih S, et al. A review on UiO-66 applications in membrane-based water treatment processes[J]. Journal of Water Process Engineering, 2023, 51: 103402.

[79] Pourmadadi M, Eshaghi M M, Ostovar S, et al. UiO-66 metal-organic framework nanoparticles as gifted MOFs to the biomedical application: A comprehensive review[J].

Journal of Drug Delivery Science and Technology, 2022, 76: 103758.

[80] Yang F, Li W, Tang B. Facile synthesis of amorphous UiO-66 (Zr-MOF) for supercapacitor application[J]. Journal of Alloys and Compounds, 2018, 733: 8-14.

[81] Wang Y, Wang S, Li Z, et al. Synthesis of UiO-66 in supercritical CO_2 and its application in dye adsorption[J]. Industrial & Engineering Chemistry Research, 2020, 60(1): 771-780.

[82] Jarai B M, Stillman Z, Attia L, et al. Evaluating UiO-66 metal-organic framework nanoparticles as acid-sensitive carriers for pulmonary drug delivery applications[J]. ACS Applied Materials & Interfaces, 2020, 12(35): 38989-39004.

[83] Li M Y, Liu J, Gao R, et al. Design and synthesis of zeolitic tetrazolate-imidazolate frameworks[J]. Materials Today Advances, 2021, 10: 100145.

[84] Huang X, Zhang J, Chen X. $[Zn(bim)_2]\cdot(H_2O)_{1.67}$: A metal-organic open-framework with sodalite topology[J]. Chinese Science Bulletin, 2003, 48: 1531-1534.

[85] Bibi S, Pervaiz E, Ali M. Synthesis and applications of metal oxide derivatives of ZIF-67: a mini-review[J]. Chemical Papers, 2021, 75: 2253-2275.

[86] Huang X C, Lin Y Y, Zhang J P, et al. Ligand-directed strategy for zeolite-type metal-organic frameworks: zinc (II) imidazolates with unusual zeolitic topologies[J]. Angewandte Chemie International Edition, 2006, 45(10): 1557-1559.

[87] Chen B, Yang Z, Zhu Y, et al. Zeolitic imidazolate framework materials: recent progress in synthesis and applications[J]. Journal of Materials Chemistry A, 2014, 2(40): 16811-16831.

[88] Küsgens P, Rose M, Senkovska I, et al. Characterization of metal-organic frameworks by water adsorption[J]. Microporous and Mesoporous Materials, 2009, 120(3): 325-330.

[89] Bux H, Liang F, Li Y, et al. Zeolitic imidazolate framework membrane with molecular sieving properties by microwave-assisted solvothermal synthesis[J]. Journal of the American Chemical Society, 2009, 131(44): 16000-16001.

[90] Banerjee R, Phan A, Wang B, et al. High-throughput synthesis of zeolitic imidazolate frameworks and application to CO_2 capture[J]. Science, 2008, 319(5865): 939-943.

[91] Ighalo J O, Rangabhashiyam S, Adeyanju C A, et al. Zeolitic imidazolate frameworks (ZIFs) for aqueous phase adsorption-a review[J]. Journal of Industrial and Engineering Chemistry, 2022, 105: 34-48.

[92] Mohamud M A, Yurtcan A B. Zeolotic imidazolate frameworks (ZIFs) derived porous carbon: A review from crystal growth & green synthesis to oxygen reduction reaction activity[J]. International Journal of Hydrogen Energy, 2021, 46(68): 33782-33800.

[93] Kukkar P, Kim K H, Kukkar D, et al. Recent advances in the synthesis techniques for zeolitic imidazolate frameworks and their sensing applications[J]. Coordination Chemistry Reviews, 2021, 446: 214109.

[94] Park K S, Ni Z, Côté A P, et al. Exceptional chemical and thermal stability of zeolitic imidazolate frameworks[J]. Proceedings of the National Academy of Sciences, 2006, 103(27): 10186-10191.

[95] Huang A, Chen Y, Wang N, et al. A highly permeable and selective zeolitic imidazolate framework ZIF-95 membrane for H_2/CO_2 separation[J]. Chemical Communications, 2012, 48(89): 10981-10983.

[96] Zhou S, Yue P, Huang J, et al. High-performance photoelectrochemical water splitting of $BiVO_4$@Co-MIm prepared by a facile in-situ deposition method[J]. Chemical Engineering Journal, 2019, 371: 885-892.

[97] Zhong G, Liu D, Zhang J. The application of ZIF-67 and its derivatives: adsorption, separation, electrochemistry and catalysts[J]. Journal of Materials Chemistry A, 2018, 6(5): 1887-1899.

[98] Phan A, Doonan C J, Uribe-Romo F J, et al. Synthesis, structure, and carbon dioxide capture properties of zeolitic imidazolate frameworks[J]. Accounts of chemical research, 2010, 43: 58-67.

[99] Lai Z. Development of ZIF-8 membranes: opportunities and challenges for commercial applications[J]. Current Opinion in Chemical Engineering, 2018, 20: 78-85.

[100] Hoop M, Walde C F, Riccò R, et al. Biocompatibility characteristics of the metal organic framework ZIF-8 for therapeutical applications[J]. Applied Materials Today,

2018, 11: 13-21.

[101] Safaei M, Foroughi M M, Ebrahimpoor N, et al. A review on metal-organic frameworks: Synthesis and applications[J]. TrAC Trends in Analytical Chemistry, 2019, 118: 401-425.

[102] Stock N, Biswas S. Synthesis of metal-organic frameworks (MOFs): routes to various MOF topologies, morphologies, and composites[J]. Chemical Reviews, 2012, 112(2): 933-969.

[103] Wu X, Bao Z, Yuan B, et al. Microwave synthesis and characterization of MOF-74 (M= Ni, Mg) for gas separation[J]. Microporous and Mesoporous Materials, 2013, 180: 114-122.

[104] Lv D, Chen Y, Li Y, et al. Efficient mechanochemical synthesis of MOF-5 for linear alkanes adsorption[J]. Journal of Chemical & Engineering Data, 2017, 62(7): 2030-2036.

[105] de Lima Neto O J, de Oliveira Frós A C, Barros B S, et al. Rapid and efficient electrochemical synthesis of a zinc-based nano-MOF for Ibuprofen adsorption[J]. New Journal of Chemistry, 2019, 43(14): 5518-5524.

[106] Yoshimura M, Byrappa K. Hydrothermal processing of materials: past, present and future[J]. Journal of Materials Science, 2008, 43: 2085-2103.

[107] Férey G. Metal-organic frameworks: the young child of the porous solids family[M] Studies in surface science and catalysis. Elsevier, 2007, 170: 66-84.

[108] Rabenau A. The role of hydrothermal synthesis in preparative chemistry[J]. Angewandte Chemie International Edition in English, 1985, 24(12): 1026-1040.

[109] Lee Y R, Kim J, Ahn W S. Synthesis of metal-organic frameworks: A mini review[J]. Korean Journal of Chemical Engineering, 2013, 30: 1667-1680.

[110] Jung D W, Yang D A, Kim J, et al. Facile synthesis of MOF-177 by a sonochemical method using 1-methyl-2-pyrrolidinone as a solvent[J]. Dalton Transactions, 2010, 39(11): 2883-2887.

[111] Marino P, Donnarumma P R, Bicalho H A, et al. A step toward change: a green alternative for the synthesis of metal-organic frameworks[J]. ACS Sustainable Chemistry & Engineering, 2021, 9(48): 16356-16362.

[112] Feng X, Wu T, Carreon M A. Synthesis of ZIF-67 and ZIF-8 crystals using DMSO (Dimethyl Sulfoxide) as solvent and kinetic transformation studies[J]. Journal of Crystal Growth, 2016, 455: 152-156.

[113] Bauer S, Serre C, Devic T, et al. High-throughput assisted rationalization of the formation of metal organic frameworks in the iron (III) aminoterephthalate solvothermal system[J]. Inorganic Chemistry, 2008, 47(17): 7568-7576.

[114] Łuczak J, Kroczewska M, Baluk M, et al. Morphology control through the synthesis of metal-organic frameworks[J]. Advances in Colloid and Interface Science, 2023, 314: 102864.

[115] McKinstry C, Cathcart R J, Cussen E J, et al. Scalable continuous solvothermal synthesis of metal organic framework (MOF-5) crystals[J]. Chemical Engineering Journal, 2016, 285: 718-725.

[116] Bhoite A A, Patil K V, Redekar R S, et al. Solvothermal synthesis of binder free Ni-MOF thin films for supercapacitor electrodes[J]. Journal of Solid State Chemistry, 2023, 326: 124192.

[117] Clausen H F, Poulsen R D, Bond A D, et al. Solvothermal synthesis of new metal organic framework structures in the zinc-terephthalic acid-dimethyl formamide system[J]. Journal of Solid State Chemistry, 2005, 178(11): 3342-3351.

[118] Sud D, Kaur G. A comprehensive review on synthetic approaches for metal-organic frameworks: From traditional solvothermal to greener protocols[J]. Polyhedron, 2021, 193: 114897.

[119] Al Amery N, Abid H R, Al-Saadi S, et al. Facile directions for synthesis, modification and activation of MOFs[J]. Materials Today Chemistry, 2020, 17: 100343.

[120] Shi X, Zhu G, Qiu S, et al. $Zn_2[(S)-O_3PCH_2NHC_4H_7CO_2]_2$: a homochiral 3D zinc phosphonate with helical channels[J]. Angewandte Chemie International Edition, 2004, 43(47): 6482-6485.

[121] Scailteur V, Lauwerys R R. Dimethylformamide (DMF) hepatotoxicity[J]. Toxicology, 1987, 43(3): 231-238.

[122] Muzart J. N, N-Dimethylformamide: much more than a solvent[J]. Tetrahedron, 2009, 65(40): 8313-8323.

[123] Tompsett G A, Conner W C, Yngvesson K S. Microwave synthesis of nanoporous materials[J]. ChemPhysChem, 2006, 7(2): 296-319.

[124] Couzon N, Ferreira M, Duval S, et al. Microwave-assisted synthesis of porous composites MOF-textile for the protection against chemical and nuclear hazards[J]. ACS Applied Materials & Interfaces, 2022, 14(18): 21497-21508.

[125] Klinowski J, Paz F A , Silva P, et al. Microwave-assisted synthesis of metal-organic frameworks[J]. Dalton Transactions, 2011, 40(2): 321-330.

[126] Ge J, Wu Z, Huang X, et al. An Effective Microwave-Assisted Synthesis of MOF-235 with Excellent Adsorption of Acid Chrome Blue K[J]. Journal of Nanomaterials, 2019, 1: 4035075.

[127] Ni Z, Masel R I. Rapid production of metal-organic frameworks via microwave-assisted solvothermal synthesis[J]. Journal of the American Chemical Society, 2006, 128(38): 12394-12395.

[128] Babu R, Roshan R, Kathalikkattil A C, et al. Rapid, microwave-assisted synthesis of cubic, three-dimensional, highly porous MOF-205 for room temperature CO_2 fixation via cyclic carbonate synthesis[J]. ACS Applied Materials & Interfaces, 2016, 8(49): 33723-33731.

[129] Thomas-Hillman I, Laybourn A, Dodds C, et al. Realising the environmental benefits of metal-organic frameworks: recent advances in microwave synthesis[J]. Journal of Materials Chemistry A, 2018, 6(25): 11564-11581.

[130] Chen C, Feng X, Zhu Q, et al. Microwave-assisted rapid synthesis of well-shaped MOF-74(Ni) for CO_2 efficient capture[J]. Inorganic Chemistry, 2019, 58(4): 2717-2728.

[131] Solís R R, Gómez-Avilés A, Belver C, et al. Microwave-assisted synthesis of NH_2-MIL-125(Ti) for the solar photocatalytic degradation of aqueous emerging pollutants in batch and continuous tests[J]. Journal of Environmental Chemical Engineering, 2021, 9(5): 106230.

[132] Taddei M, Steitz D A, van Bokhoven J A, et al. Continuous-flow microwave synthesis of metal-organic frameworks: a highly efficient method for large-scale production[J]. Chemistry-A European Journal, 2016, 22(10): 3245-3249.

[133] Kaupp G. Mechanochemistry: the varied applications of mechanical bond-

breaking[J]. CrystEngComm, 2009, 11(3): 388-403.

[134] Szczęśniak B, Borysiuk S, Choma J, et al. Mechanochemical synthesis of highly porous materials[J]. Materials Horizons, 2020, 7(6): 1457-1473.

[135] Beamish-Cook J, Shankland K, Murray C A, et al. Insights into the Mechanochemical Synthesis of MOF-74[J]. Crystal Growth & Design, 2021, 21(5): 3047-3055.

[136] Głowniak S, Szczęśniak B, Choma J, et al. Mechanochemistry: Toward green synthesis of metal-organic frameworks[J]. Materials Today, 2021, 46: 109-124.

[137] Ayoub G, Karadeniz B, Howarth A J, et al. Rational synthesis of mixed-metal microporous metal-organic frameworks with controlled composition using mechanochemisty[J]. Chemistry of Materials, 2019, 31(15): 5494-5501.

[138] Zhou S, Shekhah O, Jia J, et al. Electrochemical synthesis of continuous metal-organic framework membranes for separation of hydrocarbons[J]. Nature Energy, 2021, 6(9): 882-891.

[139] Ren H, Wei T. Electrochemical synthesis methods of metal-organic frameworks and their environmental analysis applications: a review[J]. ChemElectroChem, 2022, 9(13): e202200196.

[140] Van Assche T R C, Desmet G, Ameloot R, et al. Electrochemical synthesis of thin HKUST-1 layers on copper mesh[J]. Microporous and Mesoporous Materials, 2012, 158: 209-213.

[141] Son W J, Kim J, Kim J, et al. Sonochemical synthesis of MOF-5[J]. Chemical Communications, 2008, 47: 6336-6338.

[142] Calvo Galve N, Abrishamkar A, Sorrenti A, et al. Exploiting reaction-diffusion conditions to trigger pathway complexity in the growth of a MOF[J]. Angewandte Chemie, 2021, 133(29): 16056-16063.

[143] Azbell T J, Pitt T A, Bollmeyer M M, et al. Ionothermal Synthesis of Metal-Organic Frameworks Using Low-Melting Metal Salt Precursors[J]. Angewandte Chemie International Edition, 2023, 62(17): e202218252.

[144] Shang W, Kang X, Ning H, et al. Shape and size controlled synthesis of MOF nanocrystals with the assistance of ionic liquid mircoemulsions[J]. Langmuir, 2013,

29(43): 13168-13174.

[145] Gangu K K, Maddila S, Mukkamala S B, et al. A review on contemporary metal-organic framework materials[J]. Inorganica Chimica Acta, 2016, 446: 61-74.

[146] Wang S, McGuirk C M, d'Aquino A, et al. Metal-organic framework nanoparticles[J]. Advanced Materials, 2018, 30(37): 1800202.

[147] Darabdhara J, Ahmaruzzaman M. Recent developments in MOF and MOF based composite as potential adsorbents for removal of aqueous environmental contaminants[J]. Chemosphere, 2022, 304: 135261.

[148] Bux H, Chmelik C, Krishna R, et al. Ethene/ethane separation by the MOF membrane ZIF-8: Molecular correlation of permeation, adsorption, diffusion[J]. Journal of Membrane Science, 2011, 369: 284-289.

[149] Tonnah R K, Chai M, Abdollahzadeh M, et al. Bioinspired angstrom-scale heterogeneous MOF-on-MOF membrane for osmotic energy harvesting[J]. ACS Nano, 2023, 17(13): 12445-12457.

[150] Erçarıkcı E, Dağcı Kıranşan K, Topçu E. Three-dimensional ZnCo-MOF modified graphene sponge: flexible electrode material for symmetric supercapacitor[J]. Energy & Fuels, 2022, 36(3): 1735-1745.

[151] Shi M, Lin D, Huang R, et al. Construction of a mercapto-functionalized Zr-MOF/melamine sponge composite for the efficient removal of oils and heavy metal ions from water[J]. Industrial & Engineering Chemistry Research, 2020, 59(29): 13220-13227.

[152] Yao Y, Wang C, Na J, et al. Macroscopic MOF architectures: Effective strategies for practical application in water treatment[J]. Small, 2022, 18(8): 2104387.

[153] Hu M L, Masoomi M Y, Morsali A. Template strategies with MOFs[J]. Coordination Chemistry Reviews, 2019, 387: 415-435.

[154] Li K, Yang J, Gu J. Hierarchically porous MOFs synthesized by soft-template strategies[J]. Accounts of Chemical Research, 2022, 55(16): 2235-2247.

[155] Kim H, Lah M S. Templated and template-free fabrication strategies for zero-dimensional hollow MOF superstructures[J]. Dalton Transactions, 2017, 46(19): 6146-6158.

[156] Zhao N, Cai K, He H. The synthesis of metal-organic frameworks with template strategies[J]. Dalton Transactions, 2020, 49(33): 11467-11479.

[157] Shen K, Zhang L, Chen X, et al. Ordered macro-microporous metal-organic framework single crystals[J]. Science, 2018, 359(6372): 206-210.

[158] Zhao Z, Ding J, Zhu R, et al. The synthesis and electrochemical applications of core-shell MOFs and their derivatives[J]. Journal of Materials Chemistry A, 2019, 7(26): 15519-15540.

[159] Liu M, Xing Z, Li Z, et al. Recent advances in core-shell metal organic frame-based photocatalysts for solar energy conversion[J]. Coordination Chemistry Reviews, 2021, 446: 214123.

[160] Dai S, Tissot A, Serre C. Recent progresses in metal-organic frameworks based core-shell composites[J]. Advanced Energy Materials, 2022, 12(4): 2100061.

[161] del Rio M, Escarabajal J C G, Palomino G T, et al. Zinc/Iron mixed-metal MOF-74 derived magnetic carbon nanorods for the enhanced removal of organic pollutants from water[J]. Chemical Engineering Journal, 2022, 428: 131147.

[162] Huang X, Yan S, Deng D, et al. Novel strategy for engineering the metal-oxide@ MOF core@ shell architecture and its applications in cataluminescence sensing[J]. ACS Applied Materials & Interfaces, 2021, 13(2): 3471-3480.

[163] Subudhi S, Tripathy S P, Parida K. Metal oxide integrated metal organic frameworks (MOF@MOF): rational design, fabrication strategy, characterization and emerging photocatalytic applications[J]. Inorganic Chemistry Frontiers, 2021, 8(6): 1619-1636.

[164] Tang J, Salunkhe R R, Liu J, et al. Thermal conversion of core-shell metal-organic frameworks: a new method for selectively functionalized nanoporous hybrid carbon[J]. Journal of the American Chemical Society, 2015, 137(4): 1572-1580.

[165] Wu C H, Yun W C, Wi-Afedzi T, et al. ZIF-67 supported on marcoscale resin as an efficient and convenient heterogeneous catalyst for Oxone activation[J]. Journal of Colloid and Interface Science, 2018, 514: 262-271.

[166] Valiza deh B, Nguyen T N, Smit B, et al. Porous metal-organic framework@ polymer beads for iodine capture and recovery using a gas-sparged column[J].

Advanced Functional Materials, 2018, 28(30): 1801596.

[167] Zhao R, Ma T, Zhao S, et al. Uniform and stable immobilization of metal-organic frameworks into chitosan matrix for enhanced tetracycline removal from water[J]. Chemical Engineering Journal, 2020, 382: 122893.

[168] Lu A X, Ploskonka A M, Tovar T M, et al. Direct surface growth of UiO-66-NH$_2$ on polyacrylonitrile nanofibers for efficient toxic chemical removal[J]. Industrial & Engineering Chemistry Research, 2017, 56(49): 14502-14506.

[169] Zhou Z, Xu L, Ding Y, et al. Atomic layer deposition meets metal-organic frameworks[J]. Progress in Materials Science, 2023, 138: 101159.

[170] Zhang Z, Zhao Y, Zhao Z, et al. Atomic layer deposition-derived nanomaterials: oxides, transition metal dichalcogenides, and metal-organic frameworks[J]. Chemistry of Materials, 2020, 32(21): 9056-9077.

[171] Zhao J, Losego M D, Lemaire P C, et al. Highly adsorptive, MOF-functionalized nonwoven fiber mats for hazardous gas capture enabled by atomic layer deposition[J]. Advanced Materials Interfaces, 2014, 1(4): 1400040.

[172] Lee D T, Dai Z, Peterson G W, et al. Highly Breathable Chemically Protective MOF-Fiber Catalysts[J]. Advanced Functional Materials, 2022, 32(6): 2108004.

[173] Abbasi A R, Akhbari K, Morsali A. Dense coating of surface mounted CuBTC metal-organic framework nanostructures on silk fibers, prepared by layer-by-layer method under ultrasound irradiation with antibacterial activity[J]. Ultrasonics Sonochemistry, 2012, 19(4): 846-852.

[174] Li W, Zhang Y, Yu Z, et al. In situ growth of a stable metal-organic framework (MOF) on flexible fabric via a layer-by-layer strategy for versatile applications[J]. ACS Nano, 2022, 16(9): 14779-14791.

[175] Li Y, Zhu J, Cheng H, et al. Developments of advanced electrospinning techniques: A critical review[J]. Advanced Materials Technologies, 2021, 6(11): 2100410.

[176] Bhardwaj N, Kundu S C. Electrospinning: A fascinating fiber fabrication technique[J]. Biotechnology Advances, 2010, 28(3): 325-347.

[177] Figen A K. History, basics, and parameters of electrospinning technique[J].

Electrospun Materials and Their Allied Applications, 2020, 2: 53-69.

[178] Ahmed F E, Lalia B S, Hashaikeh R. A review on electrospinning for membrane fabrication: Challenges and applications[J]. Desalination, 2015, 356: 15-30.

[179] Lu A X, McEntee M, Browe M A, et al. MOFabric: electrospun nanofiber mats from PVDF/UiO-66-NH$_2$ for chemical protection and decontamination[J]. ACS Applied Materials & Interfaces, 2017, 9(15): 13632-13636.

[180] Zhang Y, Yuan S, Feng X, et al. Preparation of nanofibrous metal-organic framework filters for efficient air pollution control[J]. Journal of the American Chemical Society, 2016, 138(18): 5785-5788.

[181] Bai Y, Liu C, Shan Y, et al. Metal-organic frameworks nanocomposites with different dimensionalities for energy conversion and storage[J]. Advanced Energy Materials, 2022, 12(4): 2100346.

[182] Ariyamparambil V J, Kandasubramanian B. A mini-review on the recent advancement of electrospun MOF-derived nanofibers for energy storage[J]. Chemical Engineering Journal Advances, 2022, 11: 100355.

[183] Zhao R, Tian Y, Li S, et al. An electrospun fiber based metal-organic framework composite membrane for fast, continuous, and simultaneous removal of insoluble and soluble contaminants from water[J]. Journal of Materials Chemistry A, 2019, 7(39): 22559-22570.

[184] Wang C, Cheng P, Yao Y, et al. In-situ fabrication of nanoarchitectured MOF filter for water purification[J]. Journal of Hazardous Materials, 2020, 392: 122164.

[185] Ahmadijokani F, Molavi H, Bahi A, et al. Metal-Organic Frameworks and Electrospinning: A Happy Marriage for Wastewater Treatment[J]. Advanced Functional Materials, 2022, 32(51): 2207723.

[186] Liu L, Yu R, Yin L, et al. Porous organic framework membranes based on interface-induced polymerisation: design, synthesis and applications[J]. Chemical Science, 2024, 15(6): 1924-1937.

[187] Li Y, Wee L H, Volodin A, et al. Polymer supported ZIF-8 membranes prepared via an interfacial synthesis method[J]. Chemical Communications, 2015, 51(5): 918-920.

[188] Hu Q, Xu L, Fu K, et al. Ultrastable MOF-based foams for versatile applications[J]. Nano Research, 2021, 15(4): 2961-2970.

[189] Guo R, Cai X, Liu H, et al. In situ growth of metal-organic frameworks in three-dimensional aligned lumen arrays of wood for rapid and highly efficient organic pollutant removal[J]. Environmental Science & Technology, 2019, 53(5): 2705-2712.

[190] Ren W, Gao J, Lei C, et al. Recyclable metal-organic framework/cellulose aerogels for activating peroxymonosulfate to degrade organic pollutants[J]. Chemical Engineering Journal, 2018, 349: 766-774.

[191] Lohe M R, Rose M, Kaskel S. Metal-organic framework (MOF) aerogels with high micro-and macroporosity[J]. Chemical Communications, 2009, 40: 6056-6058.

[192] Zhang H, Zhao W, Zou M, et al. 3D, mutually embedded MOF@carbon nanotube hybrid networks for high-performance lithium-sulfur batteries[J]. Advanced Energy Materials, 2018, 8(19): 1800013.

[193] Yang Y, Guo Y, Qiu Z, et al. In situ growth of Zr-based metal-organic frameworks on cellulose sponges for Hg^{2+} and methylene blue removal[J]. Carbohydrate Polymers, 2024, 328: 121750.

[194] Hong D H, Shim H S, Ha J, et al. MOF-on-MOF architectures: applications in separation, catalysis, and sensing[J]. Bulletin of the Korean Chemical Society, 2021, 42(7): 956-969.

[195] Cheng P, Wang C, Kaneti Y V, et al. Practical MOF nanoarchitectonics: new strategies for enhancing the processability of MOFs for practical applications[J]. Langmuir, 2020, 36(16): 4231-4249.

[196] Campanati M, Fornasari G, Vaccari A. Fundamentals in the preparation of heterogeneous catalysts[J]. Catalysis Today, 2003, 77(4): 299-314.

[197] Kaur M, Kumar S, Younis S A, et al. Post synthesis modification of metal-organic frameworks using Schiff base complexes for various catalytic applications[J]. Chemical Engineering Journal, 2021, 423: 130230.

[198] Ma D, Li B, Shi Z. Multi-functional sites catalysts based on post-synthetic modification of metal-organic frameworks[J]. Chinese Chemical Letters, 2018, 29(6): 827-830.

[199] Dang M H D, Nguyen T, Le B Q G, et al. An effective combination of reusable Pd@MOF catalyst and deep eutectic solvents for high-performance C-C coupling reaction[J]. Journal of Industrial and Engineering Chemistry, 2022, 111: 111-120.

[200] Xu Z, Zhao G, Hedin N, et al. Fast Catalytic Esterification Using a Hydrophobized Zr-MOF with Acidic Ionic Liquid Linkers[J]. ChemistrySelect, 2020, 5(3): 1153-1156.

[201] Mahato D, Fajal S, Samanta P, et al. Selective and Sensitive Fluorescence Turn-On Detection of Cyanide Ions in Water by Post Metallization of a MOF[J]. ChemPlusChem, 2022, 87(1): e202100426.

[202] Hou S L, Dong J, Jiang X L, et al. A noble-metal-free metal-organic framework (MOF) catalyst for the highly efficient conversion of CO_2 with propargylic alcohols[J]. Angewandte Chemie International Edition, 2019, 58(2): 577-581.

[203] Chen H, Ma R, Zhang Y, et al. A Stable Triphenylamine-Based Zn(II)-MOF for Photocatalytic H_2 Evolution and Photooxidative Carbon-Carbon Coupling Reaction[J]. Inorganic Chemistry, 2023, 62(20): 7954-7963.

[204] Lee Y R, Chung Y M, Ahn W S. A new site-isolated acid-base bifunctional metal-organic framework for one-pot tandem reaction[J]. RSC Advances, 2014, 4(44): 23064-23067.

[205] Zhou K, Liu M, Zhao Z, et al. Triflate-Functionalized UiO-66 Metal-Organic Framework Nanoparticles for Tandem Synthesis of Xanthones[J]. ACS Applied Nano Materials, 2024, 7: 13367-13378.

[206] Darabdhara J, Ahmaruzzaman M. Recent developments in MOF and MOF based composite as potential adsorbents for removal of aqueous environmental contaminants[J]. Chemosphere, 2022, 304: 135261.

[207] Yu S, Pang H, Huang S, et al. Recent advances in metal-organic framework membranes for water treatment: A review[J]. Science of the Total Environment, 2021, 800: 149662.

[208] Nimbalkar M N, Bhat B R. Simultaneous adsorption of methylene blue and heavy metals from water using Zr-MOF having free carboxylic group[J]. Journal of Environmental Chemical Engineering, 2021, 9(5): 106216.

[209] Liu L, Fang Y, Meng Y, et al. Efficient adsorbent for recovering uranium from seawater prepared by grafting amidoxime groups on chloromethylated MIL-101(Cr) via diaminomaleonitrile intermediate[J]. Desalination, 2020, 478: 114300.

[210] Li H, Cao X, Zhang C, et al. Enhanced adsorptive removal of anionic and cationic dyes from single or mixed dye solutions using MOF PCN-222[J]. RSC advances, 2017, 7(27): 16273-16281.

[211] Teo W E, Ramakrishna S. A review on electrospinning design and nanofiber assemblies[J]. Nanotechnology, 2006, 17(14): R89.

[212] Bhardwaj N, Kundu S C. Electrospinning: A fascinating fiber fabrication technique[J]. Biotechnology Advances, 2010, 28(3): 325-347.

[213] Subbiah T, Bhat G S, Tock R W, et al. Electrospinning of nanofibers[J]. Journal of Applied Polymer Science, 2005, 96(2): 557-569.

[214] Rutledge G C, Fridrikh S V. Formation of fibers by electrospinning[J]. Advanced Drug Delivery Reviews, 2007, 59(14): 1384-1391.

[215] Angammana C J, Jayaram S H. Fundamentals of electrospinning and processing technologies[J]. Particulate Science and Technology, 2016, 34(1): 72-82.

[216] Keirouz A, Wang Z, Reddy V S, et al. The history of electrospinning: Past, present, and future developments[J]. Advanced Materials Technologies, 2023, 8(11): 2201723.

[217] Agarwal S, Greiner A, Wendorff J H. Functional materials by electrospinning of polymers[J]. Progress in Polymer Science, 2013, 38(6): 963-991.

[218] Xue J, Wu T, Dai Y, et al. Electrospinning and electrospun nanofibers: Methods, materials, and applications[J]. Chemical Reviews, 2019, 119(8): 5298-5415.

[219] Greiner A, Wendorff J H. Electrospinning: a fascinating method for the preparation of ultrathin fibers[J]. Angewandte Chemie International Edition, 2007, 46(30): 5670-5703.

[220] Chew S Y, Wen J, Yim E K F, et al. Sustained release of proteins from electrospun biodegradable fibers[J]. Biomacromolecules, 2005, 6(4): 2017-2024.

[221] Zhao W, Liu W, Li J, et al. Preparation of animal polysaccharides nanofibers by electrospinning and their potential biomedical applications[J]. Journal of Biomedical Materials Research Part A, 2015, 103(2): 807-818.

[222] Shi X, Zhou W, Ma D, et al. Electrospinning of nanofibers and their applications for energy devices[J]. Journal of Nanomaterials, 2015, 2015(1): 140716.

[223] Aman Mohammadi M, Hosseini S M, Yousefi M. Application of electrospinning technique in development of intelligent food packaging: A short review of recent trends[J]. Food Science & Nutrition, 2020, 8(9): 4656-4665.

[224] Agarwal S, Wendorff J H, Greiner A. Use of electrospinning technique for biomedical applications[J]. Polymer, 2008, 49(26): 5603-5621.

[229] Zong D, Zhang X, Yin X, et al. Electrospun fibrous sponges: principle, fabrication, and applications[J]. Advanced Fiber Materials, 2022, 4(6): 1434-1462.

[225] Xu T, Ding Y, Liang Z, et al. Three-dimensional monolithic porous structures assembled from fragmented electrospun nanofiber mats/membranes: Methods, properties, and applications[J]. Progress in Materials Science, 2020, 112: 100656.

[226] Li Y, Wang J, Qian D, et al. Electrospun fibrous sponge via short fiber for mimicking 3D ECM[J]. Journal of Nanobiotechnology, 2021, 19(1): 131.

[227] Chen W, Xu Y, Liu Y, et al. Three-dimensional printed electrospun fiber-based scaffold for cartilage regeneration[J]. Materials & Design, 2019, 179: 107886.

[228] Xu W, Ma J, Jabbari E. Material properties and osteogenic differentiation of marrow stromal cells on fiber-reinforced laminated hydrogel nanocomposites[J]. Acta Biomaterialia, 2010, 6(6): 1992-2002.

[229] Dong X, Cao L, Si Y, et al. Cellular structured CNTs@SiO$_2$ nanofibrous aerogels with vertically aligned vessels for salt-resistant solar desalination[J]. Advanced Materials, 2020, 32(34): 1908269.

[230] Zhang F, Si Y, Yu J, et al. Sub-Nanoporous Engineered Fibrous Aerogel Molecular Sieves with Nanogating Channels for Reversible Molecular Separation[J]. Small, 2022, 18(25): 2202173.

[231] Si Y, Yu J, Tang X, et al. Ultralight nanofiber-assembled cellular aerogels with super elasticity and multifunctionality[J]. Nature Communications, 2014, 5(1): 5802.

[232] Xu T, Wang Z, Ding Y, et al. Ultralight electrospun cellulose sponge with super-high capacity on absorption of organic compounds[J]. Carbohydrate Polymers, 2018, 179: 164-172.

[233] Duan G, Jiang S, Jérôme V, et al. Ultralight, soft polymer sponges by self-assembly of short electrospun fibers in colloidal dispersions[J]. Advanced Functional Materials, 2015, 25(19): 2850-2856.

[234] Chen Y, Shafiq M, Liu M, et al. Advanced fabrication for electrospun three-dimensional nanofiber aerogels and scaffolds[J]. Bioactive Materials, 2020, 5(4): 963-979.

[235] Han S, Nie K, Li J, et al. 3D Electrospun Nanofiber-Based Scaffolds: From Preparations and Properties to Tissue Regeneration Applications[J]. Stem Cells International, 2021, 1: 8790143.

2. Aim and Overview of the Thesis

Aim

The aim of this work is to develop reproducible methods for creating zero-dimensional (0D), one/two-dimensional (1D/2D), and three-dimensional (3D) functional macroscopic metal-organic frameworks (MOFs) materials, enabling their repeated use and facilitating easy separation from the reaction medium after use. The proof-of-concept is demonstrated by showcasing their applicability as catalysts in one-pot reactions for multiple cycles and water purification. Their ultra-high porosity, large specific surface area, structural diversity, and excellent chemical stability make MOFs valuable in fields such as catalysis, gas separation and adsorption, sensing, energy storage, and biomedicine. However, the nanoparticle powder form of MOFs, coupled with their insolubility and processing challenges, limits their full potential. Moreover, the loss of MOF nanoparticles during use can lead to pipeline blockages and secondary pollution. To address these challenges and extend the service life of MOFs, appropriate processing methods can be employed to transform MOF nanoparticles into macroscopic materials. Additionally, combining MOFs with various functional components can impart new physical and chemical properties, thereby broadening their range of applications. Therefore, the objective of this work is to establish processes for making MOF macroscopic materials focusing on the preparation of functional 0D (hydrogen-bonded organic framework (HOF)-on-Fe_3O_4/ZIF-67, magnetically separable particles), 1D/2D (UiO-66-SO_3H and UiO-66-NH_2 membranes), and 3D (PI/PAN@ZIF-67 sponge) macroscopic MOFs using solvothermal, electrospinning, freeze-drying methods. The utility of these macroscopic MOF materials is studied through their application as acid-functional and base-functional membranes, serving as Wolf-Lamb type catalysts in catalyzing cascade organic reactions multiple times. Additionally, the effectiveness of 0D and 3D macroscopic MOF materials in activating peroxymonosulfate (PMS) for the degradation of organic pollutants in waste is studied. The results are presented in a cumulative thesis format, including two published articles

in peer-reviewed journals (ChemCatChem, Advanced Energy and Sustainability Research) and one manuscript ready for submission. (section 2.1 to section 2.3). A summary diagram of the thesis work is shown in **Figure 2-1**.
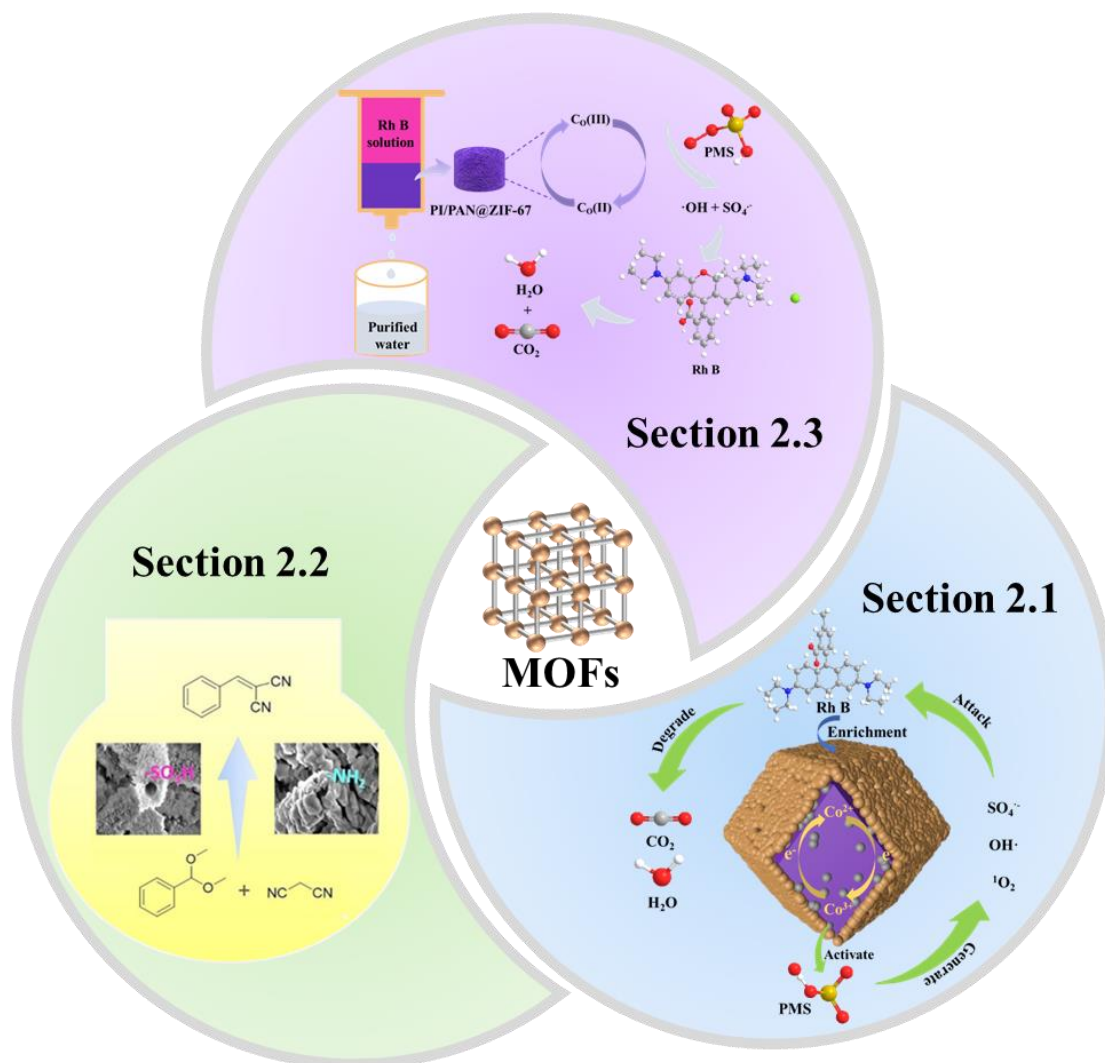
Figure 2-1. Summary of research work carried out regarding preparation and applications of macroscopic MOF materials. (Section 2.1) Synthesis of 0D macroscopic MOF material: used as a catalyst to activate PMS to degrade organic pollutants efficiently. (Section 2.2) Preparation of 1D/2D MOF fiber membranes for application in one-pot cascade reactions. (Section 2.3) Preparation of 3D MOF sponge and its application in activating PMS to degrade Rh B, a model organic pollutant.

Overview

In the first section (**Section 2.1**), a 0D magnetic core-shell HOF-on-MOF (HOF-on-Fe$_3$O$_4$/ZIF-67) composite macroscopic catalyst through the solvothermal method is prepared. The effectiveness of HOF-on-Fe$_3$O$_4$/ZIF-67 in activating PMS for the in situ generation of active species for the degradation of organic pollutants is studied by taking Rhodamine B (Rh B) as the model dye. Magnetic Fe$_3$O$_4$ can promote electron transfer between cobalt ions in ZIF, accelerating the degradation efficiency. Additionally, the catalyst could be easily and conveniently recycled using magnetic separation after the reaction. The HOF shell concentrates organic pollutants on the catalyst surface, significantly shortening the reaction path. It also effectively reduces cobalt ion leaching during the reaction, thereby increasing the stability of the catalyst.

In **Section 2.2**, the preparation and characterization of 1D/2D self-standing acid- and base- functionalized MOF membranes are detailed. The MOF membranes were prepared by growing the MOF on a template of electrospun 2D polymer membranes. Following the removal of the template polymer, self-standing, highly stable MOF membranes with hollow fibers were obtained. After use, the membranes could be easily removed and reused for cycles, maintaining their efficiency for at least 15 catalytic cycles. These membranes were used in a tea bag style for one-pot acid-base catalyzed cascade reactions. After use, the membranes could be easily removed and reused for multiple cycles, maintaining their efficiency for at least 15 catalytic cycles.

Section 2.3 focuses on the preparation and use of 3D MOF sponges. A stable, hierarchical porous zeolite imidazolate framework (ZIF-67) 3D sponge was successfully prepared by in situ growth of MOF on an electrospun short fiber network. This sponge effectively activates PMS, achieving 100% degradation efficiency of the model organic dye Rh B. The sponge's unique graded porous structure facilitates excellent water flux. Its utility as a filter for the continuous degradation of organic dyes was demonstrated by assembling a simple filtration device. In the following section, a detailed account of each study is presented.

2.1 In-situ constructed magnetic core-shell (hydrogen-bonded organic framework-on-metal-organic framework) structure: an efficient catalyst for peroxymonosulfate activation
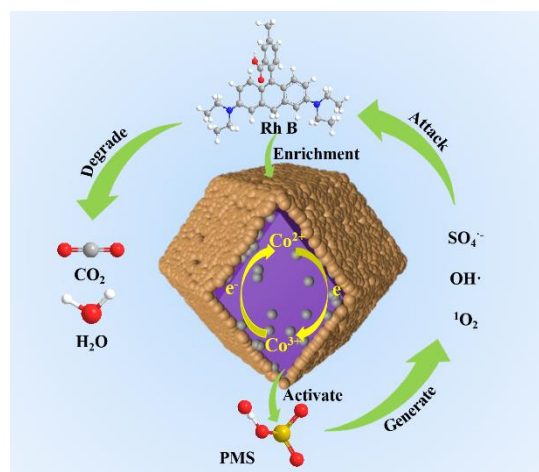
Yingying Du, Chenhui Ding, Chao Deng, Susanta Banerjee, Seema Agarwal. In-situ constructed magnetic core-shell (hydrogen-bonded organic framework-on-metal-organic framework) structure: an efficient catalyst for peroxymonosulfate activation. (Manuscript ready for submission)

Specific contributions by authors:

The idea for this project was co-designed by Prof. Seema Agarwal and me. I carried out the main experimental work, including the synthesis and characterization of Fe_3O_4 nanoparticles, ZIF-67, and the HOF-on-Fe_3O_4/ZIF-67 composite, utilizing characterization techniques such as FT-IR and electrochemical tests. I also conducted all the dye degradation experiments. Chenhui Ding performed SEM imaging and X-ray diffraction measurements on the samples, while Chao Deng handled the EPR and VSM tests. I wrote the manuscript and prepared all the figures, with Prof. Seema Agarwal supervising the project and supporting the manuscript writing. Prof. Susanta Banerjee contributed to discussions, and reviewed, and corrected the manuscript. The final manuscript was completed with the collaboration of all co-authors.

The concept of this work addresses the limitation of traditional MOF core-shell structures used as catalysts, where the shell primarily serves a protective role, and restricts the availability of catalytic active sites. The cobalt-based zeolite imidazole organic framework (ZIF-67) is frequently used as a catalyst for activating PMS to degrade organic pollutants. However, its practical application is often hindered by its nanoparticle form and the leaching of cobalt ions during use. In this work, ZIF-67 was used as the core, combined with magnetic Fe_3O_4, and a crystalline porous HOF material was selected as the shell. This design minimizes mass transfer restrictions and protects the active sites. The magnetic core-shell HOF-on-MOF (HOF-on-Fe_3O_4/ZIF-67, referred to as HFZ) catalyst was prepared by a simple solvothermal method. The specific preparation process is illustrated in **Figure 2-2a**. Initially, Fe_3O_4 nanoparticles were introduced into the precursor solution of ZIF-67 to achieve in situ growth of Fe_3O_4/ZIF-67 particles. These particles were then dispersed in an acetone solution, followed by the addition of a dimethylformamide (DMF) solution containing the HOF precursor. The mixture was stirred overnight, and the final HFZ particles were collected using magnets.
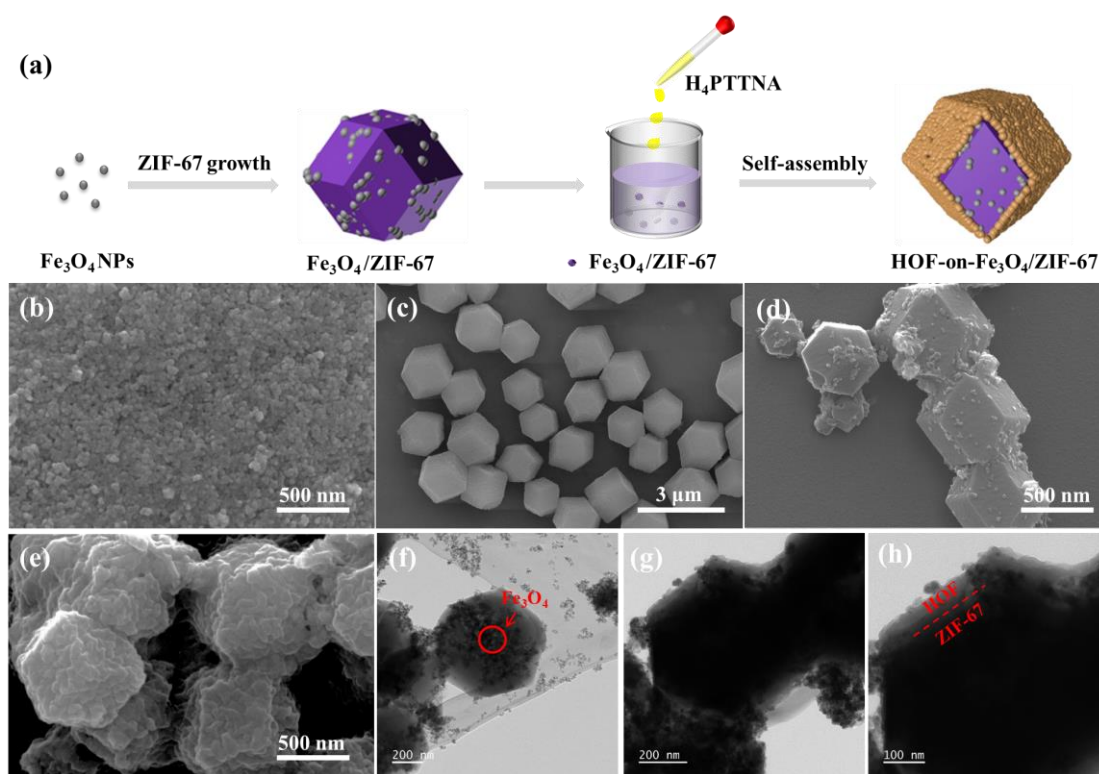
Figure 2-2. (a) Synthetic scheme for the preparation of HFZ. The SEM images of (b)

Fe_3O_4 nanoparticles, (c) ZIF-67, (d) Fe_3O_4/ZIF-67, (e) HFZ. The TEM images of f) Fe_3O_4/ZIF-67, g) and h) HFZ.

The morphology of the samples was characterized by scanning electron microscopy (SEM) (**Figure 2-2b to 2e**). The SEM images of HFZ clearly show a HOF coating on the surface of the particles, while the rhombohedral shape of ZIF-67 is preserved. Transmission electron microscopy (TEM) of HFZ reveals a darker core, representing Fe_3O_4/ZIF-67, surrounded by a lighter HOF coating (**Figure 2-2g**). The amplified TEM image (**Figure 2-2h**) shows a rough HOF shell around the core, with a thickness of about 44 nanometers (nm).
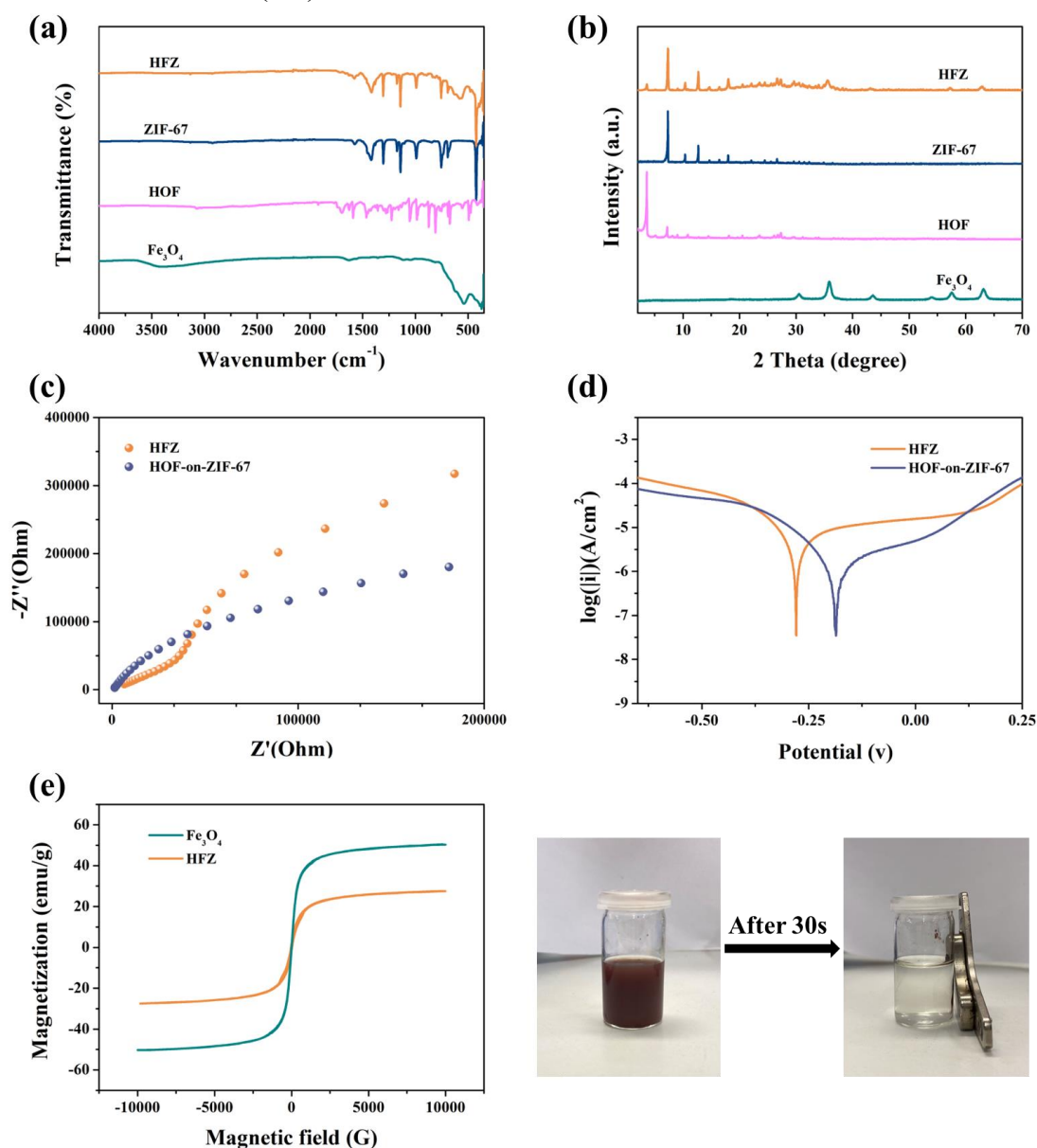
Figure 2-3. (a) The FT-IR spectra of Fe_3O_4, HOF, ZIF-67 and HFZ. (b) The XRD

diffraction patterns of Fe_3O_4, HOF, ZIF-67, and HFZ. (c) Electrochemical impedance spectroscopic (EIS) analysis and (d) Tafel polarization curves of HFZ and HOF-on-ZIF-67. (e) Magnetic hysteresis loops of Fe_3O_4 and HFZ. Optical picture showing magnetic separation of HFZ using an external magnet.

X-ray diffraction (XRD) and fourier transform infrared spectroscopy (FT-IR) confirmed the successful preparation of HFZ, showing that the addition of Fe_3O_4 and HOF did not significantly alter the crystal structure of ZIF-67 (**Figure 2-3a, 3b**). Electrochemical impedance spectroscopy (EIS) revealed that the Nyquist plot of HFZ has a smaller semicircle compared to HOF-on-ZIF-67, indicating lower charge transfer resistance (**Figure 2-3c**). This might be due to the acceleration of charge transfer facilitated by the addition of Fe_3O_4. This enhancement in electron transfer is further supported by Tafel polarization curves, where the free corrosion potentials of HFZ and HOF-on-ZIF-67 are -0.27V and -0.18V, respectively (**Figure 2-3d**), suggesting a faster electron transfer rate in HFZ. These results demonstrate that the inclusion of Fe_3O_4 significantly improves HFZ's electron transport capability, aiding in the rapid and effective degradation of organic pollutants. Additionally, vibrating sample magnetometer (VSM) tests confirmed that HFZ is ferromagnetic, enabling easy separation and recycling of the catalyst using external magnets (**Figure 2-3e**).
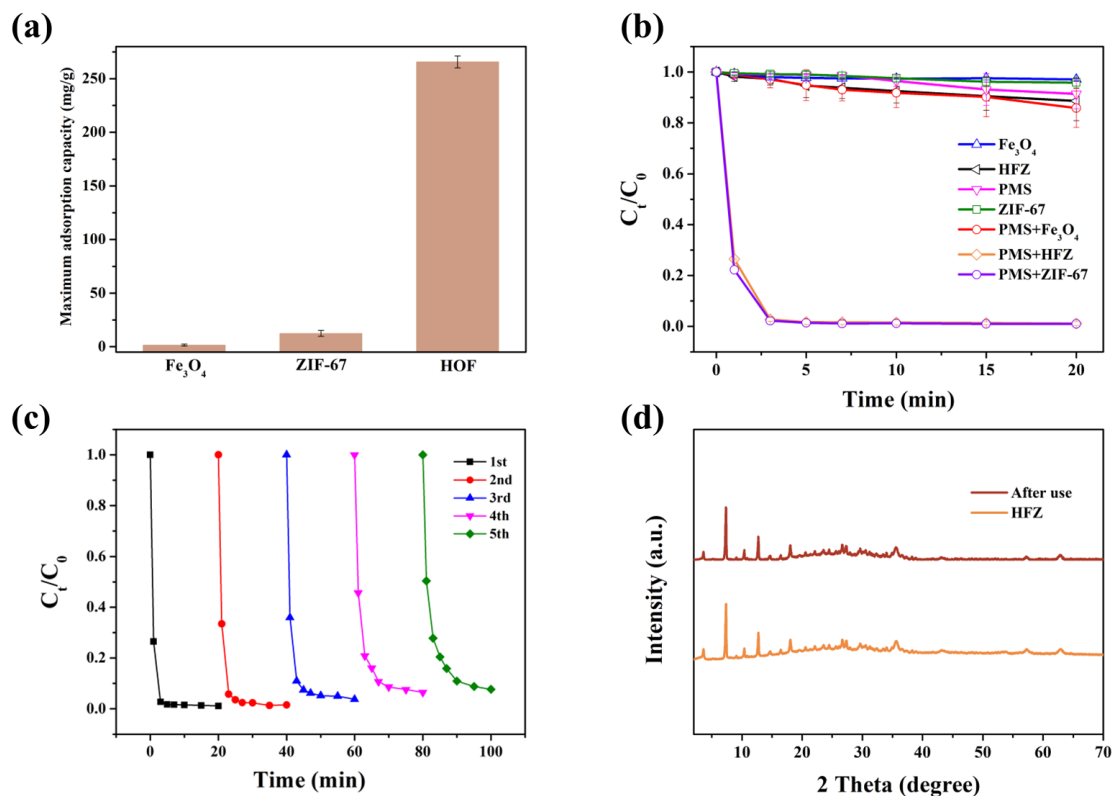
Figure 2-4. (a) The maximum adsorption capacity of Rh B by Fe_3O_4, ZIF-67, and HOF. (b) The removal of Rh B using different systems, reaction condition: Rh B; 50 mg L^{-1}, 100 mL, 1.5 mM PMS, r.t., pH=7. (c) Reusability of HFZ activated PMS for degradation of Rh B. (d) The XRD patterns of HFZ: fresh and after use.

Using Rh B as a model, the catalytic potential of HFZ for activating PMS to degrade organic pollutants was investigated. Adsorption experiments with each component of the catalyst showed that the HOF shell has a notable adsorption effect on Rh B (**Figure 2-4a**), effectively concentrating the dye on the surface of the ZIF-67 core, which likely accelerates its degradation. As shown in **Figure 2-4b,** the removal rate of Rh B by HFZ and PMS was 72.4% within 1 min, 97.5% after 3 min, and nearly 100% within 10 min. Even after 5 cycles, the removal rate of remained high at 93.6% (**Figure 2-4c**). Importantly, the XRD patterns indicates that the crystal structure of HFZ remains largely unchanged after repeated use (**Figure 2-4d**), demonstrating its high recyclability and stability. Additionally, the HOF shell effectively reduces the I cobalt ion leaching during use, with inductively coupled plasma-optical emission spectrometry (ICP-OES)

detecting only 0.14 mg L^{-1} of cobalt ion leaching after 5 cycles.

In conclusion, this work involved the design and experimental execution of a magnetic core-shell MOF catalyst (HOF-on-Fe$_3$O$_4$/ZIF-67) for activating PMS to degrade organic pollutants, such as organic dyes, in wastewater. The catalyst combines ZIF-67 with magnetic Fe$_3$O$_4$ as the core to enhance electron transfer, and HOF as a shell that can concentrate organic contaminants on the surface of the catalyst, greatly shortening the reaction path and achieving rapid organic dye degradation with high efficiency and recyclability (100% Rh B degradation within 10 min). Under the protection of the HOF shell, the leaching concentration of cobalt ions was 0.14 mg L^{-1} after 5 cycles. This research strategy offers a novel approach for preparing core-shell composite MOF materials, with potential applications beyond pollutant degradation. The work demonstrated the effectiveness and sustainability of this approach for organic dye degradation.

2.2 Template-assisted Preparation of Self-standing 2D-MOF Membranes for Application in Cascade Reactions
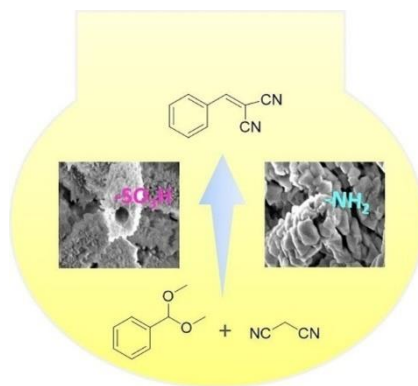
Yingying Du, Chenhui Ding, Jana Timm, Roland Marschall, Seema Agarwal. Template-assisted Preparation of Self-standing 2D-MOF Membranes for Application in Cascade Reactions. ChemCatChem, **2022**, 14(22), e202201040.

Specific contributions by authors:

In this publication, I synthesized MOF powders, prepared MOF catalyst membranes, characterized samples (FT-IR), and carried out all acid-base catalytic reactions. Chenhui Ding conducted SEM measurements and XRD testing on the samples, as well as discussed the results. He helped in problem-solving during MOF membrane preparation. Dr. Jana Timm and Prof. Roland Marschall were responsible for BET measurements and analysis of BET data. Prof. Seema Agarwal designed, guided, and supervised the project. I organized all the data and wrote the manuscript, which was then reviewed and finalized by all authors.

In this work, a template-assisted procedure is established for the preparation of two distinct functional self-standing 2D MOF membranes: UiO-66-SO$_3$H and UiO-66-NH$_2$. These MOFs were synthesized are prepared from zirconium tetrachloride (ZrCl$_4$) with 2-sulfobenzenedicarboxylic acid monosodium salt (BDC-SO$_3$Na) and 2-amino terephthalic acid (BDC-NH$_2$), respectively. For making them in the form of a 2D membrane, a template-assisted procedure is used that is divided into three steps (**Figure**

2-5). First, the template polymer polyacrylonitrile (PAN) was electrospun with $ZrCl_4$. Next, the resulting electrospun membranes were separately immersed in BDC-SO$_3$Na and BDC-NH$_2$ solutions containing acetic acid as a catalyst and reacted at 120 °C to obtain PAN/MOF composite membranes. Finally, the template polymer PAN was removed through Soxhlet extraction, yielding self-standing MOF membranes: UiO-66-SO$_3$H with a thickness of 240 ± 12 micrometers (µm) and UiO-66-NH$_2$ with a thickness of 265 ± 10 µm, respectively.

Figure 2-5. The template-assisted procedure to fabricate the self-standing 2D MOF membranes: UiO-66-SO$_3$H and UiO-66-NH$_2$ (top) and the reaction scheme to prepare corresponding MOFs (bottom).

SEM characterization, shown in **Figure 2-6**, revealed that the MOFs extensively grew on and fully enveloped the PAN fibers. Once the PAN template was removed, the MOF fibers maintained the randomly laid structure of the original template fibers but showed a hollow structure.
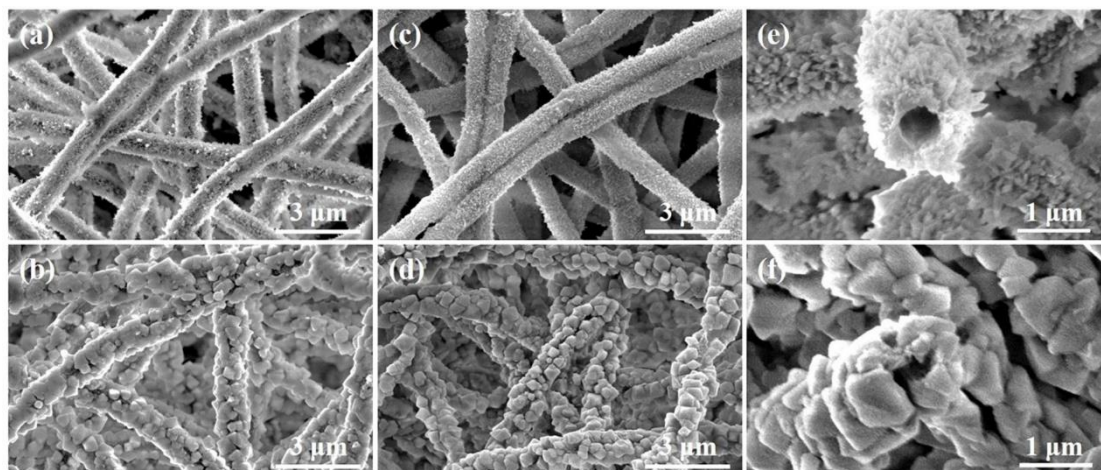
Figure 2-6. SEM morphology of (a) PAN/UiO-66-SO$_3$H, (b) PAN/UiO-66-NH$_2$, (c) UiO-66-SO$_3$H, (d) UiO-66-NH$_2$, Cross-sectional SEM morphology of (e) UiO-66-SO$_3$H, (f) UiO-66-NH$_2$ membranes.

Additionally, combined with XRD patterns and FT-IR analysis methods, the successful preparation of desired MOF structures was confirmed (**Figure 2-7a, 7b**). The N$_2$ physical adsorption isotherm provides the pore size distribution and specific surface area of the powder and self-standing MOF membranes (as shown in **Figure 2-7c,7d**). Using BET (Brunauer Emmet Teller) model combined with Roquerol correction of microporous materials, the specific surface area of the membranes (UiO-66-NH$_2$: 330 m^2 g^{-1}, UiO-66-SO$_3$H: 84 m^2 g^{-1}) was calculated to be significantly lower than that of the powder samples (UiO-66-NH$_2$:1051 m^2 g^{-1}, UiO-66-SO$_3$H: 539 m^2 g^{-1}). This reduction in surface area can be explained by a partial change in the crystal structure or surface tension of the UiO-66 material crystals, which can already be observed by the widening reflected in the XRD patterns.
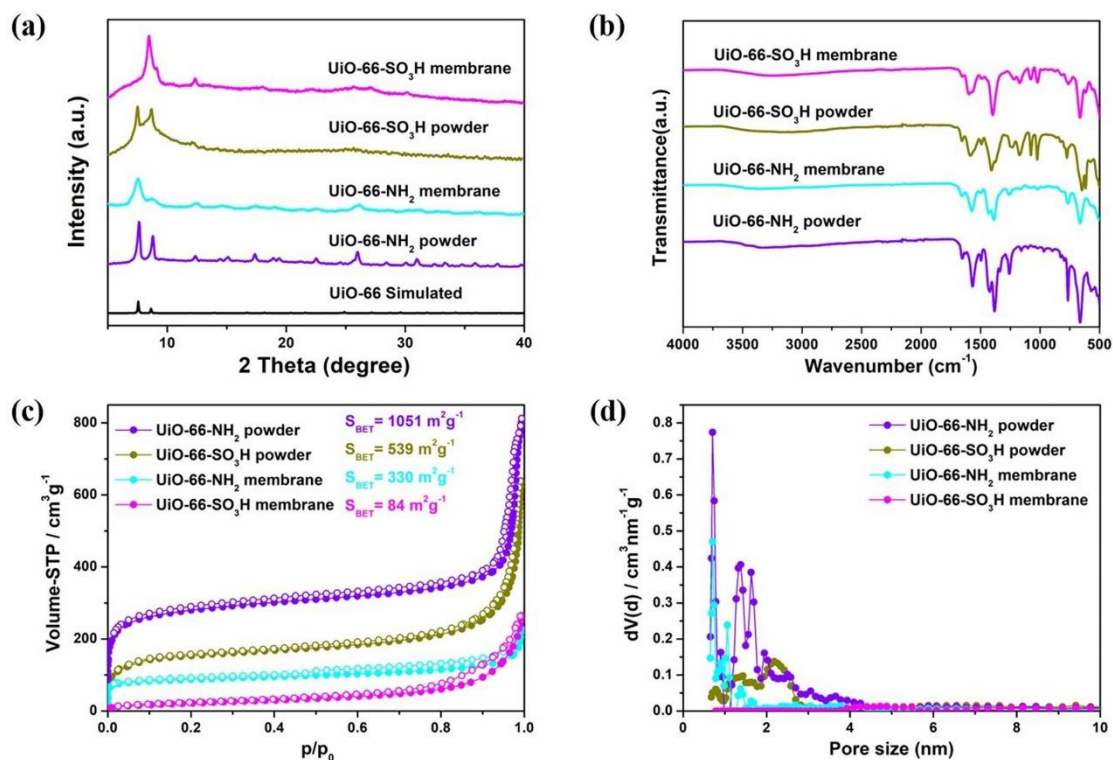
Figure 2-7. (a) XRD patterns of UiO-66 simulated, UiO-66-SO₃H powder, UiO-66-SO₃H membrane, UiO-66-NH₂ powder, and UiO-66-NH₂ membrane. (b) FT-IR spectra of UiO-66-SO₃H powder, UiO-66-SO₃H membrane, UiO-66-NH₂ powder, and UiO-66-NH₂ membrane. (c) N₂ physisorption isotherms of UiO-66-SO₃H powder, UiO-66-SO₃H membrane, UiO-66-NH₂ powder, and UiO-66-NH₂ membrane. (d) Pore size distribution and cumulative pore volume of UiO-66-SO₃H powder, UiO-66-SO₃H membrane, UiO-66-NH₂ powder, and UiO-66-NH₂ membrane.

The fiber morphology, acid-base functionalities, and modularity of the membrane enable its use in a two-step cascade reaction within a single pot something typically challenging due to the mutual inactivation of acid and base catalysts in a Wolf-Lamb type scenario. In this one-pot, two-step reaction the UiO-66-SO₃H membrane catalyzes the conversion of benzaldehyde dimethylacetal to benzaldehyde, while the UiO-66-NH₂ membrane simultaneously catalyzes the Knoevenagel condensation of benzaldehyde with different active methylene compounds such as malonitrile and ethyl cyanoacetate and diethyl malonate (**Figure 2-8a**). The system demonstrated excellent performance, particularly with malonitrile as raw material in the second step, achieving

a product yield of 99.9%. Moreover, the self-standing membranes form of the catalyst allows for easy recovery and reuse with no was no significant loss in catalytic efficiency after 15 cycles (**Figure 2-8b**).
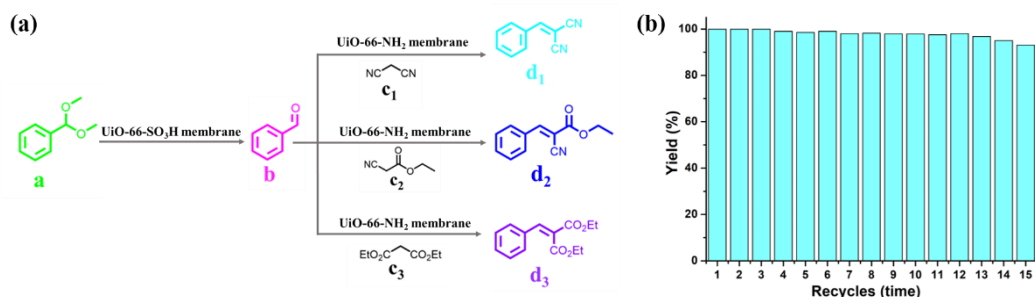
Figure 2-8. (a) One-pot cascade reactions catalyzed by acid- and base- functionalized 2D self-standing MOF membranes. (b) Recycling performance.

In summary, this work establishes a template-assisted fabrication procedure for self-standing 2D MOF membranes. The membrane showed excellent catalytic activity, achieving up to 99.9% yield in a one-pot cascade reaction (Wolf-Lamb type), and maintained its efficiency even after 15 cycles. This research represents a significant step toward the development and use of macro-sized MOF membranes as sustainable catalysts.

2.3 Sustainable Hierarchically Porous Reusable Metal-Organic Framework Sponge as a Heterogeneous Catalyst and Catalytic Filter for Degradation of Organic Dyes
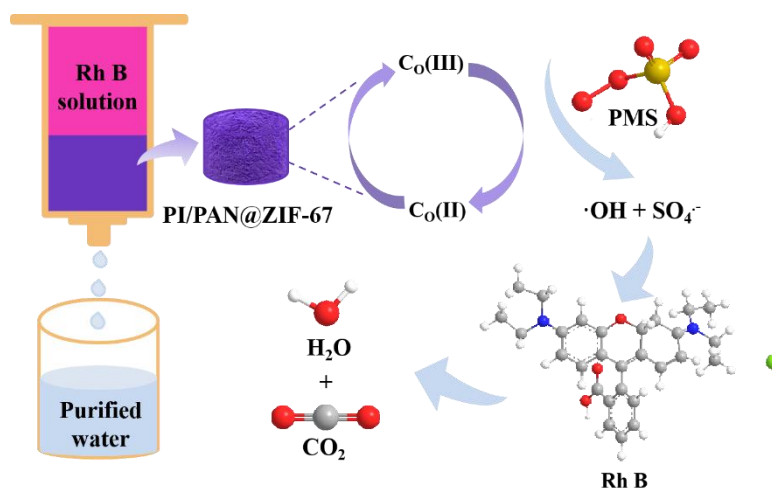
Yingying Du, Chenhui Ding, Seema Agarwal. Sustainable Hierarchically Porous Reusable Metal-Organic Framework Sponge as a Heterogeneous Catalyst and Catalytic Filter for Degradation of Organic Dyes. Advanced Energy and Sustainability Research, **2023**, 5(4), 2300218.

Specific contributions by authors:

The Concepts and resources were contributed by Prof. Seema Agarwal. Chenhui Ding and I designed the experiments in consultation with Prof. Seema Agarwal. I prepared and characterized the ZIF-67 powder, PI/PAN sponge, and PI/PAN@ZIF-67 sponge and conducted FT-IR, and compression experiments, as well as all dye degradation experiments. Chenhui Ding conducted SEM measurements and XRD testing on the samples. I analyzed the experimental data and wrote the manuscript. Prof. Seema Agarwal discussed the experimental scheme and revised the original manuscript. The final manuscript was completed with the help of all the co-authors.

This study introduces a simple and scalable approach to prepare stable, hierarchically porous zeolitic imidazolate framework (ZIF-67) 3D sponges by growing them on

template electrospun short fiber networks. The process begins with the mechanical cutting of polymer non-woven fibers prepared by electrospinning, into short fibers. These fibers are then dispersed in water/organic solvents to form a fiber suspension, which is freeze-dring to create a 3D porous sponge with open pores. These electrospun short fiber sponges serve as a matrix for creating a 3D MOF macrostructure.

A key challenge in this work was achieving a mechanically stable polymer matrix sponge with strong adhesion between the polymer matrix and the MOF, ensuring the growth of a defect-free, continuous MOF layer on the sponge template. After extensive experimentation, a reproducible procedure was established in which a dispersion of short polymer fibers, a polymer binder, and metal salt precursors for the MOF was freeze-dried to create a stable template sponge on which the MOF could grow. The specific preparation process is shown in **Figure 2-9**. Polyimide (PI) short fibers (length $L = 77 \pm 33$ μm), polymer binder (PAN), and $Co(NO_3)_2 \cdot 6H_2O$ were dispersed in dimethyl sulfoxide (DMSO) and freeze-drying to form a honeycomb structured $PI/PAN/Co^{2+}$ sponge. The $PI/PAN/Co^{2+}$ sponge then was immersed into the ZIF-67 precursor solution ($Co(NO_3)_2 \cdot 6H_2O$ and 2-methylimidazole (2-MeIm)), and ZIF-67 grows in situ on the surface of the template polymer fibers. The loading amount of ZIF-67 was determined based on the mass change of the $PI/PAN/Co^{2+}$ sponge after ZIF-67 growth. A loading capacity of up to 72 wt% was achieved. Unfortunately, all efforts to create a self-standing, mechanically stable 3D MOF sponge by removing the fiber templates were unsuccessful.
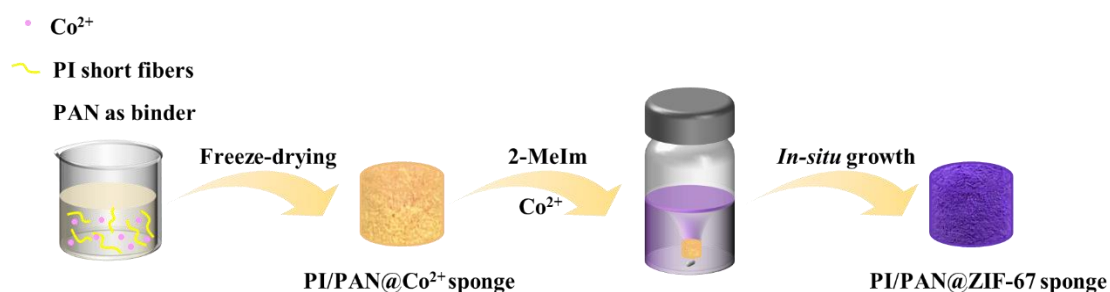
Figure 2-9. Preparation of the PI/PAN@ZIF-67 sponge: Co^{2+} comes from $Co(NO_3)_2 \cdot 6H_2O$; 2-MeIm is 2-methylimidazole.

SEM analysis of the PI/PAN@ZIF-67 sponge (**Figure 2-10b, 10c**) reveals that the surface of the PI short fibers is completely covered by a dense layer of ZIF-67 particles. The in situ growth of ZIF-67 on the PI short fibers ensures that the active sites within the ZIF-67 structure are well preserved. Cyclic compression tests of the PI/PAN@ZIF-67 sponge indicate that it has good mechanical properties, with a compressive strength of 28.1 kPa under 50% strain and a height reduction of only 9.9% after 300 compression cycles (**Figure 2-10d**).
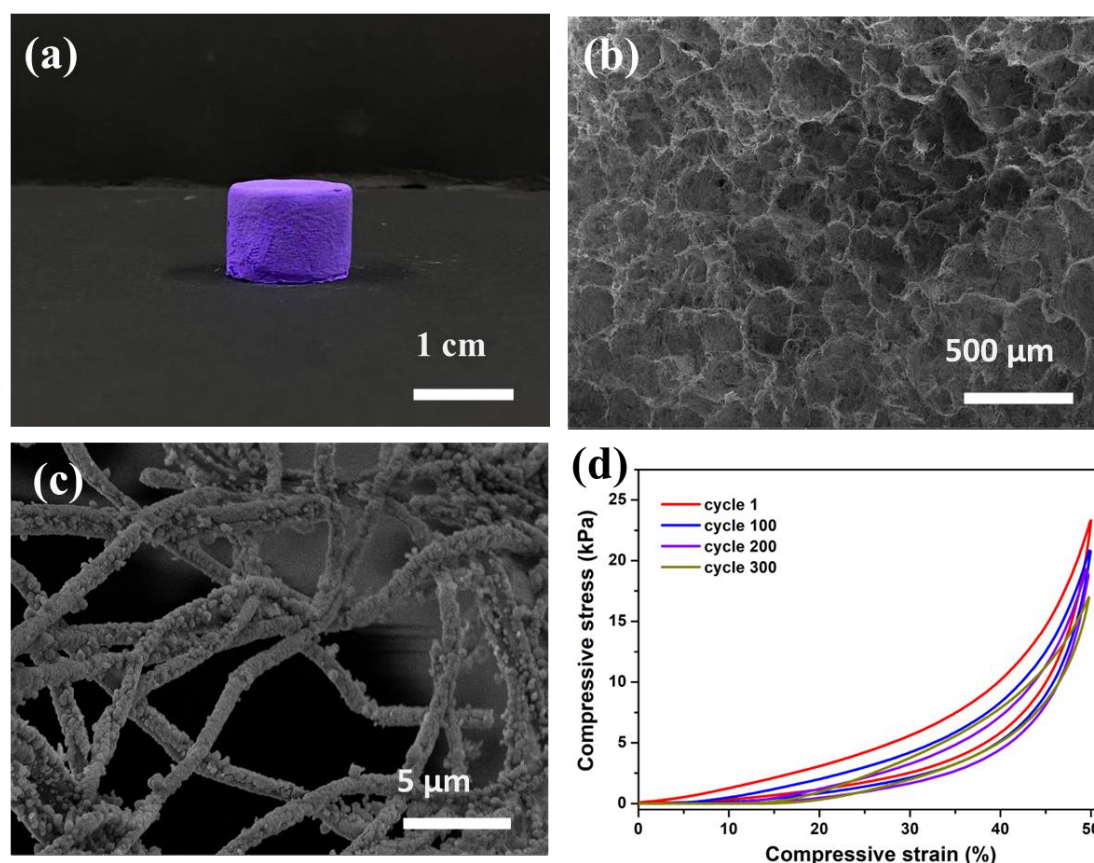
Figure 2-10. (a) The photo of PI/PAN@ZIF-67 sponge. (b, c) SEM images of PI/PAN@ZIF-67 sponge. (d) Cyclic compressive stress-strain curves at 50% strain for PI/PAN@ZIF-67 sponge.

The nanopores of the ZIF-67, the micropores between the cross-linked PI short fibers, and the regular honeycomb macropores of the sponge form a 3D structure with multilevel and hierarchical macro-micropores. It can be used as a catalyst to efficiently activate PMS to degrade organic pollutants (Rh B, as a model pollutant). **Figure 2-11a** shows the degradation of Rh B using different catalytic systems. For the PI/PAN@ZIF-

67 sponge/PMS system, the degradation rate of Rh B dye was as high as 97.4% within 5 min, and Rh B was almost completely degraded within 30 min. Furthermore, the PI/PAN@ZIF-67 sponge can be easily separated washed, and reused to degrade dyes. After five cycles of use, the degradation efficiency of Rh B remained basically unchanged (**Figure 2-11b**). Additionally, we constructed a simple filtration device to use the sponges for continuous treatment of dye wastewater solutions (**Figure 2-11c**). The Rh B solution quickly passed through the PI/PAN@ZIF-67 sponge under the force of gravity, and the sponge's catalytic action resulted in a clear solution after filtration. Even after 6 h of continuous processing, the filtration device maintained a high Rh B removal rate of 95% (**Figure 2-11d**).
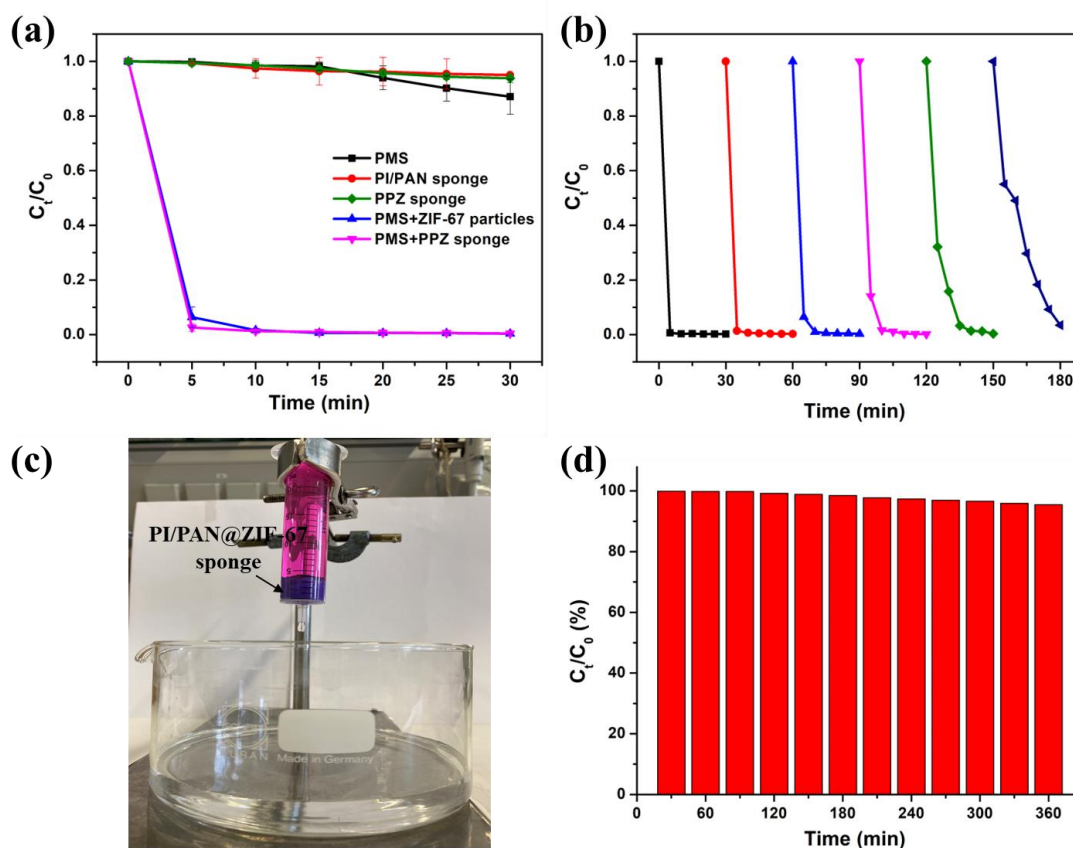
Figure 2-11. (a) Plots of C_t/C_0 versus time for studying the degradation of Rh B under different conditions. (b) Reusability test of PI/PAN@ZIF-67 sponge. (c) Photograph of the assembly showing the degradation of Rh B through the filtration process. The PI/PAN@ZIF-67 sponge was installed in the syringe as a catalytic filter to degrade Rh B. (d) Continuous degradation experiment of Rh B using PI/PAN@ZIF-67 sponge as a

filter.

In summary, we prepared PI/PAN@ZIF-67 sponge with high ZIF-67 loading (up to 72 wt%) and multi-layered macro-porous honeycomb structure by in situ growth of ZIF-67 on the surface of PI short fibers. The three-dimensional porous framework and high ZIF-67 loading endow the sponge with excellent mechanical properties and compression resistance, and serve as a PMS-activated catalyst, showing excellent degradation properties for organic dyes, and can be reused many times. This research strategy provides a scalable new method for preparing 3D MOF macroscopic materials.

3. Outlook

Metal-organic frameworks (MOFs) have been widely studied and rapidly developed since their initial discovery due to their highly ordered porosity, high specific surface area, and adjustable structure. Tens of thousands of MOF structures have been designed and synthesized, and are widely used in various fields such as catalysis, gas adsorption/separation, sensors, drug delivery, magnetic materials, and optical devices. Unfortunately, MOF nanoparticle forms are prone to loss and clogging of pipelines in practical applications, leading to secondary pollution. Additionally, their difficulty in dissolving and processing greatly hinders their development potential in practical applications. Therefore, in this work, zero-dimensional (0D), one/two-dimensional (1D/2D), and three-dimensional (3D) macroscopic MOF materials were prepared using a simple solvothermal method and electrospinning process combined with a template-assisted process and freeze-drying, respectively, and the prepared 1D/2D macroscopic MOF were further studied as Wolf-Lamb type catalysts in the form of membranes to catalyze cascade organic reactions. And the application of 0D and 3D macroscopic MOF in activated peroxymonosulfate (PMS) degradation of organic pollutants. The overall material form of MOFs makes it simple and easy to recover, separate, and recycle in practical applications. In the preparation process of macroscopic MOF materials, MOFs is effectively combined with various functional materials to give the material new physical and chemical properties, making it suitable for a wider range of applications. Therefore, it is very important to explore a new general method for constructing specific functional macroscopic MOF materials with low energy consumption, low solvent, and rapid scale-up synthesis technology. Furthermore, understanding the relationship between the structure and properties of macroscopic MOF materials and exploring the interaction at the interface should also be the focus of future research, which is conducive to the design and manufacture of new MOF-based integral functional materials for various applications. In short, more versatile and simpler manufacturing strategies should be developed in the next work to continuously promote the development of macroscopic MOF materials in practical applications.

84

4. Publications

4.1 In-situ constructed magnetic core-shell (hydrogen-bonded organic framework-on-metal-organic framework) structure: an efficient catalyst for peroxymonosulfate activation

Yingying Du, Chenhui Ding, Chao Deng, Susanta Banerjee, Seema Agarwal. In-situ constructed magnetic core-shell (hydrogen-bonded organic framework-on-metal-organic framework) structure: an efficient catalyst for peroxymonosulfate activation. Manuscript ready for submission.

In-situ constructed magnetic core-shell (hydrogen-bonded organic framework-on-metal-organic framework) structure: an efficient catalyst for peroxymonosulfate activation

Yingying Du, Chenhui Ding, Chao Deng, Susanta Banerjee, and Seema Agarwal*

Y. Du, C. Ding, C. Deng, Prof. S. Agarwal

Advanced Sustainable Polymers, Macromolecular Chemistry 2, and Bavarian Polymer Institute

University of Bayreuth

Universitätsstrasse 30, 95440 Bayreuth, Germany

E-mail: agarwal@uni-bayreuth.de

Prof. S. Banerjee

Materials Science Centre

Indian Institute of Technology Kharagpur

Kharagpur-721302, India

Abstract

Zeolite imidazole-based framework (ZIF-67), a notable class of metal-organic frameworks (MOFs), shows promise in activating peroxymonosulfate (PMS) for pollutant degradation due to its uniformly distributed cobalt ions. However, its nanoparticle form and the leaching of cobalt ions during use result in complex recyclability and the risk of secondary pollution. In this study, a magnetic core-shell hydrogen-bonded organic framework (HOF) on the MOF (HOF-on-Fe_3O_4/ZIF-67) was successfully prepared. The porous HOF shell not only protects the active sites and mitigates cobalt ion leaching but also reduces mass transfer limitations, ensuring sustained catalytic performance. The magnetic Fe_3O_4 core enhances electron transfer between cobalt ions, boosts catalytic efficiency, and facilitates easy separation and recycling. This present core-shell structure effectively activates PMS, achieving 100% removal of Rhodamine B, a model waste water dye within 10 minutes. Furthermore, under the protection of the HOF shell, cobalt ion leaching is minimized to a negligible value (0.14 mg L^{-1}) after five cycles of use. This research offers new insights into the development of core-shell composite materials with improved performance and recyclability.

1

1. Introduction

The sulfate radical-advanced oxidation process (SR-AOP) can effectively decompose highly toxic and refractory organic contaminants into low-toxicity small molecules, inorganic salts, water, and carbon dioxide, positioning it as one of the most promising technologies for wastewater treatment.[1] Compared to hydroxyl radicals ($\cdot OH$), sulfate radicals ($SO_4^{\cdot-}$) exhibit a higher redox potential (2.5 ~ 3.1V), a wider pH range (3 - 9), longer stability, and superior reaction selectivity.[2] Sulfate radicals are typically generated through the activation of persulfate (PS, $S_2O_8^{2-}$) or peroxymonosulfate (PMS, HSO_5^-).[3] Due to its asymmetric molecular structure, PMS is more easily activated than PS and is environmentally friendly, making it widely used in industry.[4] Transition metal ions (Cu^{2+}, Ni^{2+}, Fe^{2+}, Co^{2+}, and Mn^{2+}), metal oxides (Co_3O_4, Fe_3O_4, Mn_3O_4) ultrasound, ultraviolet irradiation, and electrochemistry methods are employed to activate PMS.[5] Among them, cobalt-based catalysts (especially Co^{2+}) are thermodynamically more favorable for combining with HSO_5^- having lower Gibbs free energy values, and are considered the most ideal PMS activators.[6]

The zeolite-like imidazole framework (ZIF-67), a significant subclass of metal-organic frameworks (MOFs), is constructed using cobalt as the metal source and 2-methylimidazole (2-MeIM) as the organic ligand. This framework features an abundance of divalent cobalt species uniformly dispersed throughout, high porosity, and excellent chemical stability, attributes that have attracted considerable scholarly attention.[7] Studies have demonstrated that ZIF-based catalysts can effectively activate PMS to degrade organic pollutants, highlighting their potential as promising cobalt-based catalysts.[8] However, the practical application of ZIF-67 in PMS activation is impeded by its nanoparticle form, which complicates recyclability. Additionally, the leaching of cobalt ions during use raises concerns about secondary pollution and poses risks to both the ecosystem and human health. [9] Therefore, it is imperative to design catalysts that enhance both service life and stability to address these issues.

To overcome these challenges, the development of core-shell composite materials has proven to be highly effective. For instance, Wu et al. created a $Fe_3O_4@Zn/Co$-ZIFs core-shell structure and achieved 100% removal of carbamazepine (5 mg L^{-1}) within 30 minutes.[10] Similarly, Wan et al. synthesized a core-hetero shell magnetic composite material, ZIF-67/vanadium titanium magnetite (VTM), which effectively activated PMS and achieved a 93.3% removal rate of levofloxacin within 60 minutes.[11]

However, in traditional core-shell structures, the shell usually does not participate in the reaction and primarily serves a protective role. This limits the full potential of the core-shell structure. Furthermore, the shell coating can hinder the exposure of active sites, leading to

2

reduced catalytic performance. Consequently, selecting appropriate shell materials is crucial to enhance both the protective function and the catalytic activity.

Hydrogen-bonded organic frameworks (HOFs) have emerged as a promising class of crystalline materials, attracting widespread attention from scholars due to their well-defined structures and multifunctional properties.[12] Notably, HOF-102 demonstrates excellent stability and chemical resistance, with its porosity facilitating the enrichment of dyes.[13] This characteristic enables dye aggregation on the catalyst surface, effectively shortening the degradation path and accelerating the breakdown of organic pollutants. Consequently, HOF is considered an excellent choice for shell materials. However, to our knowledge, there are currently no literature reports evaluating HOF-on-MOF materials in SR-AOP.

In this study, we developed a magnetic HOF-on-MOF-type core-shell catalyst (HOF-on-Fe_3O_4/ZIF-67, referred to as HFZ) using ZIF-67 as the core incorporated with magnetic Fe_3O_4. The inclusion of Fe_3O_4 enhances electron transfer between cobalt ions, thereby improving catalytic performance and facilitating the quick and easy separation and recovery of the catalyst after use. The porous HOF shell minimizes mass transfer limitations and protects the active sites, effectively reducing the leaching of cobalt ions during use while maintaining strong catalytic performance. This unique core-shell structure makes it an ideal catalyst for PMS activation. The catalyst efficiently activated PMS, achieving 100% removal of a model dye (Rhodamine B, Rh B) within 10 minutes, and demonstrated effective degradation across a wide pH range (3 - 9) with minimal Co ion leaching (0.14 mg L^{-1} after five cycles). This research strategy not only broadens the application of HOF materials in water treatment but also provides new insights into the preparation of core-shell composite materials for use in SR-AOP.

3

2. Results and discussion
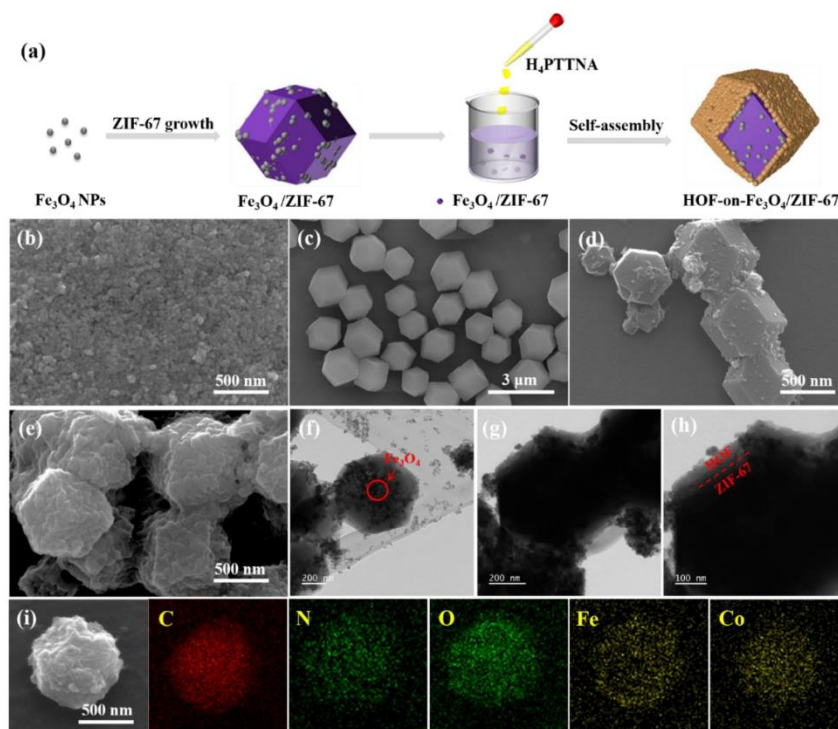
Figure 1. a) Synthetic strategy scheme for the preparation of HFZ. The SEM images of b) Fe$_3$O$_4$ nanoparticles, c) ZIF-67, d) Fe$_3$O$_4$/ZIF-67, e) HFZ. The TEM images of f) Fe$_3$O$_4$/ZIF-67, g) and h) HFZ. i) EDS elemental mapping images of HFZ.

The preparation strategy for the HFZ is illustrated in **Figure 1a**. Initially, Fe$_3$O$_4$ nanoparticles were introduced into the precursor solution of ZIF-67 to achieve in-situ growth of Fe$_3$O$_4$/ZIF-67 particles. Next, these Fe$_3$O$_4$/ZIF-67 particles were dispersed in an acetone solution, to which a dimethylformamide (DMF) solution of the HOF precursor was added dropwise and stirred overnight. The final HFZ particles were then collected using a magnetic. The morphology and particle size of the materials were characterized by scanning electron microscopy (SEM) and transmission electron microscopy (TEM). Fe$_3$O$_4$ nanoparticles maintain a consistent spherical shape with a particle size of 23.8±1.92 nm (**Figure 1b**). ZIF-67 exhibits a typical rhombohedral dodecahedron structure with a particle size of approximately 823±75 nm (**Figure 1c**).[14] The

4

average diameter of Fe_3O_4 nanoparticles and ZIF-67 were calculated with ImageJ software by randomly selecting 100 positions of particles in SEM images. HOF showed a rod-like structure (**Figure S1**). The overall morphology of the synthesized Fe_3O_4/ZIF-67 (**Figure 1d**) maintains the rhombohedral dodecahedron shape, with numerous Fe_3O_4 nanoparticles distributed on the surface and within the bulk of the ZIF-67 particles. The TEM image of Fe_3O_4/ZIF-67 (**Figure 1f**) confirms the presence of Fe_3O_4 within the ZIF-67 core. The surface of the HFZ particles is distinctly covered by the HOF coating while preserving the rhombohedral dodecahedron shape (**Figure 1e**). TEM images of HFZ (**Figure 1g**) reveal two distinct regions: a darker core, representing the Fe_3O_4/ZIF-67, surrounded by lighter regions indicating the HOF coating. The enlarged TEM image (**Figure 1h**) clearly shows an interfacial layer of rough HOF shell around the Fe_3O_4/ZIF-67 core, with a shell thickness of approximately 44 nm. Overall, the SEM and TEM images confirm the successful synthesis of the magnetic HFZ core-shell structure. Additionally, x-ray energy dispersive spectroscopy (EDS) elemental mapping of individual HFZ particles demonstrates the presence of C, N, O, Fe, and Co elements in the core-shell particles (**Figure 1i**).

The x-ray diffraction (XRD) patterns of Fe_3O_4, HOF, ZIF-67, and HFZ are shown in **Figure 2a**. In the XRD pattern of HFZ, 2 theta corresponds to the (1 0 0) crystal plane at 3.6°, which belongs to the characteristic diffraction peak of HOF.[15] 7.4°, 10.5°, 12.9°, 14.8°, 16.6° and 18.2° correspond to the (0 11), (0 0 2), (11 2), (0 2 2), (0 1 3) and (2 2 2) crystal planes, which are highly consistent with the ZIF-67 crystal.[16] And 30.5°, 35.6°, 43.6°, 57.5°, and 62.8° are attributed to (2 2 0), (3 1 1), (4 0 0), (5 1 1) and (4 4 0) crystal planes, which are highly matched with the characteristic diffraction peaks of Fe_3O_4 nanoparticles.[17] These results confirmed the successful preparation of HFZ, and the addition of Fe_3O_4 and HOF had no significant effect on the crystal structure of ZIF-67.

Fourier transform infrared spectroscopy (FT-IR) was employed for structural analysis (**Figure 2b**). The peak at 625 cm^{-1} corresponds to the Fe-O bond, and the peak at 574 cm^{-1} is associated with Fe_3O_4, aligning well with the literature.[18] The peak at 425 cm^{-1} is attributed to the stretching vibration of Co-N in the ZIF-67 crystal, while the peaks at 1418 cm^{-1} and 1580 cm^{-1} correspond to the stretching modes of the C-N bond in imidazole.[19] These characteristic peaks observed in the FT-IR spectra of HFZ confirm the successful synthesis of HFZ.

5

WILEY-VCH
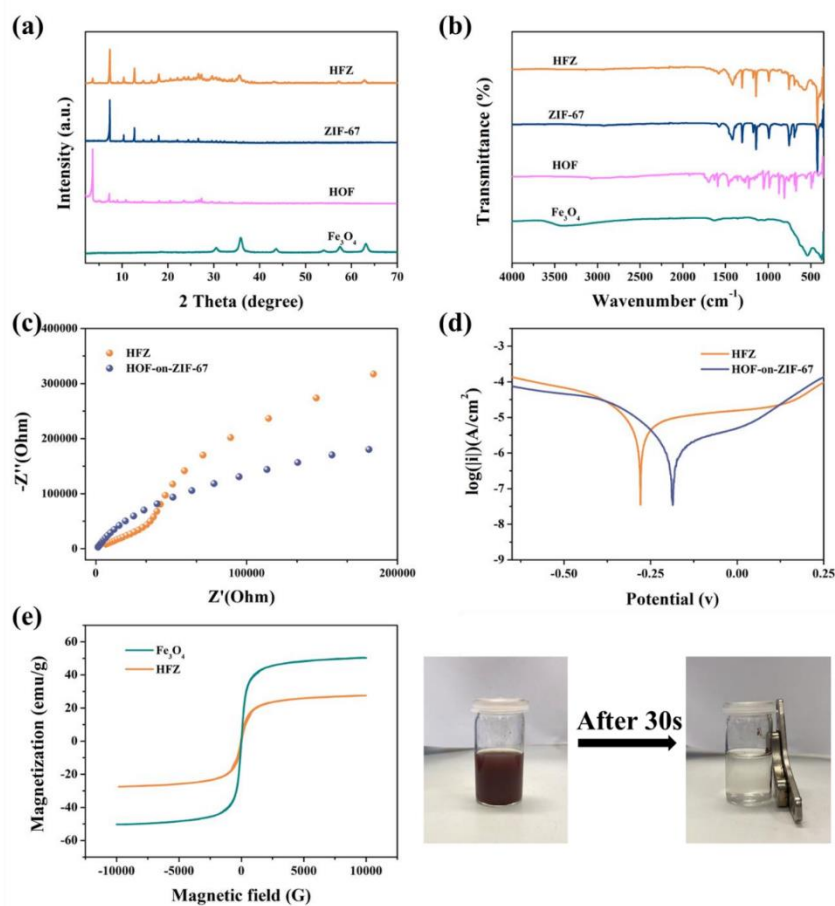
Figure 2. a) The XRD patterns of Fe_3O_4, HOF, ZIF-67, and HFZ. b) The FT-IR spectra of Fe_3O_4, HOF, ZIF-67 and HFZ. c) Electrochemical impedance spectroscopic (EIS) analysis and d) Tafel polarization curves of HFZ and HOF-on-ZIF-67. e) Magnetic hysteresis loops of Fe_3O_4 and HFZ. And HFZ has excellent magnetic separation using an external magnet (30 s).

The electrochemical impedance spectroscopic (EIS) analysis of HOF and HOF-on-ZIF-67 revealed that the Nyquist plot for HFZ shows a smaller semicircle compared to HOF-on-ZIF-67 (**Figure 2c**). This indicates that HFZ has a relatively lower charge transfer resistance, which can be attributed to the accelerated charge transfer facilitated by the inclusion of Fe_3O_4.[20] The Tafel polarization curve analysis further supports this observation (**Figure 2d**). The free

6

91

corrosion potentials for HFZ and HOF-on-ZIF-67 are -0.27 V and -0.18 V. This suggests a faster electron transfer rate for HFZ compared to HOF-on-ZIF-67. These results indicate that the addition of Fe_3O_4 significantly enhances the electron transfer ability of HFZ which would be beneficial for the rapid and effective degradation of organic pollutants.

Additionally, magnetic properties were evaluated using a vibrating sample magnetometer (VSM) (**Figure 2e**). The saturation magnetization (Ms) values for Fe_3O_4 nanoparticles and HFZ were 50.3 emu g^{-1} and 27.6 emu g^{-1}, respectively. The decrease in magnetic strength for HFZ is primarily due to the ZIF-67 and HOF coatings. Nonetheless, the strong magnetic response of HFZ allows for easy separation using an external magnet, facilitating the collection, recycling, and reuse of the catalyst.

As a refractory organic pollutant, Rhodamine B (Rh B) released into water can cause cancer in humans, pollute water and soil, and harm the ecosystem. Therefore, in our study, Rh B was chosen as a model organic contaminant to evaluate the performance of HFZ as a catalyst to activate PMS. Before the actual experiment of evaluating catalytic performance, the dye enrichment effect of the individual components of the core-shell structure was conducted (**Figure S2**). The results showed that the adsorption capacities of Fe_3O_4 nanoparticles and ZIF-67 for Rh B were low, with maximum adsorption capacities of 1.5 mg g^{-1} and 14.3 mg g^{-1}, respectively. This low adsorption is likely due to the large molecular structure of Rh B, resulting in minimal interaction with the surfaces of these materials. In contrast, HOF exhibited a high adsorption capacity for Rh B, with a maximum value of 265.3 mg g^{-1}. This high capacity can be attributed to the high porosity and porous structure of HOF.[15] These results suggest that the HOF shell in the composite material effectively enriches the dye, concentrating Rh B which might be promising for dye degradation. Next, the Rh B removal efficiencies of different systems were evaluated and the results are illustrated in **Figure 3a**. Fe_3O_4 and ZIF-67 alone exhibited negligible removal efficiencies (1.6% and 3.1%, respectively). The HFZ system, however, achieved a 12.6% reduction in Rh B within 20 minutes. This reduction is likely due to the adsorption of Rh B on the HOF shell of HFZ, as HOF alone also demonstrated significant adsorption of Rh B. The removal efficiency of Rh B with PMS alone was only 8.6%, indicating that PMS alone cannot be spontaneously activated to produce free radicals effectively. In the Fe_3O_4 and PMS system, 14.2% of Rh B was removed, suggesting that Fe_3O_4 alone has limited ability to activate PMS.

In contrast, the HFZ together with PMS removed 72.4% of Rh B within 1 minute, with the removal efficiency reaching up to 97.5% after 3 minutes of reaction and nearly complete removal within 10 minutes. This demonstrates that HFZ serves as an efficient catalyst for PMS

7

WILEY-VCH

activation, facilitating the rapid removal of Rh B. Initially, as shown in **Figure 3a**, the dye degradation efficiency of ZIF-67 activated PMS appears almost the same as that of HFZ. As the total amounts (mass) of HFZ and ZIF-67 used in the experiments were the same, the actual amount of activating ZIF-67 in HFZ is less than that in pure ZIF-67. This actually indicates that HFZ-activated PMS is more efficient, as it contains less ZIF-67 compared to pure ZIF-67. This demonstrates that introducing Fe_3O_4 can enhance electron transfer between cobalt ions and accelerate the degradation rate of organic matter. We compared the efficiency of HFZ with some literature known related systems (**Figure 3b**) and demonstrated a new, efficient dye degradation system. The values for CuS-PVP@ZIF-67, $MnFe_2O_4$/ZIF-67, $CuFe_2O_4$@ZIF-67, Fe_3O_4-PVP@ZIF-67, NF/ZIF-67, and cal-ZIF-67/Ac in **Figure 3b** were taken from literatures cited as in the reference section.[21]
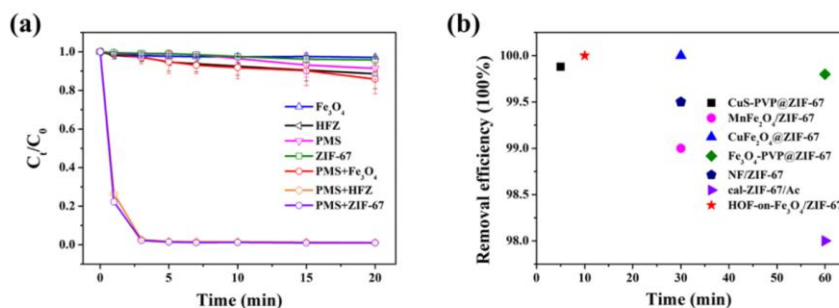
Figure 3. a) The removal of Rh B using different systems, reaction condition: Rh B; 50 mg L^{-1}, 100 mL, 1.5 mM PMS, rt., pH=7. b) Comparison of HFZ/PMS system with other reported MOF-based and/or metal oxide catalysts in Rh B removal.

To further explore the performance of HFZ, we analyzed the effects of Rh B concentration, PMS contents, HFZ dosages, and solution conditions on degradation efficiency. **Figure 4a** shows the effect of a constant amount of HFZ in degrading different initial concentrations of Rh B, ranging from 25 mg L^{-1} to 150 mg L^{-1} keeping the amount of PMS and the pH constant. When the concentration of Rh B increased from 25 mg L^{-1} to 150 mg L^{-1}, the removal efficiency dropped from 97% to 6% within 1 minute. The degradation rate constant k decreased from 3.35 min $^{-1}$ to 0.064 min $^{-1}$ in this process (**Figure S4**). The removal of Rh B in higher concentrations (150 mg L^{-1}) took longer and reached ~ 64% degradation in 10 minutes. After this time, the rate of dye reduction decreased from 3.2 mg min^{-1} to 0.1 mg min^{-1}, resulting in a

8

total reduction of 74% after 20 minutes. Up to Rh B concentration of 50 mg L^{-1}, complete degradation took place in 10 minutes.

Figure 4b describes the effect of PMS dosages on Rh B degradation using a constant Rh B concentration of 50 mg L^{-1} and a fixed the amount of HFZ. When the PMS dosage was 0.5 mM, 27% of Rh B was removed within 1 minute, and the removal efficiency reached 77.3% at 20 minutes, indicating that the catalytic performance was unsatisfactory with insufficient PMS concentration. However, when the PMS dosage increased from 0.5 mM to 1.5 mM, the catalytic performance improved significantly, and the degradation rate constant k value also increased from 0.197 to 0.825 min^{-1}. (**Figure S5**). When the PMS dosage is 1.5 mM, Rh B is almost completely removed within 10 minutes. However, increasing the PMS dosage to 2.5 mM did not significantly enhance the removal efficiency of Rh B, with the k value is 0.876 min^{-1}. Therefore, considering both economic and practical factors, 1.5 mM PMS is selected as the optimal dosage for catalytic degradation.
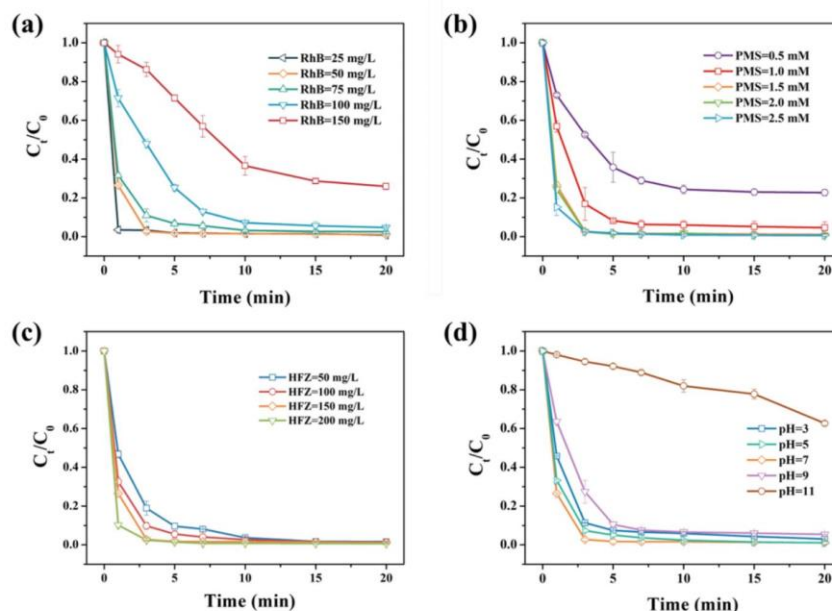
Figure 4. Effect of a) initial concentration of Rh B, b) PMS dosage, c) catalyst HFZ content, and d) the value of pH on rhodamine removal efficiency. Reaction condition: 100 mL Rh B= 50 mg L^{-1}, PMS= 1.5 mM, HFZ= 150 mg L^{-1}, pH=7, rt.

9

The effect of different HFZ contents on Rh B degradation, while keeping the amounts of PMS and RH B concentration the same, is shown in **Figure 4c**. The results show that the increase of HFZ content is beneficial to Rh B degradation. As the amount of catalyst increased from 50 mg L^{-1} to 200 mg L^{-1}, the removal efficiency of Rh B also increased. The pseudo-first-order reaction rate constant also confirms this conclusion. The reaction rate constants under different HFZ dosages were 0.456, 0.583, and 0.825 min^{-1} (**Figure S6**), respectively. This is because the increase in the number of active sites in the reaction system promotes the activation of PMS and produces more reactive oxygen species. However, compared with the catalyst content of 150 mg L^{-1}, the rate constant of 200 mg L^{-1} only increased by 0.04 min^{-1}, and there was no significant improvement. This may be because the partially saturated active site in the 200 mg L^{-1} catalyst is not used when the amount of PMS is limited. Considering the catalyst cost factors, the optimal catalyst dosage selected in this study is 150 mg L^{-1}.

The initial pH value of the solution is a key factor affecting the catalytic performance of the HFZ/PMS system. The effect of the initial pH was assessed by adjusting the pH value of the solution to 3, 5, 7, 9, and 11 (**Figure 4d**). The results show that the Rh B removal efficiency is highest at pH 7, achieving 100% removal within 10 minutes. At pH 5, 97.6% of Rh B was removed within the same time frame. At pH values of 3 and 9, more than 94% of Rh B was removed within 10 minutes. However, when the pH is increased to 11, the removal efficiency significantly decreases. Only 2% of Rh B is removed within the first minute, 18.1% within 10 minutes, and 38.4% within 20 minutes. This trend is also reflected in the reaction rate constants. At pH values of 3, 5, 7, and 9, the degradation rate constant k is 0.529, 0.598, 0.825, and 0.448 min^{-1}, respectively. And when pH = 11, the reaction rate constant is only 0.0165min^{-1} (**Figure S7**). This reduced efficiency at high alkalinity is likely due to PMS self-decomposing without producing $SO4^{\cdot-}$, thus lowering the degradation efficiency of Rh B. [22] This indicates that the HFZ/PMS system exhibits excellent catalytic activity across a broad pH range (3 to 9), with the highest efficiency at pH 7.

Therefore, to further explore the application of the HFZ system in actual water bodies, we also conducted an experiment to evaluate the removal of Rh B by the HFZ/PMS system in river water taken from the Roter main river in Bayreuth, Germany, the pH value of the river water is 7.98 (**Figure 5a**). Compared with laboratory pure water, the removal process of Rh B in the river water in the early stage of the reaction is relatively slow (52.8%). The removal efficiency increased to 99% when the reaction lasted for 10 minutes ($k = 0.437$ min^{-1}) and completed degradation in about 20 minutes (**Figure S8**). This demonstrates that HFZ can maintain high

10

PMS activation performance in real water, indicating the potential for practical application of the HFZ/PMS system.
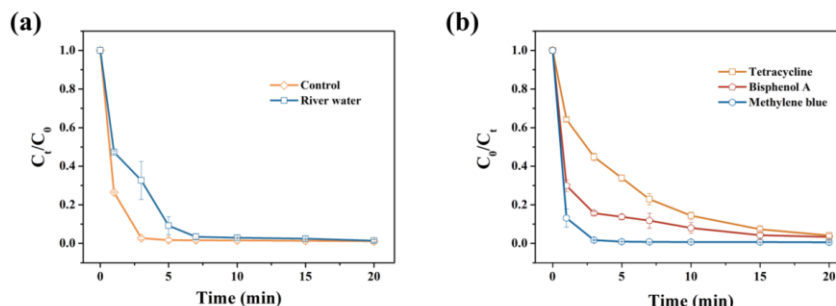
Figure 5. (a) Removal of Rh B by HFZ/PMS system in river water, rection condition: 100 mL 50 mg L^{-1} Rh B, PMS= 1.5 mM, HFZ= 150 mg L^{-1}, pH=7, rt. (b)Removal of different organic pollutants by HFZ/PMS system, reaction condition: 100 mL 50 mg L^{-1} organic pollutant, PMS= 1.5 mM, HFZ= 150 mg L^{-1}, pH=7, rt.

The system was also tested for three other typical organic pollutants methylene blue (MB), tetracycline (TC), and bisphenol A (BPA). The results are shown in **Figure 5b**. The removal efficiencies of MB, TC, and BPA in the 20 minutes HFZ/PMS system are 100%, 96.7%, and 95.9% respectively. This indicates that the HFZ/PMS system can be used to decompose a variety of organic pollutants.

To gain a deeper understanding of the reactive oxygen species produced during the reaction and to explore the removal process of Rh B, scavenger experiments were performed. Methanol (MeOH) and tert-butanol (TBA) are well-known scavengers for SO$_4^{\cdot-}$ and ·OH radicals. [23] Furfuryl alcohol (FFA) is commonly used as a scavenger for non-free radical ^{1}O$_2$, while sodium azide (NaN$_3$) can be employed to confirm the presence of ^{1}O$_2$, SO$_4^{\cdot-}$, and ·OH. [24] The results, depicted in Figure 6a, show that the addition of 1 M MeOH and TBA respectively inhibited the removal of Rh B. Within 10 minutes, the removal efficiency of Rh B decreased to 87.1% and 94.6%, respectively. The result shows that PMS produced SO$_4^{\cdot-}$ and ·OH respectively during the reaction process. However, the addition of TBA only slightly inhibited the removal of Rh B during the reaction, indicating that ·OH did not play a major role in the reaction. When 10 mM FFA was added to the reaction system, the Rh B removal efficiency decreased to 51.7% within 10 minutes, which indicated that non-free radicals ^{1}O$_2$ were also produced during the reaction. When 10 mM NaN$_3$ was added to the reaction system, it was found that Rh B could hardly be degraded. Those results confirm that the reactive oxidation species SO$_4^{\cdot-}$, ·OH, and

11

$^1O_2$ are generated, among them, $SO_4^{\bullet-}$ and $^1O_2$ play a leading role in the degradation of Rh B in the HFZ/PMS system.
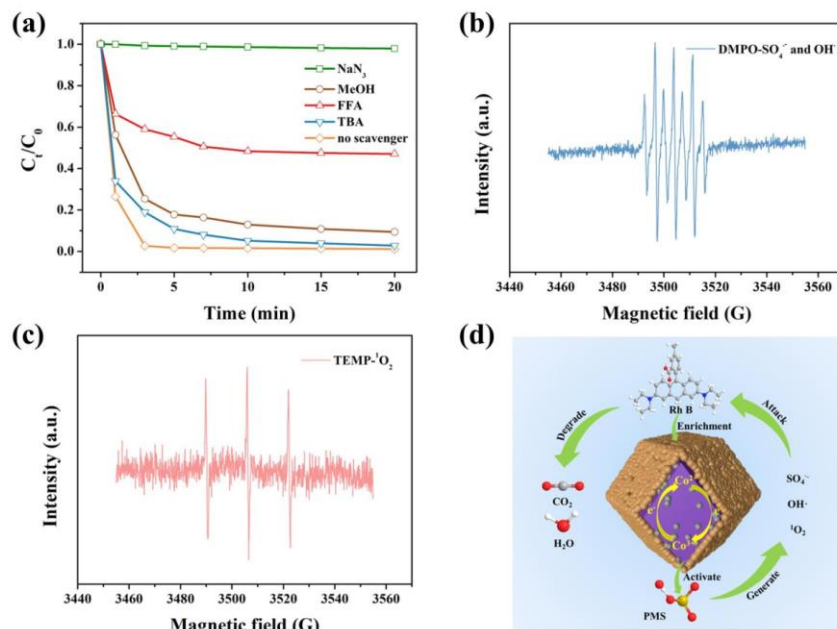
Figure 6. (a) The removal of Rh B in different scavenger systems. EPR spectra of (b) $\cdot$OH, $SO_4^{\bullet-}$ and (c) $^1O_2$ in Rh B solution. Reaction condition: 100 mL 50 mg L^{-1} Rh B, PMS= 1.5 mM, HFZ= 150 mg L^{-1}, pH=7, rt. (d) Possible degradation mechanism of Rh B in HFZ/PMS system.

Electron paramagnetic resonance (EPR) experiments were used to further identify the reactive oxidation species that may form during the degradation process of Rh B, to prove the aforementioned result. $SO_4^{\bullet-}$, $\cdot$OH, and $^1O_2$ were captured using 5, 5-dimethyl-1-pyrroline (DMPO) and 2, 6, 6-tetramethyl-4-piperidone (TEMP). As shown in **Figure 6b**, when we used DMPO as the capture agent to verify the presence of $SO_4^{\bullet-}$, $\cdot$OH, we found that there is only one DMPOX (5,5-dimethyl-2-oxo-pyrrolidine-1-oxy), the seven-element signal peak. But this does not mean that $SO_4^{\bullet-}$ and $\cdot$OH are not produced during the reaction. This is attributed to the ultrafine splitting of DMPO oxidation products, indicating that DMPO may be strongly oxidized by $SO_4^{\bullet-}$, $\cdot$OH, and other strong oxidants during the reaction. [10, 25] When TEMP was used as the capture agent for EPR experiments (**Figure 6c**), a triple signal peak was successfully

12

detected, which was the characteristic peak of TEMP-$^1O_2$. This result confirmed the generation of $^1O_2$ during the reaction.[26]

Combining the above experimental results, the possible degradation mechanism of Rh B removal by HFZ/PMS was proposed. The results are shown in **Figure 6d**. Rh B is adsorbed to the catalyst surface due to the porous structure and electrostatic interaction of the HOF shell, leading to the enrichment of Rh B molecules on the catalyst surface. This process effectively shortens the reaction pathway during the degradation process. HSO_5^- could be activated by Co^{2+} in the structure of HFZ to produce $SO_4^{\cdot-}$ and $\cdot OH$.[27] The cobalt ions state in the ZIF-67 core of HFZ can interconvert between Co^{2+} and Co^{3+}.[28] And the heterogeneous cleavage of the O-O bond in HSO_5^- produces $^1O_2$.[29] Besides, during the entire reaction process, the magnetic Fe_3O_4 in the HFZ can accelerate the charge transfer and as the electron donor promote the cycling between Co^{2+} and Co^{3+}, which will further react with PMS to generate $SO_4^{\cdot-}$, thereby speeding up the removal rate of Rh B.

To evaluate the reusability of HFZ in PMS activation, five Rh B degradation cycles were performed (**Figure 7a**). After five cycles, the removal efficiency of Rh B can still reach 93.6 %. More importantly, the XRD patterns show that the crystal structure of HFZ does not change significantly between the fresh and after use (**Figure 7b**). The above results demonstrated that HFZ, as a catalyst for activating PMS, exhibited high recyclability and good stability. Moreover, after 5 cycles of use, ICP-OES detected only 0.14 mg L^{-1} cobalt ion leaching, which indicates that under the protection of the HOF shell, cobalt ion leaching problems can be effectively slowed down during use.
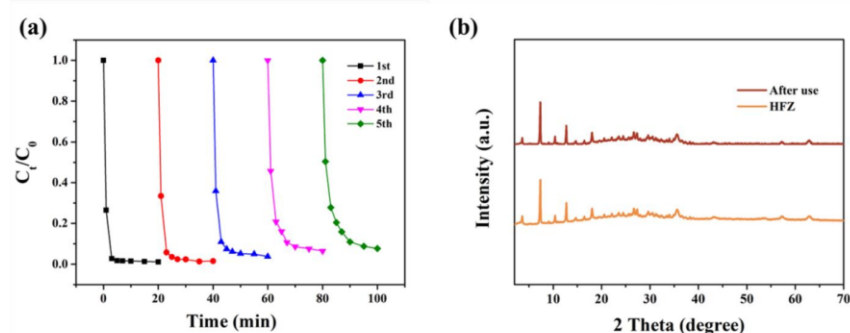
Figure 7. (a) Reusability of HFZ activated PMS for degradation of Rh B. (b) The XRD patterns of HFZ between the fresh and after use.

13

The possible degradation pathways of Rh B during the degradation process were analyzed using high-pressure liquid chromatography and mass spectroscopy (HPLC-MS), and the intermediates and their m/z values were identified (**Figure S9**). According to the experimental results and previous reports, the degradation pathway of Rh B is mainly divided into four processes as shown in **Figure S10**.[30] First, N-de-ethylation generates m/z = 387, m/z = 359, and m/z = 331 intermediates, and then the chromophore structure is broken and degraded (m/z = 255, 213, 212). With the conjugated chromophore structure Upon destruction, the reaction mixture becomes more complex, and a subsequent ring-opening process occurs, producing some primary oxidation products (m/z = 148, 99, 83), which are further degraded into smaller compounds (m/z = 74). The subsequently formed oxidation intermediates are further mineralized into water, carbon dioxide, and other small molecule compounds of inorganic salt.

3. Conclusion

In this study, the magnetic HOF-on-MOF type core-shell catalyst (HOF-on-Fe_3O_4/ZIF-67) was successfully constructed using ZIF-67 as the core, incorporated with magnetic Fe_3O_4. The morphology and crystal of the catalyst were characterized by SEM, TEM, XRD and FT-IR. The effects of Rh B concentration, PMS dosages, catalyst contents, and pH value of the initial solution on pollutant degradation efficiency were discussed in detail. The results showed that under the optimal conditions (Rh B=50 mg L^{-1}, HFZ= 150 mg L^{-1}, PMS=1.5 mM, pH=7, rt.), the HFZ/PMS system achieved 100% Rh B degradation within 10 minutes, and HFZ showed high catalytic activity for Rh B degradation in a wide range of pH values (3 - 9). Under the protection of the HOF shell, the leaching concentration of cobalt ion was 0.14 mg L^{-1} after 5 cycles. In addition, the catalyst shows satisfactory catalytic effect in different water quality and can degrade different types of organic pollutants, which provides a basis for its application in practice use. The scavenger experiment and EPR investigated the reactive oxidation species produced during the reaction of HFZ/PMS system, and proposed the possible reaction mechanism of Rhodamine degradation. The degradation pathway of Rh B was also identified by HPLC-MS. In conclusion, this study strategy provides new thought for the preparation of core-shell structure composite materials.

4. Experimental Section

Preparation of Fe_3O_4 nanoparticles: Fe_3O_4 nanoparticles were prepared based on previously reported literature. [31] In brief, 5 mmol of $FeSO_4 \cdot 7H_2O$ and 5 mmol of $FeCl_3 \cdot 6H_2O$ were dissolved in 15 mL of Milli-Q water to form a clear orange solution. This solution was then

14

added dropwise to 20 mL of 3.5 mol L^{-1} ammonia water at 60 °C under ultrasound irradiation, and the reaction was allowed to proceed for 30 minutes. The resulting black nanoparticles were separated and collected from the solution using a magnetic, washed repeatedly with water and methanol, and vacuum dried at 65 °C overnight for further use.

Preparation of HOF:[15] 100 mg H$_4$TNAPy was dissolved in 30 mL of DMF under heating at 120 °C for 2h to get a clear yellow solution. After cooling down to room temperature, the solution was poured into 200 mL of acetone under stirring (270 rpm) within 3 minutes. The suspension was stirred overnight. Afterward, a yellow powder was isolated by centrifugation at 8500 rpm for 5 minutes. The obtained yellow powder was further washed with acetone (3 x 30 mL) and then dried at room temperature.

Preparation of ZIF-67: In a typical process, 0.145 g Co(NO$_3$)$_2$·6H$_2$O and 2.37 g of 2-MeIM were each dissolved in 12 mL of water forming solutions A and B, respectively. At room temperature, solution B was quickly poured into solution A and stirred at room temperature for 12 hours to obtain purple particles. The purple particles were collected by centrifugation, washed with water and methanol (3 x 30 mL), and dried in an oven at 80 °C to obtain ZIF-67 particles.

Preparation of HOF-on-Fe₃O₄/ZIF-67 (HFZ): 115 mg of Fe$_3$O$_4$ was dispersed in 16 mL of water to form solution A. Separately, 290 mg of Co(NO$_3$)$_2$·6H$_2$O and 4.7 g of 2-MeIM were dissolved in 16 mL of water to create solutions B and C, respectively. At room temperature, solution B was added to solution A while stirring. After 1 hour, solution C was introduced to the mixture, and stirring continued for an additional 12 hours. The Fe$_3$O$_4$/ZIF-67 particles were then collected using a magnet for later use. Next, 100 mg of H$_4$TNAPy was dissolved in 30 mL of DMF and heated at 120 °C for 2 hours to obtain a clear yellow solution. After cooling to room temperature, this solution was poured into 200 mL of a 500 mg L^{-1} Fe$_3$O$_4$/ZIF-67 acetone dispersion within 3 minutes while stirring at 270 rpm. The suspension was stirred overnight. Finally, the HFZ particles were collected using the magnet, washed with acetone (5 x 30 mL), and dried in a vacuum oven at 80 °C. The preparation of HOF-on-ZIF-67 is the same as HFZ except that there is no need to add solution A (Fe$_3$O$_4$), and solution B is added directly to solution C.

Adsorption experiment: In the adsorption experiment, the adsorption conditions are set as follows: the adsorbent dosage of 10 mg, a solution volume of 20 mL, a temperature of 25 °C, and a stirring speed of 200 rpm. The concentration of residual dye solution is analyzed using UV–vis spectroscopy, by measuring the absorbance at the maximum absorption wavelength

15

of $\lambda_{max} = 555$ nm. The concentrations of the dye (Rh B) before and after adsorption are determined from the standard calibration curve.

The adsorption performance of the adsorbents was calculated by the following equation:

$$q_{\mathbf{e}} = (C_0 - C_e) \cdot V \cdot m^{-1}$$

where $q_{\mathbf{e}}$ (mg g^{-1}) is the adsorption capacity of Rh B at equilibrium; C_0 (mg L^{-1}) is the initial Rh B concentration; C_e (mg L^{-1}) is the residual Rh B concentration at equilibrium; V (L) is the volume of Rh B solution used and m (g) is the mass of adsorbent used.

Catalytic degradation experiment: Degradation experiments were performed in 200 mL glass containers at ambient temperature. Stir the solution at a speed of 300 rpm to ensure thorough mixing. Adjust the initial pH of the solution with 0.1M NaOH or 0.1M HCl. In a general reaction procedure, 100 mL, 50 mg L^{-1} of Rh B and PMS were added to the glass container, and then the reaction was activated by adding a catalyst (HFZ). At specific time intervals, 1 mL of the reaction solution was collected and used for magnetic separation, and then 0.5 mL of the reaction solution was immediately mixed with 0.5 mL of methanol to quench the reaction. Using a UV-Vis spectrophotometer to determine the reaction concentrations. All experiments were conducted in triplicate, and average values with standard deviations were presented.

Analytic methods: The concentration of Rh B, MB, and TC in aqueous solution is measured by UV-vis spectrophotometer (Jasco Spectrometer V-670) at wavelength 555 nm, 665 nm, and 355 nm. The concentration of BPA in aqueous solution is measured by HPLC-MS, a UV wavelength of 230 nm. Rh B degradation intermediates were identified using high-pressure liquid chromatography-mass spectroscopy (HPLC-MS, VWR Chemicals, Germany), a welch ultimate C18 column (2.1×100 mm), a UV wavelength of 555 nm, mobile phase water (eluent A)/methanol (eluent B), gradient elution was listed as follows: 45% A/55% B (0~1.5 min), 25% A/75% B (1.5~14 min), 45% A/55% B (14~15 min), 45% A/55% B (15~25 min).

The degradation efficiency of pollutants was calculated according to Equation:

$$R\% = \frac{100\% \times (C_0 - C_t)}{C_0}$$

Which R is the degradation efficiency of pollutants (%), and C_0 is the concentration of pollutants at time 0, C_t is the concentration of pollutants at time t (mg L^{-1}).

And the kinetics of pollutants degradation process was investigated according to the pseudo first-order kinetics Equation:

$$-\ln(\frac{C_t}{C_0}) = \mathbf{k}t$$

16

WILEY-VCH

Where k is the degradation rate constant and t is the degradation time (min). Besides, all degradation experiments were repeated, and the average value with the standard deviation was presented for the results.

References

[1]   a) Y. Yan, Z. Wei, X. Duan, M. Long, R. Spinney, D. D. Dionysiou, R. Xiao, P. J. J. Alvarez, *Environ. Sci. Technol.* **2023**, 57, 12153. b) J. Wang, S. Wang, *Chem. Eng. J.* **2020**, 401, 126158.

[2]   a) Y. Chen, H. Kang, M. Cheng, G. Zhang, G. Wang, H. Liu, W. Xiao, Y. Liu, H. Jiang, *Adv. Funct. Mater.* **2024**, 34, 2309223. b) J. Lee, U. Von Gunten, J. H. Kim, *Environ. Sci. Technol.* **2020**, 54(6), 3064-3081.

[3]   a) C. Guo, M. Cheng, G. Zhang, W. Xiong, C. Zhou, B. Song, H. Liu, *Environ. Sci. Nano*, **2023**, 10, 1528-1552. b) J. Tan, X. Zhang, Y. Lu, X. Li, Y. Huang, *Langmuir*, **2023**, 40(1), 21-38.

17

WILEY-VCH

[4]   X. Zheng, X. Niu, D. Zhang, M. Lv, X. Ye, J. Ma, M. Fu, *Chem. Eng. J.* **2022**, 429, 132323.

[5]   a) T. Yu, H. Chen, T. Hu, J. Feng, W. Xing, L. Tang, W. Tang, *Appl. Catal. B* **2024**, 342, 123401. b) Y. Gao, T. Wu, C. Yang, C. Ma, Z. Zhao, Z. Wu, S. Cao, W. Geng, Y. Wang, Y. Yao, Y. Zhang, C. Cheng, *Angew. Chem. Int. Ed.* **2021**, 60, 22513 – 22521. c) S. An, G. Zhang, T. Wang, W. Zhang, K. Li, C. Song, JT. Miller, S. Miao, J. Wang, X. Guo, *ACS Nano* **2018**, 12, 9441-9450. d) Z. Wang, E. Almatrafi, H. Wang, H. Qin, W. Wang, L. Du, S. Chen, G. Zeng, P. Xu, *Angew. Chem. Int. Ed.* **2022**, 61, e202202338.

[6]   L. Chen, H. Ji, J. Qi, T. Huang, C. C. Wang, W. Liu, *Chem. Eng. J.* **2021**, 406, 126877.

[7]   a) H. S. Jadhav, H. A. Bandal, S. Ramakrishna, H. Kim, *Adv. Mater.* **2022**, 34, 2107072. b) R. Banerjee, A. Phan, B. Wang, C. Knobler, H. Furukawa, M. O'Keeffe, O. M. Yaghi, *Science* **2008**, 319, 939. c) G. Zhong, D. Liu, J. Zhang, *J. Mater. Chem. A* **2018**, 6(5), 1887-1899. d) D. Saliba, M. Ammar, M. Rammal, M. Al-Ghoul, M. Hmadeh, *J. Am. Chem. Soc.* **2018**, 140(5), 1812-1823.

[8]   a) M. Kohantorabi, S. Giannakis, G. Moussavi, M. Bensimon, M. R. Gholami, C. Pulgarin, *J Hazard. Mater.* **2021**, 413, 125308. b) S. Ma, D. Yang, Y. Guan, Y. Yang, Y. Zhu, Y. Zhang, T. Yao, *Appl. Catal. B* **2022**, 316, 121594. c) C. Zhu, S. Zhao, Z. Fan, H. Wu, F. Liu, Z. Chen, A. Li, *Adv. Funct. Mater.* **2020**, 30(49), 2003947.

[9]   Y. Li, J. Feng, Y. Zhang, C. Wang, J. Hao, Y. Wang, X. Cheng, *Chemosphere*, **2023**, 311, 137038.

[10]   Z. Wu, Y. Wang, Z. Xiong, Z. Ao, S. Pu, G. Yao, B. Lai, *Appl. Catal. B* **2020**, 277, 119136.

[11]   H. Wan, J. Yan, C. Guo, Q. Cui, W. Zhang, *Environ. Res.* **2022**, 204, 111986.

[12]   a) R. B. Lin, Y. He, P. Li, H. Wang, W. Zhou, B. Chen, *Chem. Soc. Rev.* **2019**, 48(5), 1362-1389. b) R. B. Lin, B. Chen, *Chem*, **2022**, 8, 2114-2135. c) I. Hisaki, C. Xin, K. Takahashi, T. Nakamura, *Angew. Chem. Int. Ed.* **2019**, 12, 11160-70. d) C. A. Halliwell, S. E. Dann, J. Ferrando-Soria, F. Plasser, K. Yendall, E.V. Ramos-Fernandez, G.T. Vladisavljević, M.R. Elsegood, A. Fernandez, *Angew. Chem.* **2022**, 134, e202208677.

[13]   a) X. Song, Y. Wang, C. Wang, D. Wang, G. Zhuang, K. O. Kirlikovali, O. K. Farha, *J. Am. Chem. Soc.* **2022**, 144(24), 10663-10687. b) S. Goswami, K. Ma, J. Duan, K. O. Kirlikovali, J. Bai, J. T. Hupp, O. K. Farha, *Langmuir*, **2022**, 38, 1533-1539. c) B. Wang, R. B. Lin, Z. Zhang, S. Xiang, B. Chen, *J. Am. Chem. Soc.* **2020**, 142,14399-14416.

[14]   R. Wagia, I. Strashnov, M. W. Anderson, M. P. Attfield, *Cryst. Growth Des.* **2018**, 18, 695-700.

18

103

WILEY-VCH

[15]   K. Ma, P. Li, J. H. Xin, Y. Chen, Z. Chen, S. Goswami, O. K. Farha, *Cell Rep. Phys. Sci.* **2020**, 1.

[16]   Y. Du, C. Ding, S. Agarwal, *Adv. Energy Sustainability Res.* **2024**, 5(4), 2300218.

[17]   Z. Dong, Q. Zhang, B. Y. Chen, J. Hong, *Chem. Eng. J.* **2019**, 357, 337-347.

[18]   Y. Wei, Y. Han, X. Hu, Y. Lin, X. Wang, X. Deng, *Procedia Eng.* **2012**, 27, 632-637.

[19]   a) Q. Yang, S. Ren, Q. Zhao, R. Lu, C. Hang, Z. Chen, H. Zheng, *Chem. Eng. J.* 2018, **333**, 49. b) Z. Li, H. Dai, M. Yang, Y. Fu, Y. Ying, Y. Li, *J. Mater. Chem. A* **2018**, 6(8), 3402-3413.

[20]   Y. Guo, C. Zhou, X. Lv, S. Du, M. Sui, *Sep. Pur.f. Technol.* **2024**, 128729.

[21]   a) X. Zhang, J. Zhang, B. Hou, X. Yang, J. Ren, C. Shao, *Appl. Surf. Sci.*, **2024**, *643*, 158663. b) X. Wu, D. Sun, H. Ma, C. Ma, X. Zhang, J. Hao, *Colloid Surface A*, **2022**, 637, 128278. c) J. Cui, T. Liu, Q. Zhang, T. Wang, X. Hou, *Chem. Eng. J.* **2021**, 404, 126453. d) S. Lu, S. You, J. Hu, X. Li, L. Li, *RSC adv.* **2024**, 14, 7528-7539. e) L. Peng, X. Gong, X. Wang, Z. Yang, Y. Liu, *RSC adv.* **2018**, 8, 26377-26382. f) Y. Li, X. Yan, X. Hu, R. Feng, M. Zhou, *Chem. Eng. J.* **2019**, 375, 122003.

[22]   a) F. Wang, H. Fu, F. X. Wang, X. W. Zhang, P. Wang, C. Zhao, C. C. Wang, *J Hazard. Mater.* **2022,** 423, 126998. b) D. L. Ball, J. O. Edwards, *J. Am. Chem. Soc.* **1956**, 78(6), 1125-1129.

[23]   a) T. B. Nguyen, V. A. Thai, C. W. Chen, C. P. Huang, R. A. Doong, L. Chen, C. D. Dong, *Sep. Pur.f. Technol.* **2022**, 288, 120719. b) Y. Xu, J. Ai, H. Zhang, *J Hazard. Mater.* **2016**, 309, 87-96.

[24]   a) Z. Weng, Y. Lin, S. Guo, X. Zhang, Q. Guo, Y. Luo, B. Han, *Angew. Chem.* **2023**, 135(43), e202310934. b) Y. Li, J. Li, Y. Pan, Z. Xiong, G. Yao, R. Xie, B. Lai, *Chem. Eng. J.* **2020**, 384, 123361. c) M. Ahmadi, F. Ghanbari, *Environ. Sci. Pollut. R.* **2018**, 25, 6003-6014.

[25]   W. Ma, N. Wang, T. Tong, L. Zhang, K. Y. A. Lin, X. Han, Y. Du, *Carbon*, **2018**, 137, 291-303.

[26]   S. C. Mei, G. X. Huang, X. H. Rui, L. Li, M. K. Ke, X. Q. Pan, Y. Yu, *Adv. Funct. Mater.* **2022**, 32(18), 2111184. b) Y. Zeng, J. Deng, N. Zhou, W. Xia, Z. Wang, B. Song, C. Zhou, *Small*, **2024**, 2311552.

[27]   C. Wang, P. Cheng, Y. Yao, Y. Yamauchi, X. Yan, J. Li, J. Na, *J. Hazard. Mater.* **2020**, 392, 122164.

[28]   W. Zheng, Y. Sun, Y. Gu, *Chem. Eng. J.* **2023**, 459, 141668.

[29]   X. Wu, D. Sun, H. Ma, C. Ma, X. Zhang, J. Hao, *Colloid Surface A* **2022**, 637, 128278.

[30]   a) Z. He, C. Sun, S. Yang, Y. Ding, H. He, Z. Wang, *J Hazard. Mater.* **2009,** 162(2-3),

19

WILEY-VCH

1477-1486. b) Q. Zhong, J. Liu, J. Wang, Y. Li, J. Li, G. Zhang, *Chemosphere* **2022**, 300, 134564.

[31] M. Chen, N. Wang, X. Wang, Y. Zhou, L. Zhu, *Chem. Eng. J.* **2021**, 413, 127539.

20

105

WILEY-VCH

Supporting Information

In-situ constructed magnetic core-shell (hydrogen-bonded organic framework-on-metal-organic framework) structure: an efficient catalyst for peroxymonosulfate activation

Yingying Du, Chenhui Ding, Chao Deng, Susanta Banerjee, and Seema Agarwal*

Y. Du, C. Ding, C. Deng, Prof. S. Agarwal
Advanced Sustainable Polymers, Macromolecular Chemistry 2, and Bavarian Polymer Institute
University of Bayreuth
Universitätsstrasse 30, 95440 Bayreuth, Germany
E-mail: agarwal@uni-bayreuth.de

Prof. S. Banerjee
Materials Science Centre
Indian Institute of Technology Kharagpur
Kharagpur-721302, India
Yingying Du, Chenhui Ding, Chao Deng, S. Banerjee, and Seema Agarwal*

1

Experimental section

Materials and Chemicals

Cobalt nitrate hexahydrate (Co(NO$_3$)$_2$·6H$_2$O), and Bisphenol A (BPA) were attained from Alfa Aesar. 2-methylimidazole (2-MeIM), Oxone® (Peroxymonosulfate, 2KHSO$_5$·KHSO$_4$·K$_2$SO$_4$), and Tetracycline (TC) were brought from Thermo Fisher Scientific. Rhodamine B (Rh B) was purchased from Sigma Aldrich. Iron(II) sulfate heptahydrate (FeSO$_4$·7H$_2$O) and sodium azide (NaN$_3$) were supplied by Grussing GmbH. FeCl$_3$·6H$_2$O, Methylene blue (MB), were purchased from Riedel-de Haen. 6,6',6",6"'-(Pyrene-1,3,6,8-tetrayl)tetrakis(2-naphthoic acid) (H$_4$TNAPy) was obtained from BLD pharm. Methanol (MeOH, $\geq$ 99.7%), tert-butyl alcohol (TBA, $\geq$ 99.7%), Dimethylformamide (DMF, $\geq$ 99.5%), Acetone, ammonia solution (NH$_3$·H$_2$O), sodium hydroxide (NaOH), and Hydrochloric acid (HCl, 37%) were supplied by Fisher Chemical company. All aqueous solutions were prepared by self-produced Milli-Q water in the laboratory unless otherwise noted.

Characterization

The morphology was characterized by scanning electron microscopy (SEM, FEI Quanta FEG 250) transmission electron microscopy (TEM), and high-angle annular dark field scanning transmission electron microscopy (HAADF-STEM, FEI Themis Z, USA). Energy Dispersive X-ray spectroscopy (EDS) was tested by scanning electron microscopy (SEM, Zeiss LEO 1530). The X-ray diffraction (XRD) patterns of the samples were obtained on a Bragg-Brentano type diffractometer (XPERT-PRO, PANalytical B.V.) with Cu-Kα X-ray radiation (λ = 1.540598 Å). The functional groups of all the samples were analyzed using Fourier transform infrared spectra (FT-IR, Digilab Excalibur FTS-3000). Electrochemical impedance spectroscopy (EIS) and Tafel curves were studied using an electrochemical workstation (GAMRY instruments). The magnetic properties of the samples were analyzed using a vibrating sample magnetometer (VSM, LakeShore 7410). The reactive oxygen species (ROS) were detected by electron

2

107

WILEY-VCH

paramagnetic resonance (EPR) spectroscopy on a BRUKER EMXPLUS (Brooke (Beijing) Technology Co., LTD), employing DMPO and TEMP as spin trapping agents. The concentration of leached Co ions was analyzed by an inductively coupled plasma-optical emission spectrometer (ICP-OES, PerkinElmer, Avio ^{TM} 200, America).

Electrochemical measurements: the EIS measurements were performed in a three-electrode cell with an Ag/AgCl as the reference electrode, a platinum foil as the counter electrode, and the bias in the range from 0.01 Hz to 10 Hz. The electrolyte was Na_2SO_4 (1 M, pH = 7).

The working electrode was prepared as follows: 3.5 mg of HOF-on-Fe_3O_4/ZIF-67 and HOF-on-ZIF-67 were dispersed in 500 µL ethanol, respectively. Then 50 µL Nafion (5 %) was added into the solution. After sonicating for 4 h 10 µL of the suspension was deposited by drop-coating directly onto a 0.071 cm^2 glassy carbon electrode at room temperature, and dry at room temperature for 5 hours to obtain the working electrode.

Linear sweep voltammetry (LSV) was recorded as the potential was swept from -1.2 V to 1.2 V at a scan rate of 5 mV s^{-1}.

EPR experiment: 15 mg PMS is added to 5 ml water or methanol, and then 5 mg MOF catalyst (HOF-on-Fe_3O_4/ZIF-67) is added. React for about 1 minute, extract 1 mL of the reaction solution, and add 11 µL DMPO and TEMP (100 mM). Shake the mixed solution between the capture agent and the active material for about 30 seconds. After the complete reaction, inject it into the quartz capillary tube and take it immediately to process the EPR test.

3
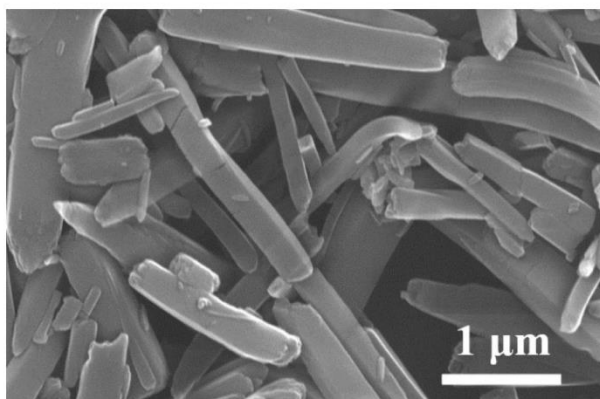
WILEY-VCH

Figure

Figure S1. SEM image of HOF.

4
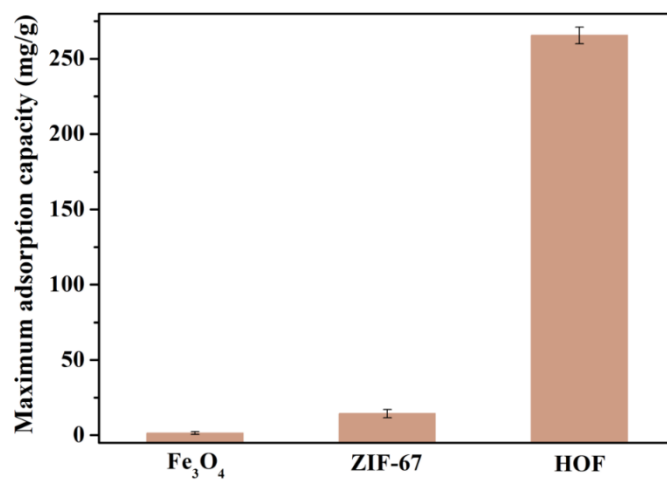
Figure S2. The maximum adsorption capacity of Rh B by Fe_3O_4, ZIF-67, and HOF.
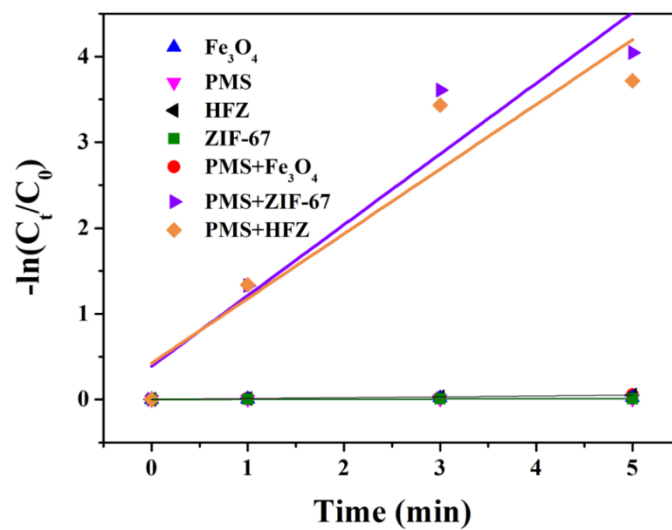
Figure S3. The kinetic rates of Rh B degradation under different catalytic conditions.

6

111
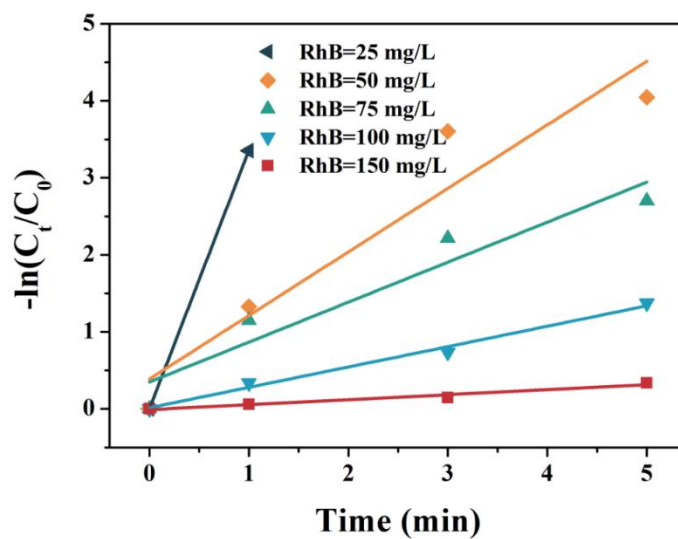
Figure S4. The kinetic rates of Rh B degradation under different initial concentrations of Rh B solution.

7
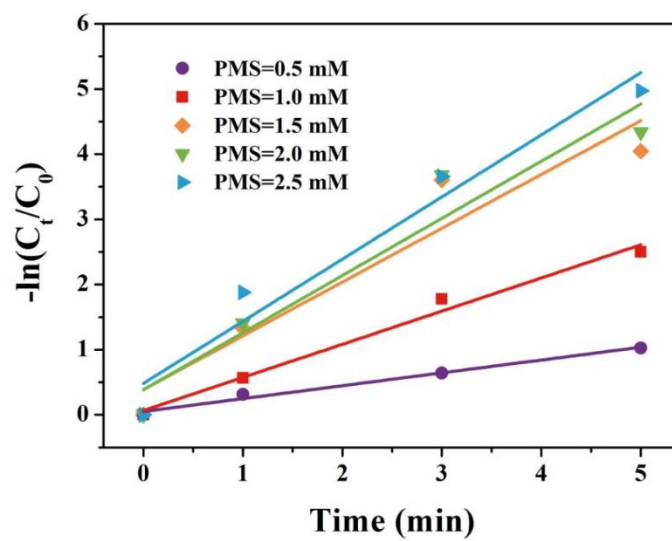
WILEY-VCH

Figure S5. The kinetic rates of Rh B degradation under different dosages of PMS.

8

113
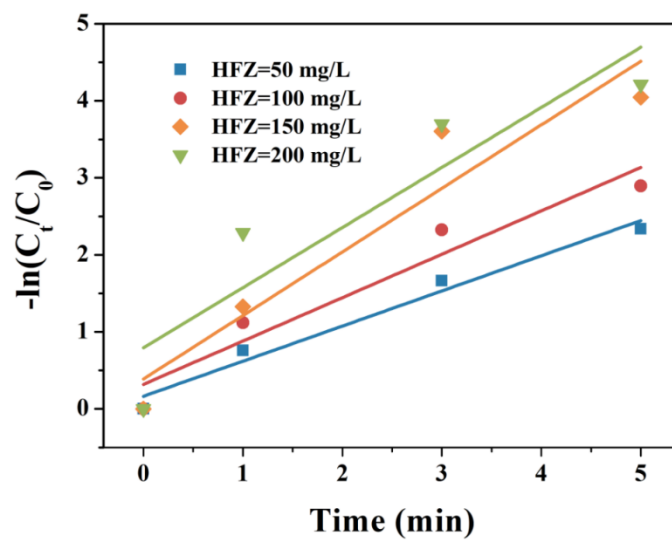
Figure S6. The kinetic rates of Rh B degradation under different contents of HFZ.

9

114
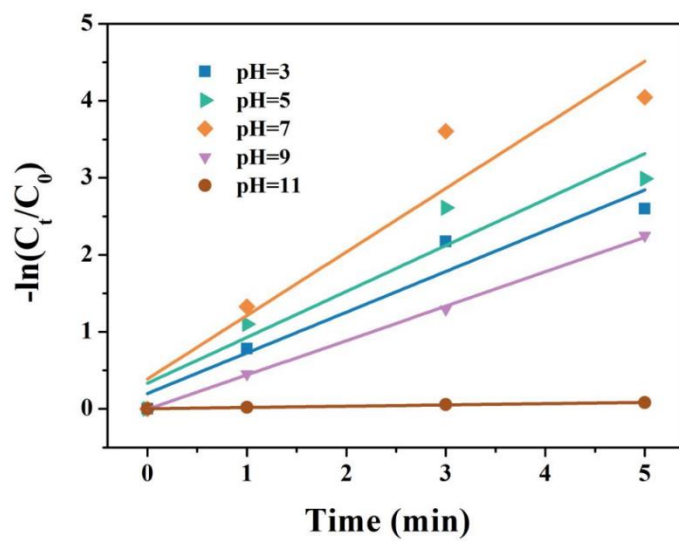
Figure S7. The kinetic rates of Rh B degradation under different pH values.

10

115
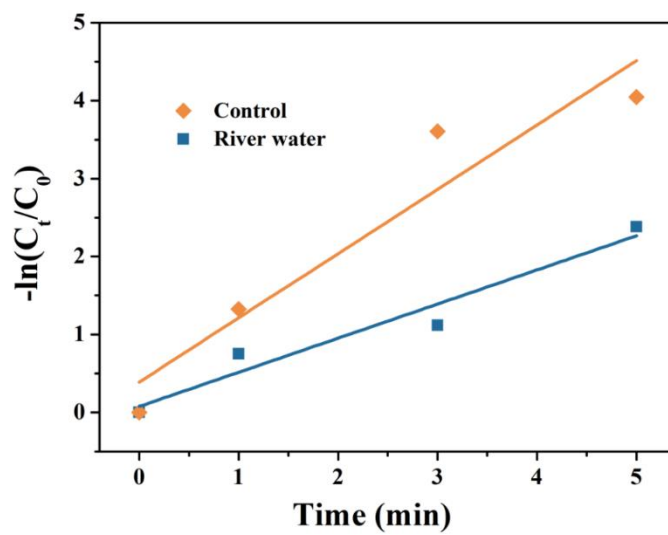
Figure S8. The kinetic rates of Rh B degradation under different water matrices.

11

WILEY-VCH
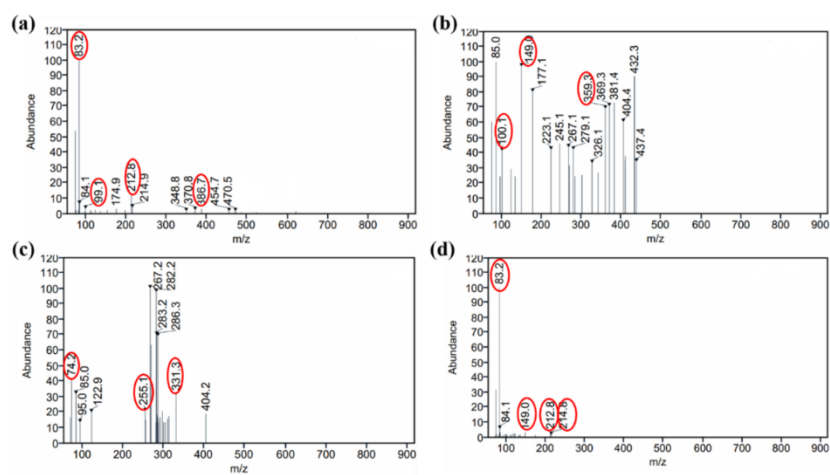
Figure S9. HPLC-MS spectra of intermediates found in the degradation of Rh B at different reaction times a) 1 minute, b) 3 minutes, c) 5 minutes, d) 7 minutes.

12

117
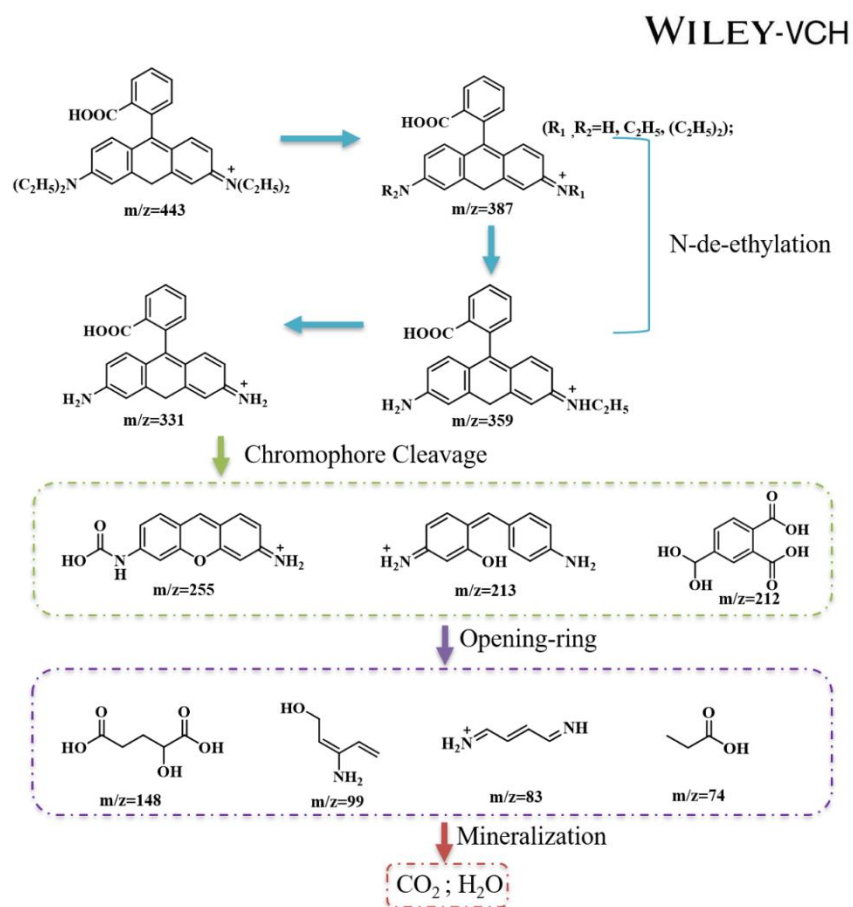
Figure S10. Possible degradation pathway of Rh B.

13

118

4.2 Template-assisted Preparation of Self-standing 2D-MOF Membranes for Application in Cascade Reactions

Yingying Du, Chenhui Ding, Jana Timm, Roland Marschall, Seema Agarwal. Template-assisted Preparation of Self-standing 2D-MOF Membranes for Application in Cascade Reactions. ChemCatChem, **2022**, 14(22), e202201040.

Template-assisted Preparation of Self-standing 2D-MOF Membranes for Application in Cascade Reactions

Yingying Du,[a] Chenhui Ding,[a] Jana Timm,[b] Roland Marschall,[b] and Seema Agarwal*[a]

Self-standing metal-organic framework (MOF) membranes open up several application areas where their use in the powder form is either not possible or non-sustainable. Most MOF membranes are prepared as a thin layer either on a supporting substrate or used as a composite membrane with additional supporting material. In this work, we present the preparation procedure for making highly stable, easy-to-handle, reusable, efficient pure MOF membranes (UiO-66-SO$_3$H and UiO-66-NH$_2$ membranes; thickness 240 ± 12 μm and 265 ± 10 μm, respectively) with hollow fiber morphology and their use in cascade reactions in

one-pot catalyzed by incompatible acid-base in tea-bag-type concept. The catalytic performance of the catalyst membranes was tested by reacting benzaldehyde dimethyl acetal with three active methylene compounds. The membranes exhibited excellent catalytic activity in cascade reactions in one pot (the yield of the product was as high as 99.9%) and can be reutilized up to 15 times without any significant loss in activity. Stable pure MOF membranes, as shown in this work, would be of interest for several other applications beyond catalysis.

Introduction

Metal-organic frameworks (MOFs) with large surface area, tunable pore size, porosities, and high thermal and chemical stability emerged as important porous materials for several applications, such as gas separation, oil-water separation, etc.[1] MOFs are framework structures formed by the self-assembly of metal clusters and organic ligands through coordination bonds as an insoluble and post-synthesis non-processable powder.[2] MOF was grown on a substrate using an in-situ growth method to enable their use in several application areas where a film is required. One of the methods utilizes immersion of an inorganic substrate in a MOF reaction solution.[3] Further improvement is made by modifying the inorganic surface that provides nucleation sites for MOF's growth and improves the substrate-MOF adhesion.[4] Other methods using already prepared MOF nanoparticles (e.g., ZIF-8) as seeds for the growth of thin MOF film on an inorganic or polymer substrate are also studied.[5]

The use of MOF in heterogenous catalysis in one-pot cascade reactions is recently getting more and more attention as a sustainable alternative to multi-step reactions.[6] The intermediate processing steps, such as the removal and

purification of products at each stage, are eliminated in one-pot cascade reactions, simplifying the synthetic procedure, reducing the solvents' use, and minimizing waste generation.[7] Besides MOF, several examples of cascade reactions using different catalysts (homogenous, enzymes, and heterogenous) for an individual sequence of reactions in a cascade are also known.[8]

One-pot cascade reactions with catalysts that deactivate each other are more challenging as they require carefully designed catalyst support architectures that keep the individual catalysts isolated from each other in an active state.[9] The incompatible catalysts which deactivate each other on coming into contact are called Wolf-Lamb-type catalysts. Moreover, easy and complete recovery after the reaction is of utmost importance for the sustainable use of catalysts. The recovered catalysts can be reused in several other catalytic reactions without losing activity. This makes the design of catalyst support architecture furthermore challenging.

Several efforts are invested in providing solutions to this challenge, and different catalytic supports keeping the two or more incompatible active catalysts isolated from each other in one pot are reported in the literature. For this, polymer resins and magnetic nanoparticles,[10] acidic- and basic-layered silicates,[11] zeolites,[12] and metal-organic frameworks (MOFs)[13] are highlighted.

MOFs as catalyst support has increased in the last years due to high porosity, specific surface area, and possibilities of tuning their structure.[14] In particular, acid-base bifunctional MOF powder is an effective catalyst for cascade reactions in one pot.[15] Complex catalyst supports, such as egg yolk-shell structured covalent organic framework (COF)@ MOF (YS-COF@MOF), were also used for the site-separation of acidic and basic groups.[16] MOF is prepared and subsequently used mostly in the form of nanoparticles, which can agglomerate during reactions. Also, retrieving MOF nanoparticles requires an additional filtration or magnetic separation step.[17] Future efforts are

[a] Y. Du, C. Ding, S. Agarwal
Macromolecular Chemistry and Bavarian Polymer Institute
University of Bayreuth
Universitätsstrasse 30, 95440 Bayreuth (Germany)
E-mail: agarwal@uni-bayreuth.de
[b] J. Timm, R. Marschall
Department of Chemistry
Physical Chemistry IIII
University of Bayreuth
Universitätsstrasse 30, 95440 Bayreuth (Germany)

Supporting information for this article is available on the WWW under https://doi.org/10.1002/cctc.202201040

needed to design efficient incompatible catalyst supports that are easily reusable.

Previously, we reported a teabag-type concept for reusable heterogeneous catalysis in which catalysts can be removed easily, like a teabag from tea, and reused. For example, gold nanoparticles (AuNPs) were incorporated in high surface-to-volume hollow polymer fibers, forming a porous nonwoven membrane by randomly laying these fibers by electrospinning. It catalyzed the hydrolytic oxidation of dimethyl phenyl silane and the alcoholysis of dimethyl phenyl silane with n-butanol. The catalytic non-woven was taken out for reuse in the same way as a teabag after use.[18] Keeping our focus on the tea-bag-type concept for catalysts' reusability, we later prepared catalytic supports for incompatible acid and base catalysts. We electrospun and later cross-linked the fibers in nonwoven prepared from -SO$_3$H and -NH$_2$ functional polymers and used them in one-pot cascade reactions: deacetylation-and subsequent reaction of an aldehyde with reactive methylene compounds.[19] Efficient catalysis was observed, but the soft polymer catalyst membranes were easily swollen by the solvents used for reactions to form a gel, reducing the catalyst's service life.

In this work, we present a preparation procedure for making highly stable, easy-to-handle, reusable, efficient self-standing pure MOF membranes based on well-known MOF (UiO-66)[20] for use in acid-base catalyzed cascade reactions in one-pot in tea-bag-type concept. After use, the catalyst membranes can be simply removed, washed, and reused for the next cycles of reactions. A procedure for making such self-standing MOF membranes with functional groups —SO$_3$H and —NH$_2$ is described, followed by detailed studies regarding their catalytic ability in cascade reactions in one pot. The catalyst membranes exhibited excellent catalytic activity in the acid-base catalyzed reactions (the yield was as high as 99.9%). Moreover, it reveals the same activity on reusing at least 15 catalytic cycles. The details of the material preparation and use in one-pot acid-base catalyzed reactions are described in detail in the results and discussion section.

Results and discussion

The synthesis strategy of making MOF (UiO-66-SO$_3$H) (acid-functionalized) and MOF (UiO-66-NH$_2$) (base-functionalized) individual porous membranes is shown in Figure 1. First, a fiber membrane of polyacrylonitrile (PAN) as a template polymer, together with ZrCl$_4$, was obtained by electrospinning a mixed solution of ZrCl$_4$ and PAN in DMF. The optical photographs of the PAN/ZrCl$_4$ membrane are shown in Figure S1. The membrane was obtained as a non-woven by random deposition of fibers (average diameter 500 nm and thickness $78 \pm 10 \mu m$) (Figure S1). Next, using the in-situ growth method, MOF (UiO-66-SO$_3$H and UiO-66-NH$_2$) were grown on PAN membrane using the acetic acid catalyst in the water together with either 2-aminobenzenedicarboxylic acid (BDC-NH$_2$) or 2-sulfobenzenedicarboxylic acid monosodium salt (BDC-SO$_3$Na). In the next step, the template polymer, PAN was removed by Soxhlet extraction with DMF leaves behind UiO-66-SO$_3$H and UiO-66-NH$_2$ membranes of thickness $240 \pm 12 \mu m$ and $265 \pm 10 \mu m$, respectively.

A scanning electron microscope (SEM) was used to characterize the morphology of the synthesized UiO-66-SO$_3$H/-NH$_2$ membranes before and after PAN removal, as shown in Figure 2. Figures 2a, and 2b are PAN/UiO-66-SO$_3$H and PAN/UiO-66-NH$_2$ membranes, respectively. Through the in-situ growth, a large amount of MOF grows on the surface of PAN fiber and completely wraps them. Figure 2c, and 2d are the surface morphologies of the UiO-66-SO$_3$H membrane and UiO-66-NH$_2$ membrane observed under SEM after removing the template polymer PAN by Soxhlet extraction. After removing PAN, the membrane remained intact. Figure 2e, and 2f are the cross-sectional images of UiO-66-SO$_3$H and UiO-66-NH$_2$ membranes, respectively, after the removal of PAN, which shows

Figure 1. Strategy to fabricate the self-standing UiO-66-SO$_3$H and UiO-66-NH$_2$ membranes (top) and the reaction scheme to prepare corresponding MOFs (bottom).
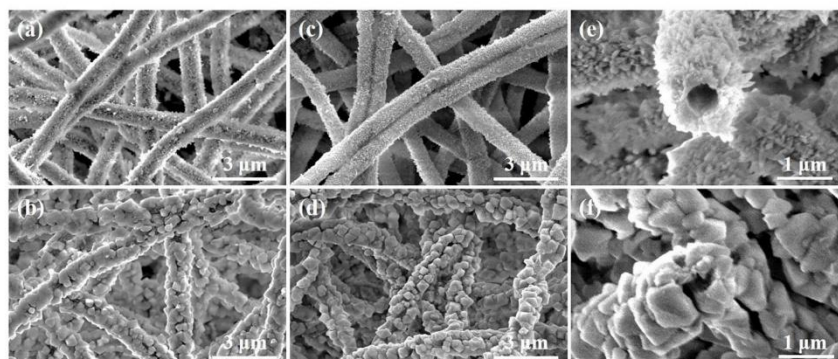
Figure 2. SEM morphology of a) PAN/UiO-66-SO₃H, b)PAN/UiO-66-NH₂, c) UiO-66-SO₃H, d) UiO-66-NH₂, Cross-sectional SEM morphology of e) UiO-66-SO₃H, f) UiO-66-NH₂ membranes.

hollow MOF fibers. The optical photographs of UiO-66-SO₃H and UiO-66-NH₂ membranes are shown in Figure S1.

The distinct peaks at $2\theta = 7.52°$, $8.69°$ and the absence of a peak at $2\theta = 17.07°$ originating from the template polymer (PAN) (Figure 3a) in XRD confirmed the preparation of UiO-66-SO₃H/-NH₂ membranes.[21] Compared with MOF powder, the characteristic peaks of MOF membranes are broader. But the main characteristic peak still exists, indicating that Soxhlet
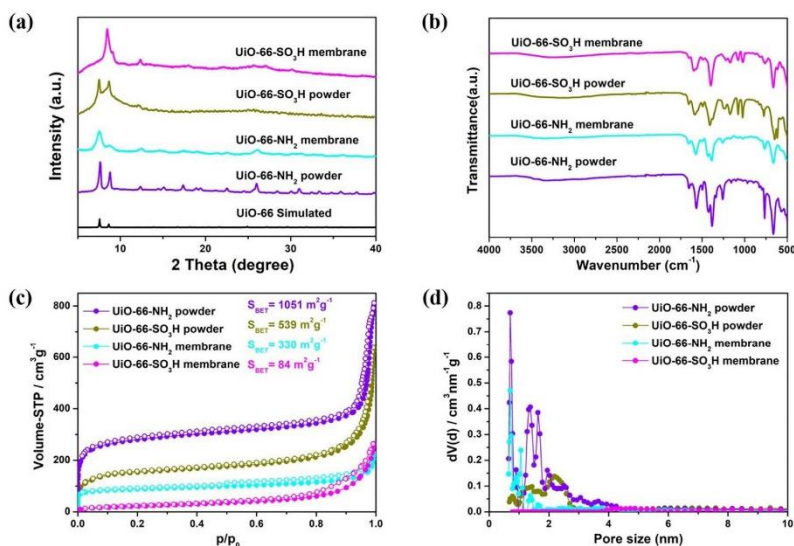
Figure 3. a) XRD patterns of UiO-66 simulated, UiO-66-SO₃H powder, UiO-66-SO₃H membrane, UiO-66-NH₂ powder and UiO-66-NH₂ membrane. b) FT-IR spectra of UiO-66-SO₃H powder, UiO-66-SO₃H membrane, UiO-66-NH₂ powder and UiO-66-NH₂ membrane. c) N₂ physisorption isotherms of UiO-66-SO₃H powder, UiO-66-SO₃H membrane, UiO-66-NH₂ powder and UiO-66-NH₂ membrane. d) Pore size distribution and cumulative pore volume of UiO-66-SO₃H powder, UiO-66-SO₃H membrane, UiO-66-NH₂ powder and UiO-66-NH₂ membrane.

extraction has caused a certain degree of disorder or inhomogeneity in crystallite size within the framework, but the overall phase integrity is preserved.[22]

In the infrared spectrum of the UiO-66-SO$_3$H membrane, the characteristic stretching bands at 1074 cm^{-1} and 1024 cm^{-1} are S−O, and at 1253 cm^{-1} and 1167 cm^{-1} from O=S=O could be observed (Figure 3b).[23] In the infrared spectrum of the UiO-66-NH$_2$ membrane, the appearance of an absorption band at 1572 cm^{-1} indicates the reaction of -COOH with Zr^{4+}. The 1502 cm^{-1} band is from aromatic C=C.[15a] The main characteristic peak of polyacrylonitrile C≡N was seen at 2245 cm^{-1}. By comparison, the self-standing UiO-66-SO$_3$H and UiO-66-NH$_2$ membranes did not show the characteristic peak of C≡N at 2245 cm^{-1} (Figure S2b). This confirms the successful preparation of independent self-standing UiO-66-SO$_3$/-NH$_2$ membranes.

N$_2$ physisorption isotherm provided pore size distribution and specific surface area of the powders and membranes, as shown in Figure 3. The Nitrogen physisorption isotherms of all samples indicate micropores in the materials due to a sharp increase at very low relative pressures (p/p$_0$) (Figure 3c). Additionally, small mesopores were found in all materials (Figure 3d).[24] At p/p$_0$ > 0.5, the shape of the physisorption isotherms of the powders and the membranes are different. This change might be explained by the formation of the nanostructured fiber morphology and cavitation effects (effects not visible in the pore size distribution due to fitting of the adsorption of the physisorption isotherm).[25] When comparing the pore size distributions (PSD) of the powders and the membranes, the similarity is very impressive and shows that even characteristics of MOFs (high porosity and well-defined pores) could be assigned to a membrane by the used synthetic approach. The specific surface areas of the membranes, as calculated using the BET (Brunauer Emmet Teller) model with the Roquerol correction for microporous materials[26] are significantly lower (UiO-66-NH$_2$: 330 m^{2}g^{-1}, UiO-66-SO$_3$H: 84 m^{2}g^{-1}) than the specific surface areas of powder samples (UiO-66-NH$_2$: 1051 m^{2}g^{-1} UiO-66-SO$_3$H: 539 m^{2}g^{-1}). This de-

crease in the surface area could be explained by the partial change in the crystal structure or surface tension of the crystals of the UiO-66 materials, which was already observed due to the broadening of the reflections in the XRD pattern (Figure 3a).

Further, the self-supporting MOFs were studied in one pot as acid-base catalysts for a sequence of two steps, as shown in Scheme 1 (for reaction mechanism, please refer to Scheme S1). Three different one-pot reactions were studied. In each of the three reactions, the UiO-66-SO$_3$H membrane is intended to catalyze the conversion of benzaldehyde dimethyl acetal to benzaldehyde as the first step. At the same time, the UiO-66-NH$_2$ membrane is designed to catalyze the subsequent reaction of benzaldehyde with different active methylene compounds, such as malononitrile and ethyl cyanoacetate, and diethyl malonate. Benzaldehyde undergoes cyanation by malononitrile, whereas ethyl cyanoacetate and diethyl malonate undergo Knoevenagel condensation with benzaldehyde.

Before starting one-pot reactions, the acid and base-MOF membranes were tested for the individual reaction steps in different pots. The UiO-66-SO$_3$H membrane catalyzed the deacetylation reaction, as shown in Scheme 1-step a to b and Figure S3a. The molar ratio of benzaldehyde dimethyl acetal to UiO-66-SO$_3$H catalyst was 1:0.0233. The reaction was fast. About 85% of the theoretical amount of benzaldehyde was already obtained in 15 minutes. The conversion rate as determined from the initial portion of the % conversion vs. time curve (Figure S3a) till about 15 minutes was 5.69%·min^{-1}. After this, although there was a slow down in the rate of reaction, still very high conversion (>95% of benzaldehyde) was obtained in about 60 minutes (rate = 1.56%·min^{-1}). The UiO-66-NH$_2$ membrane catalyzed the reaction of benzaldehyde and malononitrile, as shown in Figure S3b. The molar ratio of benzaldehyde to UiO-66-NH$_2$ catalyst was 1:0.0565. Approximately after 30 minutes, 80% of benzaldehyde was converted to 2-benzylidene malononitrile (rate = 2.49%·min^{-1}). The benzaldehyde was almost completely converted into 2-benzylidene malononitrile when the reaction proceeded for 120 minutes.
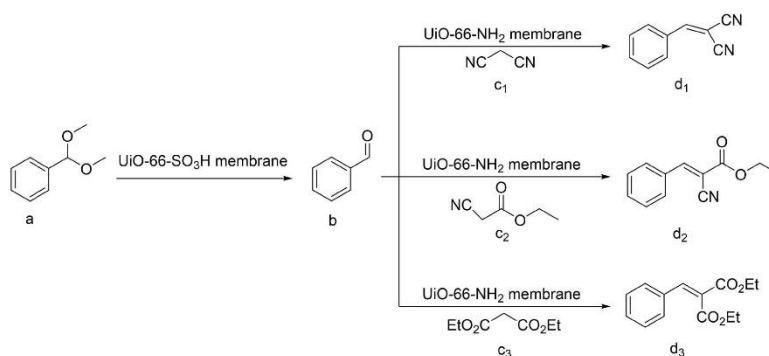
Scheme 1. Wolf-Lamb-type one-pot cascade reactions were studied in the present work.

The one-pot, two-step catalysis experiment results are shown in Figure 4a. For one-pot two steps reactions, both The UiO-66-NH$_2$ and UiO-66-SO$_3$H membranes were inserted in a reaction vessel, and all reagents were added simultaneously. Benzaldehyde dimethyl acetal (0.0025 mol), UiO-66-SO$_3$H catalyst (0.58×10^{-4} mol) and UiO-66-NH$_2$ catalyst (1.4×10^{-4} mol) were used for the reaction. The reaction was monitored for the formation of products by gas chromatography (GC). After 30 minutes, more than 80% of benzaldehyde dimethyl acetal was consumed (rate = 2.81% · min^{-1}). After a small induction period, the final product 2-benzylidene malononitrile started forming with a ~1.11% min^{-1} conversion rate until about 60 minutes. After this, although the production rate of 2-benzylidene malononitrile decreased (1.06% · min^{-1}), the reaction was still completed until very high conversions (99.9% in 4 h).

Since the first step, the UiO-66-SO$_3$H membrane catalyzed reaction, is the same, we only studied the base UiO-66-NH$_2$ catalyzed conversion of benzaldehyde in the next set of reactions to ethyl-2-cyano-3-phenyl acrylate, as shown in Figure S3c. No inhibition time was found. 70% of the benzaldehyde was converted into the product ethyl-2-cyano-3-phenyl acrylate after only 90 minutes (rate = 0.78% · min^{-1}), and about 95% conversion to the product was achieved after 7 hours of reaction. Afterward, acid UiO-66-SO$_3$H and base UiO-66-NH$_2$ membranes were used together to study the kinetics of acid-

base-catalyzed two-step reactions in one pot. The results of the one-pot, two-step reaction of the production of benzaldehyde from benzaldehyde dimethyl acetal and its further reaction with ethyl cyanoacetate are shown in Figure 4b. The results were very promising. After a slow start, the rate of reaction increased. About 88% of the product was achieved in 7 h (rate = 12.6% · h^{-1}) with almost quantitative conversion in 8 h.

Encouraged by the above results, we tested the reaction of benzaldehyde dimethyl acetal with diethyl malonate. The base UiO-66-NH$_2$ catalyzed the conversion of benzaldehyde to diethyl 2-benzylidene malonate, as shown in Figure S3d.

Unfortunately, the reaction proceeded very slowly, with only 37% of diethyl 2-benzylidene malonate produced (rate = 3.21% · h^{-1}). The results of the one-pot, two-step reaction of the production of benzaldehyde from benzaldehyde dimethyl acetal and its further reaction with diethyl malonate are shown in Figure 4c. The dimethoxybenzyl acetal was only 74% converted in this reaction, and at the end of the reaction, only 36.7% of the product was produced (rate = 2.42% · h^{-1}). We speculate that this may be because the pKa value of diethyl malonate is too high. Malononitrile (pKa = 11.1), ethyl cyanoacetate (pKa = 13.2), diethyl malonate (pKa = 16.3).[27] Due to the high pKa of diethyl malonate, deprotonation of methylene groups is extremely difficult, resulting in low product yields in one-pot reactions. There have been similar reports of this phenomenon before.[28] In addition, we investigated blank
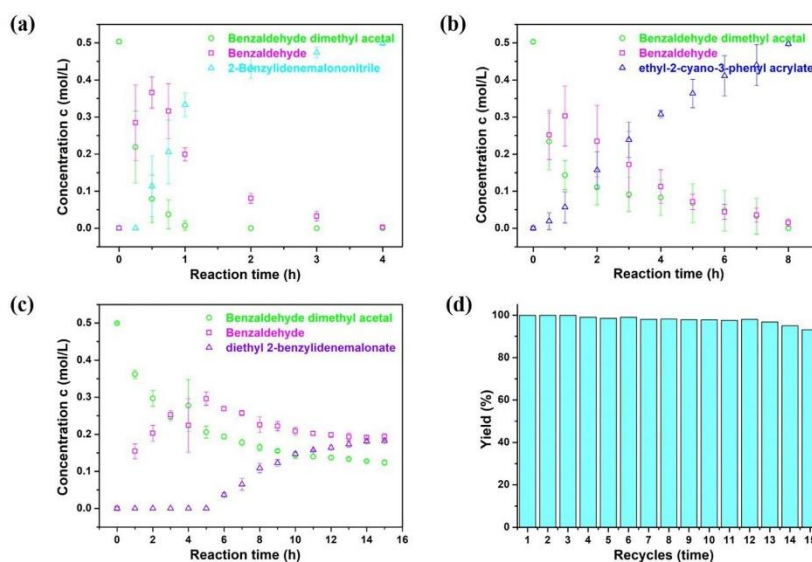
Figure 4. Acid (UiO-66-SO$_3$H membrane) and base (UiO-66-NH$_2$ membrane) catalyzed reactions: a) from benzaldehyde dimethyl acetal to 2-benzylidene malononitrile in one-pot; b) from benzaldehyde dimethyl acetal to ethyl-2-cyano-3-phenyl acrylate in one-pot; c) from benzaldehyde dimethyl acetal to diethyl 2-benzylidene malonate in one-pot. d) Catalyst recycling studies. Reaction conditions: (2.5 mmol) dimethoxybenzyl acetal, (3 mmol) malononitrile, 50 mg UiO-66-SO$_3$H membrane and 50 mg UiO-66-NH$_2$ membrane, solvent: DMF (5 mL), 80 °C.

experiments (without a catalyst) of the tandem reaction of benzaldehyde dimethyl acetal with different active methylene compounds (Table S4). Without the catalyst, the products 2-benzylidene malononitrile, ethyl-2-cyano-3-phenyl acrylate, and diethyl 2-benzylidene malonate were not detected in the one-pot two-step reactions. It indicated that the addition of the catalyst played an important role in the reaction process.

Next, we tested the recycling ability of the UiO-66-SO$_3$H/-NH$_2$ membranes for the one-pot, two-step reaction of benzaldehyde dimethyl acetal with malononitrile. After the reaction is completed, the catalyst membranes only need to be simply taken out, washed with acetone and methanol, and dried in a vacuum oven at 80 °C. After this, it was directly used for the next catalytical cycles under the same reaction conditions. The results are shown in Figure 4d. When the catalyst membranes are reused 15 times, 2-benzylidene malononitrile can still be obtained as high as 93.1%. We carried out XRD characterization on the used catalyst membranes, as shown in Figure S4a, by comparison, there is no obvious difference between the used catalyst membranes and the fresh catalyst membranes, indicating that the catalyst membranes have good chemical resistance. In addition, we conducted Fourier-transform infrared (FT-IR) tests on the used catalyst membranes, as shown in Figure S4b, and the catalyst membranes can still maintain their integrity after 15 cycles of use. The performance of self-standing MOF membranes in one-pot reactions is compared with bifunctional acid-base MOF powders reported in the literature (Table S5). It can be seen that the self-supporting MOF membranes (UiO-66-SO$_3$H/-NH$_2$ membranes) exhibit excellent catalytic activity and efficient recycling performance. As there was no change in the structure and physical integrity of the MOF membranes, they are expected to work for many more cycles, not limited to the 15 cycles as tested in this work.

Conclusions

In conclusion, we present highly stable, easy-to-handle, reusable, efficient functional MOF self-standing membranes (UiO-66-SO$_3$H and UiO-66-NH$_2$ membranes) for sustainable use as Wolf-Lamb-type (acid-base) catalysts in one-pot cascade reactions in a tea-bag-type concept. First, a simple procedure for making UiO-66-SO$_3$H and UiO-66-NH$_2$ membranes based on in-situ growth of respective MOFs on seeded template polymer fibers in a non-woven is established. The membranes were characterized using routine analytical methods for porosity, morphology, and functionality and showed morphologically made up of hollow fibers. The membranes efficiently catalyzed both steps of a cascade one-pot reaction, i.e., deacetylation of benzaldehyde dimethyl acetal to benzaldehyde and reaction of active methylene compounds malononitrile and ethyl cyanoacetate with benzaldehyde. A high overall yield of the final products could be obtained. MOF membranes with -NH$_2$ base groups are limited as catalysts for the reaction of benzaldehyde with active methylene compounds having high pKa, such as diethyl malonate.

The membranes are easy to use and, after completion of the reaction, can be pulled out, washed, and reused without any significant drop in reaction efficiency, even after 15 cycles. This work provides an important step forward in preparing and using MOF membranes of macroscopic dimensions as sustainable catalysts.

Experimental Section

Materials

Zirconium(IV) chloride (ZrCl$_4$, Alfa Aesar company, 99.5%), 2-amino-benzenedicarboxylic acid (BDC-NH$_2$, Alfa Aesar company, 99%), 2-sulfobenzenedicarboxylic acid monosodium salt (BDC-SO$_3$Na, Sigma Aldrich company), polyacrylonitrile (Mw = 80,000, Carl Roth), benzaldehyde dimethyl acetal (Alfa Aesar company, 99%), benzaldehyde (Alfa Aesar company, 99%), ethyl cyanoformate (Sigma Aldrich company, > 99%), malononitrile (Alfa Aesar company, 99.5 + %), diethyl malonate (Acros Organics company, > 99%), Dodecane (Alfa Aesar company, 99%), acetic acid (Fisher Chemical Company, 99.7%), N, N-dimethylformamide (Fisher Chemical company, 99.5%) were purchased as stated.

Preparation of UiO-66-SO$_3$H particles and UiO-66-NH$_2$ particles

The solvothermal reaction was used to synthesize UiO-66-SO$_3$H particles. 0.233 g ZrCl$_4$ and 0.268 g 2-sulfobenzenedicarboxylic acid monosodium salt (BDC-SO$_3$Na) dissolved in 10 mL DI water and 1 mL acetic acid. Afterward, the mixture was transferred to a 50 mL Teflon-lined autoclave and reacted in an oven at 120 °C for 24 h. After cooling to room temperature, the white powder could be obtained by centrifugation and washing with 20 mL methanol 3–4 times, and finally dried at 100 °C overnight in an oven. The UiO-66-NH$_2$ particles are also synthesized by the solvothermal method. Just use 2-aminobenzenedicarboxylic acid instead of 2-sulfobenzenedicarboxylic acid monosodium salt (BDC-SO$_3$Na). Other conditions are the same as synthetic UiO-66-SO$_3$H particles.

Preparation of UiO-66-SO$_3$H membrane and UiO-66-NH$_2$ membrane

First, 0.33 g of ZrCl$_4$ and 1.0 g PAN were stirred in 5.6 g of DMF in 10 mL glass bottle for 3 h. The solution was used for electro-spinning with an applied voltage 18.0 KV, flow rate 1.5 mL·h^{-1}, and a 20.0 cm distance between the electrodes. This results in a PAN/ZrCl$_4$ fiber membrane. Next, 0.115 g ZrCl$_4$, and 0.134 g 2-sulfobenzenedicarboxylic acid monosodium salt (BDC-SO$_3$Na) dissolved in 10 mL DI water and 1 mL acetic acid in 50 mL Teflon-lined autoclave. And then, 25 mg PAN/ZrCl$_4$ fiber membrane was added. The reaction was carried out in an oven at 120 °C for one day resulting in PAN/UiO-66-SO$_3$H fiber membranes. Finally, the PAN was removed from the membranes by Soxhlet extraction at 165 °C for one day with DMF. The resulting UiO-66-SO$_3$H fiber membrane free of PAN were dried. The preparation of the UiO-66-NH$_2$ membrane is the same as the UiO-66-SO$_3$H fiber membrane. Use 2-aminobenzenedicarboxylic acid (BDC-NH$_2$) instead of 2-sulfobenzenedicarboxylic acid monosodium salt (BDC-SO$_3$Na).

The amount of acid and base groups were calculated based on the elemental analysis.

For UiO-66-SO$_3$H membrane:

Elemental analysis: C 27.28%, H 3.63%, S 3.73%.

The amount of $S = 3.73/(32*100) = 0.0011625$ mol/g of UiO-66-SO$_3$H membrane = amount of acid group = 0.58×10^{-4} mol/50 mg membrane.

For UiO-66-NH$_2$ membrane:

Elemental analysis: C 34.26%, H 4.14%, N 3.96%.

The amount of $N = 3.96/(14*100) = 0.002828$ mol/g of UiO-66-NH$_2$ membrane =

the amount of base groups (−NH$_2$) = 1.41×10^{-4} mol/50 mg membrane.

Catalytic experiment

One-step acid-catalyzed reaction

Before catalyzing the reaction, the catalyst was activated in an oven at 353 K for 12 h to remove the solvent molecules. The reaction is carried out in the liquid phase under air. Typically, 2.5 mmol benzaldehyde dimethyl acetal, 5 mmol distilled water, 50 mg UiO-66-SO$_3$H membrane, 0.75 mmol dodecane (as an internal standard), and 5 mL DMF were taken in a 25 mL glass reactor vial. The reaction mixture was then heated to 80 °C with stirring at 200 rpm. At regular intervals, 10 μL of the reaction mixture was taken using a pipette and the progress of the reaction was monitored by the GC-FID system (GC-2010 Plus, Shimadzu). After the reaction, the membrane is directly taken out of the reaction medium, washed with acetone (3×20 mL) and methanol (3×20 mL), dried at 80 °C in a vacuum oven, and reused for recycle runs.

One-step base-catalyzed reaction

Before catalyzing the reaction, the catalyst was activated in an oven at 353 K for 12 h to remove the solvent molecules. The reaction is carried out in the liquid phase under air. 2.5 mmol benzaldehyde, 3 mmol active methylene compounds, 50 mg UiO-66-NH$_2$ membrane, 0.75 mmol dodecane (as an internal standard), and 5 mL DMF were taken in a 25 mL glass reactor vial. The reaction mixture was then heated to 80 °C with stirring at 200 rpm. At regular intervals, 10 μL of the reaction mixture was taken using a pipette and the progress of the reaction was monitored by GC-FID system (GC-2010 Plus, Shimadzu). After the reaction, the membrane is directly taken out of the reaction medium, washed with acetone (3×20 mL) and methanol (3×20 mL), dried at 80 °C in a vacuum oven, and reused for recycle runs.

One-pot two-step acid-base catalyzed reaction

Before catalyzing the reaction, the catalyst was activated in an oven at 353 K for 12 h to remove the solvent molecules. The reaction is carried out in the liquid phase under air. Typically, 2.5 mmol benzaldehyde dimethyl acetal, 5 mmol distilled water, 3 mmol active methylene compounds, 50 mg UiO-66-SO$_3$H membrane and 50 mg UiO-66-NH$_2$ membrane, 0.75 mmol dodecane (as an internal standard), and 5 mL DMF were taken in a 25 mL glass reactor vial. The reaction mixture was then heated to 80 °C with stirring at 200 rpm. At regular intervals, 10 μL of the reaction mixture was taken using a pipette and the progress of the reaction was monitored by GC-FID system (GC-2010 Plus, Shimadzu). After the reaction, the membranes are directly taken out of the reaction medium, washed with acetone (3×20 mL) and methanol (3× 20 mL), dried at 80 °C in a vacuum oven, and reused for recycle runs.

Conflict of Interest

The authors declare no conflict of interest.

Data Availability Statement

The data that support the findings of this study are available in the supplementary material of this article.

[1] a) H. Demir, G. O. Aksu, H. C. Gulbalkan, S. Keskin, *Carbon Capture Science & Technology* **2022**, *2*, 100026; Technology **2022**, *2*, 100026; b) Y. Deng, Yanni. Wu, G. Chen, X. Zheng, M. Daia, C. Peng, *Chem. Eng. J.* **2021**, *405*, 127004.

[2] O. M. Yaghi, G. Li, H. Li, *Nature* **1995**, *378(6558)*, 703.

[3] a) Y. Y. Liu, E. P. Hu, E. A. Khan, Z. P. Lai, *J. Membr. Sci.* **2010**, *353*, 36; b) A. Huang, H. Bux, F. Steinbach, J. Caro, *Angew. Chem.* **2010**, *122*, 5078.

[4] X. Qin, Y. X. Sun, N. X. Wang, Y. B. Xie, J. R. Li, *Chem. Ind. Eng.* **2017**, *36*, 1306.

[5] L. Fan, M. Xue, Z. Kang, S. Qiu, *J. Mater. Chem.* **2012**, *22*, 25272.

[6] T. Toyao, M. Saito, Y. Horiuchi, M. Matsuoka, *Cata. Sci. Technol.* **2014**, *4*, 625.

[7] a) Y. Huang, A. M. Walji, C. H. Larsen, D. W. C. MacMillan, *J. Am. Chem. Soc.* **2005**, *127*, 43, 15051; b) J. Barluenga, F. Rodríguez, F. J. Fananµs, *Chem. Asian J.* **2009**, *4*, 1036; c) P. F. Xu, W. Wang, in *Catalytic cascade reactions*, John Wiley & Sons, **2013**; d) A. Behr, A. J. Vorholt, K. A. Ostrowski, T. Seidensticker, *Green Chem.* **2014**, *16*, 982; e) Q. J. Liang, Y. H. Xu, T. P. Loh, *Org. Chem. Front.* **2018**, *5*, 2765; f) H. Pellissier, *Adv. Synth. Catal.* **2020**, *362*, 2289.

[8] a) L. F. Tietze, *Chem. Rev.* **1996**, *96*, 115; b) I. R. Baxendale, S. V. Ley, C. Piutti, *Angew. Chem.* **2002**, *114*, Nr. 12; c) M. J. Climent, A. Corma, S. Iborra, *ChemSusChem* **2009**, *2*, 500; d) C. Grondal, M. Jeanty, D. Enders, *Nat. Chem.* **2010**, *2*, 167; e) A. Belluati, I. Craciun, J. Liu, C. G. Palivan, *Biomacromolecules* **2018**, *19*, 4023; f) Y. Liu, J. A. Izzo, D. McLeod, S. Ričko, E. B. Svenningsen, T. B. Poulsen, K. A. Jørgensen, *J. Am. Chem. Soc.* **2021**, *143*, 8208; g) W. Xu, L. Jiao, Y. Wu, L. Hu, W. Gu, C. Zhu, *Adv. Mater.* **2021**, *33*, 2005172.

[9] B. J. Cohen, M. A. Kraus, A. Patchornik, *J. Am. Chem. Soc.* **1981**, *103*, 7621.

[10] a) N. T. S. Phan, C. S. Gill, J. V. Nguyen, Z. J. Zhang, C. W. Jones, *Angew. Chem. Int. Ed.* **2006**, *45*, 2209; b) J. P. H. Li, A. A. Adesina, E. M. Kennedy, M. Stockenhuber, *Phys. Chem. Chem. Phys.* **2017**, *19*, 26630; c) X. Yuan, Z. Wang, Q. Zhang, J. Luo, *RSC Adv.* **2019**, *9*, 23614.

[11] a) K. Motokura, N. Fujita, K. Mori, T. Mizugaki, K. Ebitani, K. Kaneda, *J. Am. Chem. Soc.* **2005**, *127*, 9674; b) A. Erigoni, M. C. Hernández-Soto, F. Rey, C. Segarra, U. Díaz, *Catal. Today* **2020**, *345*, 227.

[12] a) T. Ge, Z. Hua, Y. Zhu, Y. Song, G. Tao, X. Zhou, L. Chen, W. Ren, H. Yao, J. Shi, *RSC Adv.* **2014**, *4*, 64871; b) K. A. Almeida, D. Cardoso, *Catal. Today* **2013**, *213*, 122; c) A. Kawano, T. Moteki, M. Ogura, *Microporous Mesoporous Mater.* **2020**, *299*, 110104.

[13] a) M. Mu, X. Yan, Y. Li, L. Chen, *J. Nanopart. Res.* **2017**, *19*, 148; b) J. H. Zhao, Y. Yang, J. X. Che, J. Zuo, X. H. Li, Y. Z. Hu, X. W. Dong, L. Gao, X. Y. Liu, *Chem. Eur. J.* **2018**, *24*, 9903; c) S. Mistry, A. Sarkar, S. Natarajan, *Cryst. Growth Des.* **2019**, *19*, 747; d) T. Zurrer, K. Wong, J. Horlyck, E. C.

Lovell, J. Wright, N. M. Bedford, Z. Han, K. Liang, J. Scott, R. Amal, *Adv. Funct. Mater.* **2021**, *31*, 2007624.

[14] a) Y. B. Huang, J. Liang, X. S. Wang, R. Cao, *Chem. Soc. Rev.* **2017**, *46*, 126; b) A. Dhakshinamoorthy, Z. Li, H. Garcia, *Chem. Soc. Rev.* **2018**, *47*, 8134; c) X. Zhang, J. Sun, G. Wei, Z. Liu, H. Yang, K. Wang, H. Fei, *Angew. Chem. Int. Ed.* **2019**, *58*, 2844; d) S. Yuan, J. Zhang, L. Hu, J. Li, S. Li, Y. Gao, Q. Zhang, L. Gu, W. Yang, X. Feng, B. Wang, *Angew. Chem.* **2021**, *133*, 21853; e) W. Yang, X. Liu, X. Chen, Y. Cao, S. Cui, L. Jiao, C. Wu, C. Chen, D. Fu, I. D. Gates, Z. Cao, H. Jiang, *Adv. Mater.* **2022**, 2110123.

[15] a) P. Rani, R. Srivastava, *J. Colloid Interface Sci.* **2019**, *557*, 144; b) Y. Hu, J. Zhang, H. Huo, Z. Wang, X. Xu, Y. Yang, K. Lin, R. Fan, *Catal. Sci. Technol.* **2020**, *10*, 315; c) Y. R. Lee, X. H. Do, S. S. Hwang, K. Y. Baek, *Catal. Today* **2021**, *359*, 124.

[16] Q. Dang, H. Huang, L. Li, X. Lyu, S. Zhong, Y. Yu, D. Xu, *Chem. Mater.* **2021**, *33*, 5690.

[17] J. Liu, T. A. Goetjen, Q. Wang, J. G. Knapp, M. C. Wasson, Y. Yang, Z. H. Syed, M. Delferro, J. M. Notestein, O. K. Farha, J. T. Hupp, *Chem. Soc. Rev.* **2022**, *51*, 1045.

[18] F. Mitschang, H. Schmalz, S. Agarwal, A. Greiner, *Angew. Chem. Int. Ed.* **2014**, *53*, 4972.

[19] M. O. Pretscher, S. Gekle, S. Agarwal, *Macromol. Rapid Commun.* **2019**, *40*, 1900148.

[20] J. H. Cavka, S. Jakobsen, U. Olsbye, N. Guillou, C. Lamberti, S. Bordiga, K. P. Lillerud, *J. Am. Chem. Soc.* **2008**, *130*, 13850.

[21] M. J. Katz, Z. J. Brown, Y. J. Colón, P. W. Siu, K. A. Scheidt, R. Q. Snurr, J. T. Hupp, O. K. Farha, *Chem. Commun.* **2013**, *49*, 9449.

[22] Y. Yang, H. F. Yao, F. G. Xi, E. Q. Gao, *J. Mol. Catal. A* **2014**, *390*, 198.

[23] R. G. Vaghei, D. Azarifar, S. Daliran, A. R. Oveisi, *RSC Adv.* **2016**, *6*, 29182.

[24] M. Thommes, K. Kaneko, A. V. Neimark, J. P. Olivier, F. Rodriguez-Reinoso, J. Rouquerol, K. S. W. Sing, *Pure Appl. Chem.* **2015**, *87*, 1051.

[25] C. Schlumberger, M. Thommes, *Adv. Mater. Interfaces* **2021**, *8*, 2002181.

[26] J. Rouquerol, F. Rouquerol, P. Llewellyn, G. Maurin, K. S. W. Sing, Academic press, **2013**.

[27] W. S. Matthews, J. E. Bares, J. E. Bartmess, F. G. Bordwell, F. J. Cornforth, G. E. Drucker, Z. Margolin, R. J. McCallum, G. J. McCollum, N. R. Vanier, *J. Am. Chem. Soc.* **1975**, *97*, 7006.

[28] a) D. Wang, Z. Li, *Catal. Sci. Technol.* **2015**, *5*, 1623; b) H. Liu, F. G. Xi, W. Sun, N. N. Yang, E. Q. Gao, *Inorg. Chem.* **2016**, *55*, 12, 5753.

ChemCatChem

Supporting Information

Template-assisted Preparation of Self-standing 2D-MOF Membranes for Application in Cascade Reactions

Yingying Du, Chenhui Ding, Jana Timm, Roland Marschall, and Seema Agarwal*

WILEY-VCH

Characterization

The Fourier transform infrared spectra (FTIR, 500-4000 cm^{-1}) were obtained using a spectrometer (Digilab Excalibur FTS-3000).

Scanning electron microscopy (SEM): The surface morphology was observed with a Zeiss LEO 1530, operating at an acceleration voltage of 3 kV employing an Everhart-Thornley secondary electron detector. Before imaging, the samples were sputtered with a thin platinum layer of 2 nm (Sputter Coater 208HR, Cressington).

The Xray diffraction (XRD, Cu Kα, λ = 1.540598 Å) patterns were recorded on a Bragg-Brentanotype diffractometer (XPERT-PRO, PANalytical B.V.), and each XRD pattern was scanned over a range of 2θ = 2° to 40° at a rate of 0.5° min^{-1}.

N$_2$ adsorption/desorption isotherms were measured on Quantachrome iQ and kept at 77 K by a liquid nitrogen bath. The data were analyzed using the ASIQ v 3.0 software package.

Gas Chromatography (GC): GC measurements were performed on a GC-FID system (GC-2010 Plus, Shimadzu), using nitrogen as a carrier gas. An amount of 10 µL of the reaction mixture was dissolved in 1 mL acetonitrile. 1 µL of this solution was injected with a split ratio of 1:50 and measured from 50 °C (2 min hold) up to 300 °C at a heating rate of 15K min^{-1}.

1

WILEY-VCH

Supporting Figures and Tables
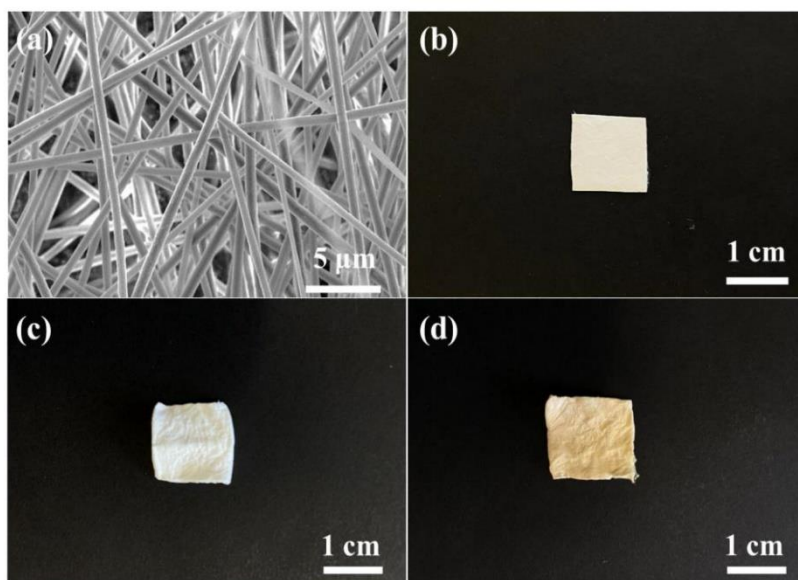
Figure S1. SEM images of a) PAN/ZrCl$_4$ membrane. Photographs of b) PAN/ZrCl$_4$ membrane, c) UiO-66-SO$_3$H membrane and d) UiO-66-NH$_2$ membrane.

2
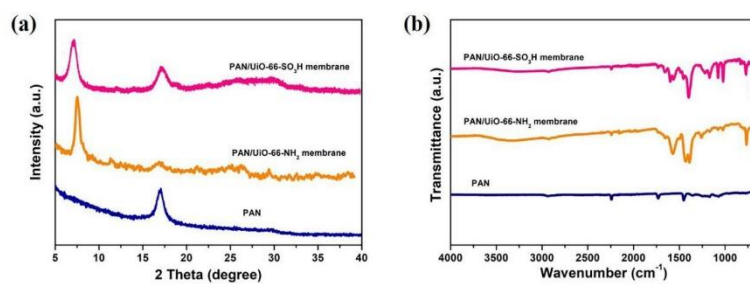
Figure S2. a) XRD patterns of PAN, PAN/UiO-66-NH$_2$ membrane and PAN/UiO-66-SO$_3$H membrane. b) FT-IR spectra of PAN, PAN/UiO-66-NH$_2$ membrane and PAN/UiO-66-SO$_3$H membrane.

3
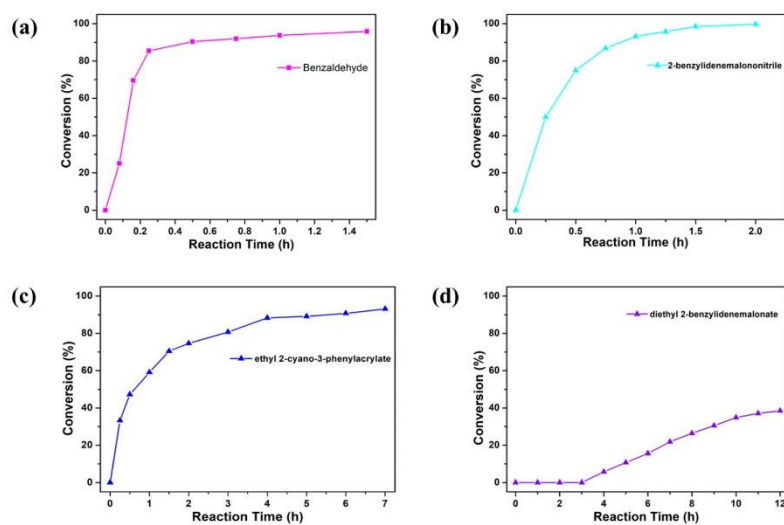
Figure S3. a) UiO-66-SO$_3$H membrane catalyzed reaction from benzaldehyde dimethyl acetal to benzaldehyde. b) UiO-66-NH$_2$ membrane catalyzed reaction of benzaldehyde to 2-benzylidenemalononitrile. c) UiO-66-NH$_2$ membrane catalyzed reaction of benzaldehyde to ethyl-2-cyano-3-phenyl acrylate. d) UiO-66-NH$_2$ membrane catalyzed reaction of benzaldehyde to diethyl 2-benzylidene malonate.

4

WILEY-VCH
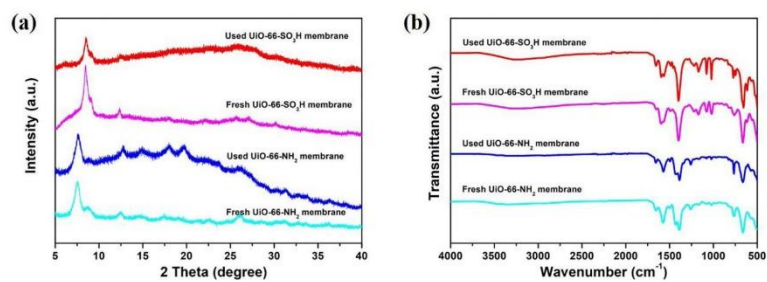
Figure S4. a) XRD patterns of fresh and used UiO-66-SO$_3$H/-NH$_2$ membranes. b) FT-IR

spectra of the fresh and used UiO-66-SO$_3$H/-NH$_2$ membranes.

5

WILEY-VCH

Table S1. The kinetic experiments for the conversion of benzaldehyde dimethyl acetal to 2-benzylidenemalononitrile in one-pot.
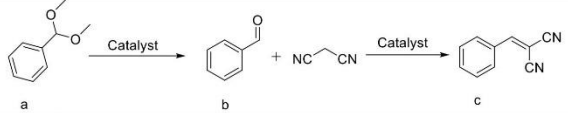
Reaction time (h)	Concentration of a (mol/L)	Concentration of b (mol/L)	Concentration of c (mol/L)
0	0.504±0.006	-	-
0.5	0.079±0.064	0.366±0.043	0.113±0.082
0.75	0.037±0.039	0.316±0.074	0.206±0.086
1	0.007±0.012	0.199±0.018	0.333±0.033
2	-	0.080±0.013	0.433±0.029
3	-	0.032±0.013	0.47±0.0148
4	-	0.002±0.004	0.499±0.006

6

WILEY-VCH

Table S2. The kinetic experiments for the conversion of benzaldehyde dimethyl acetal to ethyl-2-cyano-3-phenyl acrylate in one-pot.
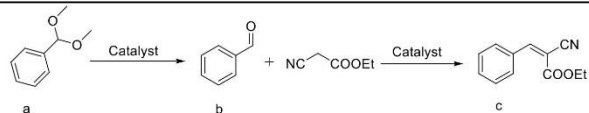
Reaction time (h)	Concentration of a (mol/L)	Concentration of b (mol/L)	Concentration of c (mol/L)
0	0.503±0.005	0	-
0.5	0.234±0.076	0.252±0.066	0.019±0.023
1	0.143±0.039	0.303±0.081	0.057±0.042
2	0.111±0.046	0.235±0.096	0.157±0.050
3	0.091±0.046	0.172±0.089	0.239±0.047
4	0.082±0.048	0.112±0.046	0.307±0.010
5	0.068±0.052	0.071±0.021	0.36±0.038
6	0.048±0.054	0.044±0.020	0.411±0.054
7	0.033±0.048	0.036±0.019	0.440±0.055
8	-	0.015±0.009	0.497±0.005

7

135

WILEY-VCH

Table S3. The kinetic experiments for the conversion of benzaldehyde dimethyl acetal to to diethyl 2-benzylidene malonate in one-pot.

Reaction time (h)	Concentration of a (mol/L)	Concentration of b (mol/L)	Concentration of c (mol/L)
0	0.499±0.012	0	-
1	0.362±0.012	0.154±0.020	-
2	0.297±0.022	0.203±0.022	-
3	0.248±0.012	0.253±0.012	-
4	0.278±0.070	0.224±0.072	-
5	0.206±0.016	0.296±0.018	-
6	0.194±0.006	0.269±0.005	0.037±0.006
7	0.178±0.010	0.257±0.007	0.065±0.016
8	0.165±0.009	0.226±0.021	0.109±0.013
9	0.155±0.004	0.222±0.013	0.123±0.009
10	0.144±0.010	0.209±0.011	0.148±0.004
11	0.140±0.005	0.202±0.005	0.157±0.002
12	0.137±0.005	0.199±0.007	0.164±0.007
13	0.134±0.003	0.193±0.010	0.173±0.008
14	0.128±0.002	0.193±0.00	0.182±0.003
15	0.124±0.007	0.193±0.008	0.182±0.002

8

136

WILEY-VCH

Table S4. The blank experiment for the reaction of benzaldehyde dimethyl acetal with different active methylene compounds (without catalyst) [a].

entry	R_1	R_2	Product (c)	conv. of a (%)	yield of c (%)
1	CN	CN		Trace	0
2	CN	COOEt		Trace	0
3	COOEt	COOEt		0	0

[a] Reaction condition: 1.5 mmol benzaldehyde dimethyl acetal, 3 mmol distilled water, 1.8 mmol methylene compounds, 0.15 mmol dodecane (as an internal standard), and 3 mL DMF to a 10mL glass reactor vial. The reaction mixture was then heated to 80 °C with stirring at 200 rpm.

9

137

WILEY-VCH

Table S5. One-pot acid-base cascade reactions: comparison of MOF particles with MOF membranes as catalysts.
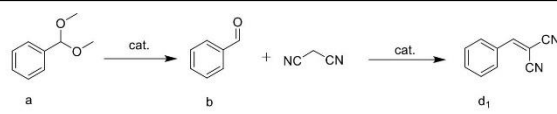
entry	catalyst	conv. of a (%)	yield of d_1 (%)	Recycle times	Ref.
1	UiO-66-SO$_3$H FM [a] UiO-66-NH$_2$ FM	99.9	99.9	15	this work
2	MIL-101-AB-0.26[b]	92.0	91.0	3	1
3	MIL-101(Al/Fe)-NH$_2$ [c]	100	99.8	5	2
4	MIL-101(Cr)@CS[d] [MIL-101(Cr)/CS=2.86]	99.0	99.0	5	3
5	Yb-BDC-NH$_2$[e]	97.0	97.0	4	4
6	ZIF8-A61-SO$_3$H[f]	100.0	98.0	5	5

Reaction conditions: [a] Benzaldehyde dimethyl acetal (1 mmol), malononitrile (1.2 mmol), distilled water (108 µL), 50 mg UiO-66-SO$_3$H membrane, 50 mg UiO-66-NH$_2$ membrane, DMF (2 mL), 80 ∘C. [b] Benzaldehyde dimethyl acetal (1 mmol), malononitrile (2 mmol), DMF 2 mL, catalyst 0.04 mmol, 363K. [c] Benzaldehyde dimethyl acetal (1.0 mmol), malononitrile (1.5 mmol), toluene (3 mL), catalyst (20 mg). [d] Benzaldehyde dimethyl acetal (2 mmol), malononitrile (2.1 mmol), acetonitrile (2 mL), distilled water (50 µL), and catalyst (50 mg); 80 °C; reaction time 12 h. [e] Benzaldehyde dimethyl acetal (2.0 mmol), malononitrile (2.1 mmol) and DMSO-d6 (2 mL), catalyst (100 mg), 50 °C and 24 h. [f] Benzaldehyde dimethyl acetal (1 mmol), malononitrile (5 mmol),1,4-dioxane (4 ml), catalyst (100 mg).

10

WILEY-VCH

Scheme S1. Mechanism of acid-base reaction catalyzed by catalyst membrane.
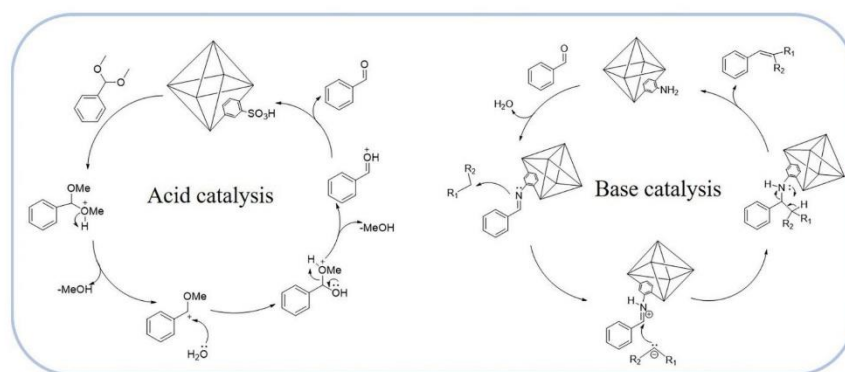
References

[1] H. Liu, F. G. Xi, W Sun, N. N. Yang, E. Q. Gao, *Inorg. Chem.* **2016**, 55, 12, 5753.

[2] Y. Hu, J. Zhang, H. Huo, Z. Wang, X. Xu, Y. Yang, K. Lin, R. Fan, *Catal. Sci. Technol.* **2020**, 10, 315.

[3] Z. S. Zhao, Y. Zhang, T. Fang, Z. B. Han, F. S. Liang, *ACS Appl. Nano Mater.* **2020**, 3, 6316.

[4] Y. Zhang, Y. Wang, L. Liu, N. Wei, M. L. Gao, D. Zhao, Z. B. Han, *Inorg. Chem.* **2018**, 57, 4, 2193.

[5] Y. R. Lee, X. H. Do, S. S. Hwang, K. Y. Baek, *Catal. Today.* **2021**, 359, 124.

11

4.3 Sustainable Hierarchically Porous Reusable Metal-Organic Framework Sponge as a Heterogeneous Catalyst and Catalytic Filter for Degradation of Organic Dyes

Sustainable Hierarchically Porous Reusable Metal–Organic Framework Sponge as a Heterogeneous Catalyst and Catalytic Filter for Degradation of Organic Dyes

Yingying Du, Chenhui Ding, and Seema Agarwal*

Advanced oxidation processes based on sulfate radical are considered one of the most promising wastewater treatment technologies currently. Among heterogeneous catalysts, cobalt metal–organic framework (MOF) has been widely reported. However, the inherent powder form of MOF hinders its practical application and reusability. Therefore, innovative methods to increase the loading capacity and the accessibility of MOF active sites in monolithic materials are required. Therefore, a simple and scalable method of fabricating a stable, hierarchical porous zeolitic imidazolate framework (ZIF-67) 3D sponge by growing MOF on a short electrospun fiber network is shown. The sponge can efficiently activate peroxymonosulfate and rapidly degrade an exemplary organic dye (Rhodamine B) with a degradation efficiency of 100%. The resulting multilevel, hierarchical porous structure is beneficial to the mass transfer of reagents making the catalytic process efficient. This also enables the use of the ZIF-67 as an efficient catalytic filter for continuous removal of dye. The sponge can be recycled and reused for several cycles due to its robustness without loss in efficiency. The proposed research strategy provides a new way to design MOF 3D monolithic materials.

1. Introduction

Water resources are an integral part of human development and life. However, organic dye discharges from industries such as textiles, cosmetics, papermaking, and leather pollute water resources every year.[1] Organic dyes are generally toxic and highly stable and are difficult to degrade and handle.[2] The consumption of dye-contaminated water can lead to serious health issues.[3] Therefore, the wastewater treatment of organic dyes has always been an important issue that researchers have paid close attention. At present, the technical means commonly used in wastewater treatment include adsorption,[4] filtration,[5] membrane separation,[6] coagulation,[7] and so on. However, these methods only transfer the dye to the material, and there are still secondary pollution problems, which greatly increase the operation and time costs of the treatment. Therefore, other cost-effective wastewater treatment technologies should be further developed.

The advanced oxidation process is to oxidize active species to decompose organic dyes into low-toxic small molecules or water and carbon dioxide through redox reactions.[8] It is one of the most promising wastewater treatment technologies at present. Among them, sulfate radical based advanced oxidation processes (SR-AOPs) have attracted extensive attention of researchers due to the wide source of sulfate radical, high oxidation potential (2.5–3.1 V), wide pH value working range (3.0–9.0), and excellent reaction selectivity.[9] Sulfate radicals are usually produced by activating peroxomonosulfate (PMS) and peroxydisulfate through photolysis, ultrasound, transition metal ions, and their metal oxides.[10] However, the traditional activation method still has problems such as insufficient catalytic performance and secondary contamination (difficult recovery of catalyst).[11] Therefore, the development of materials with immobilized catalysts/catalytic species with high activity and stability is the development trend of SR-AOPs.

Metal–organic frameworks (MOFs) are emerging porous materials, which are widely used in catalysis, separation, sensing, and other fields due to their high specific surface area, ordered porous structure, and multifunctional active sites.[12] In particular, cobalt (Co)-based zeolite-like imidazole-based organic frameworks (ZIFs) with Co as the metal ion and imidazolium salt as the organic ligand have been reported for the degradation of organic dyes by activating persulfate.[13] However, due to the inherent difficulty of processing and recycling of ZIFs in the form of powder nanocrystals, their application in practical use is hindered.[14] In order to solve this problem, researchers usually immobilize ZIF particles on supporting carriers, such as films,[15] foams,[16] resins,[17] and so on to obtain ZIF composites with higher practicability and functionality. However, there are still problems such as insufficient loading

Y. Du, C. Ding, S. Agarwal
Macromolecular Chemistry and Bavarian Polymer Institute
University of Bayreuth
Universitätsstrasse 30, 95440 Bayreuth, Germany
E-mail: agarwal@uni-bayreuth.de

of ZIF and poor availability of active sites of ZIF in composites.[14a,18]

In this work, we first show a procedure of loading ZIF-67 in large amounts (as large as 72%) on a 3D porous fibrous network skeleton of polyimide (PI) electrospun short fibers. In our previous works, we established a method of making PI porous frameworks (sponges) using short electrospun fibers and showed its use as pressure sensors, heat insulation, etc., and skeleton for the growth of covalent organic framework.[19] The present method allows in situ growth of ZIF-67 onto the surface of PI network fibers of the 3D skeleton and thereby bringing ZIF-67 in the shape of a 3D sponge with hierarchical porosity and mechanical stability. The hierarchically porous network facilitates the transport of reagents required for the efficient degradation of organic dyes and at the same time, it exposes a plenty of active sites (ZIF-67) for degradation reaction. After establishing the preparation procedure, the practicability of polymer–MOF sponge as a reusable catalyst to activate PMS for the degradation of organic dye Rhodamine B (Rh B) under different conditions was shown. The unique hierarchical porous structure of the sponge leads to a good water flux and therefore, its utility as a filter for continuous degradation of organic dye is also shown by assembling a simple filter device. This work provides a new avenue for applying MOF-based composites to practical wastewater treatment technologies as efficient reusable heterogeneous materials and filters.

2. Results and Discussion

The preparation process of PI/PAN@ZIF-67 sponge is shown in **Figure 1**. First, PI short fibers, polyacrylonitrile (PAN), and $Co(NO_3)_2 \cdot 6H_2O$ are dispersed in dimethyl sulfoxide (DMSO), and the PI/PAN/Co^{2+} sponge with honeycomb frame structure is obtained by freeze-drying. PI short fibers were prepared by mechanical cutting of a PI nonwoven prepared by electrospinning as described in our previous work.[20] PI fibers had an average diameter $d = 521 \pm 143.0$ nm and length $L = 77 \pm 33$ μm, respectively. Fifty short fibers were randomly selected in scanning electron microscope (SEM) images for calculating the average diameter and length using ImageJ software (Figure S1, Supporting Information). PAN as a binder ensures the stability of PI short fibers in the 3D structure and makes Co^{2+} uniformly dispersed on the surface of PI short fibers, providing a great deal of sites for the growth of ZIF-67. Then the PI/PAN/Co^{2+} sponge was put into the precursor solution of ZIF-67 (aqueous solution of Co nitrate hexahydrate and 2-methylimidazole), and ZIF-67

grew in situ on the surface of the PI fiber to obtain a sponge in which ZIF-67 was grown on the surface of fibers making network porous PI/PAN template sponge. The final sponge is designated as PI/PAN@ZIF-67. It is worth noting that stirring is necessary during the preparation of PI/PAN@ZIF-67 sponge. If there is no stirring, the nucleation of ZIF-67 is slow, and it is easy to generate larger sized particles, which leads to nonadherence and easy detachment from the sponge surface giving defects and low ZIF-67 loading (Figure S2, Supporting Information). The loading of ZIF-67 was determined according to the mass change of PI/PAN/Co^{2+} sponge after the growth of ZIF-67. The loading of ZIF-67 could be as high as 72%.

The morphology of the samples was analyzed by SEM. **Figure 2**a shows the optical picture of PI/PAN@Co^{2+} sponge. A honeycomb structure with uniform macroscopic and microscopic pores was visible (Figure 2b). The wall of the sponge is composed of PI short fibers interwoven with each other, and the PI short fibers have a relatively smooth and clean surface (Figure 2c,d). It can be clearly observed that the wall of the PI/PAN@Co^{2+} sponge is a porous network structure with micron-scale pores (4–30 μm) formed by percolation of fibers. This porous network structure provides amount of growth sites and reaction space for ZIF-67 formation, indicating its excellent performance as a carrier. The energy dispersive spectrometer (EDS) spectrum of PI/PAN/Co^{2+} sponge proves that Co^{2+} was successfully attached to the surface of PI short fibers and dispersed uniformly (Figure 2e–h). This provides lots of nucleation sites for the growth of ZIF-67. The honeycomb porous network structure of PI/PAN@Co^{2+} sponge was maintained after in situ growth of ZIF-67 (Figure 2j). The surface of PI short fibers is completely covered by lots of ZIF-67 particles (Figure 2k,l). The in situ growth of ZIF-67 on the PI short fiber enables the internal active sites in the ZIF-67 structure to be well preserved. The nanopores of the ZIF-67 itself, the micropores between the cross-linked PI short fibers, and the macroscopic and regular honeycomb macropores of the sponge form a 3D structure of multilevel and hierarchical macro–micropores. This structure can not only expose the active site of ZIF-67 to promote the activation of PMS, but also facilitate the intermolecular mass transfer in the solution to accelerate the degradation of the dye.

We used X-Ray diffraction (XRD) to analyze the crystal properties of PI/PAN and PI/PAN@ZIF-67 sponges, as shown in **Figure 3**a. For the PI/PAN sponge, 2θ at 17.5° corresponding to the (0 0 1) has a broad characteristic diffraction peak.[21] The peaks at 7.4°, 10.5°, 12.9°, 14.8°, 16.6°, and 18.2° belong

Figure 1. Preparation of the PI/PAN@ZIF-67 sponge: Co^{2+} comes from $Co(NO_3)_2 \cdot 6H_2O$; 2-MeIm is 2-methylimidazole.

2300218 (2 of 9)
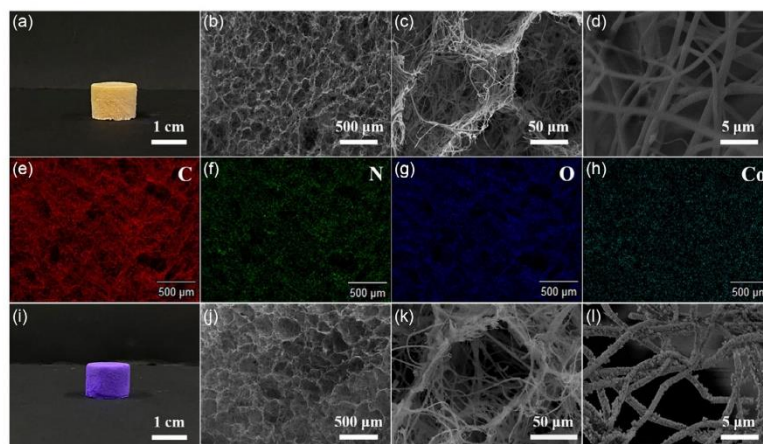
Figure 2. The photo of a) PI/PAN@Co^{2+} sponge and i) PI/PAN@ZIF-67 sponge, b–d) SEM images of PI/PAN@Co^{2+} sponge, e–h) EDS spectrum of PI/PAN@Co^{2+} sponge, and j–l) SEM images of PI/PAN@ZIF-67 sponge.
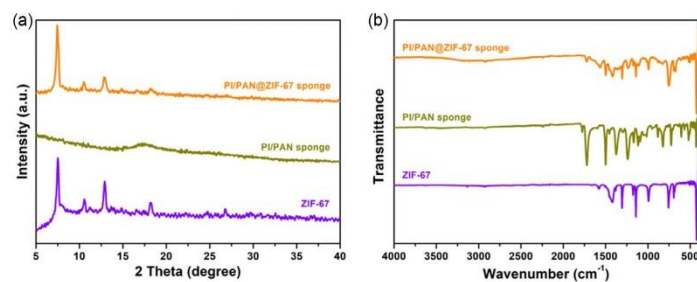
Figure 3. a) The XRD patterns of ZIF-67 powder, PI/PAN sponge, and PI/PAN@ZIF-67 sponge; b) FT-IR spectra of ZIF-67, PI/PAN sponge, and PI/PAN@ZIF-67 sponge.

to the (011), (0 0 2), (11 2), (0 0 2), (0 1 3), and (2 2 2) crystalline planes of ZIF-67.[13a] In the XRD pattern of PI/PAN@ZIF-67 sponge, the characteristic diffraction peaks of PI/PAN and ZIF-67 could be well confirmed. This indicates the successful preparation of PI/PAN@ZIF-67 sponges.

The Fourier transform infrared (FT-IR) spectrum of the PI/PAN@ZIF-67 sponge is shown in Figure 3b. The characteristic stretching bands at 425, 992, and 1570 cm^{-1} are attributed to the Co—N, C—N, and C=N of ZIF-67.[22] The peak at 1364 cm^{-1} is the C—N stretching of the PI imide ring; 1715 and 1779 cm^{-1} are the symmetric and asymmetric stretching vibration peaks of C=O in the PI imide ring, respectively.[23] 2240 cm^{-1} is attributed to the C≡N stretching vibration peak in PAN.[24]

The mechanical properties and shape recovery ability of the sponge are particularly important for any practical use, and they

were evaluated by cyclic compression experiments. **Figure 4**a,b shows the cyclic compressive stress–strain curves of PI/PAN and PI/PAN@ZIF-67 sponges, respectively. It can be found that the compressive strength of PI/PAN is only 5.0 kPa (50% strain), and the sponge height is compressed by about 25.8% after 50 cycles of compression, indicating that the internal structure has undergone serious collapse. The compressive strength of the PI/PAN@ZIF-67 sponge was 28.1 kPa (50% strain), and the height decreased only by 9.9% after 300 cycles of compression. This is due to the fact that the PI/PAN@ZIF-67 sponge consists of two parts: the soft PI short fibers and the hard ZIF-67. The hard ZIF-67 grown on the surface of PI short fibers in situ can significantly improve the mechanical properties of PI/PAN@ZIF-67 sponge and ensure its structural stability. In addition, the 0.1 g PI/PAN@ZIF-67 sponge can withstand

2300218 (3 of 9)
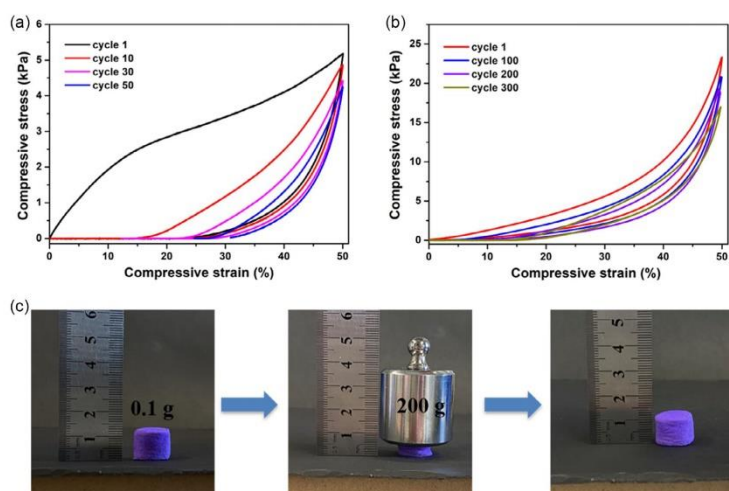
Figure 4. Cyclic compressive stress–strain curves at 50% strain for a) PI/PAN sponge, b) PI/PAN@ZIF-67 sponge, an c) compressive capacity of PI/PAN@ZIF-67 sponge.

a weight of 200 g without collapsing (Figure 4c), further demonstrating its excellent robustness.

Using Rh B as a typical example, we explored the potential of PI/PAN@ZIF-67 sponge as a catalyst in activating PMS for the degradation of organic dyes. **Figure 5** shows the degradation of Rh B under different catalytic systems. To rule out the possible adsorption effect of the sponge in the removal of Rh B from the aqueous solution, we tested the change in the dye concentration
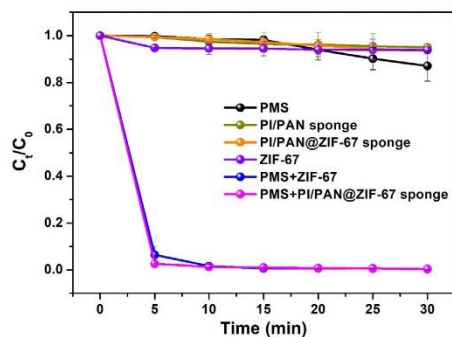
Figure 5. Plots of C_t/C_0 versus time for studying the degradation of Rh B under different conditions. Reaction conditions: Rh B concentration = 50 mg L^{-1}, PMS concentration = 1.5 mM, catalyst amount = 100 mg L^{-1}, pH = 7, temperature = 25 °C.

after putting PI/PAN sponge, PI/PAN@ZIF-67 sponge, and ZIF-67 in the Rh B solution, respectively. The results showed a small decrease (4.9%, 6.2%, and 5.2%, respectively) in Rh B concentration after 30 min as determined by UV–vis spectrophotometer (the concentration of Rh B was evaluated at a wavelength of 555 nm). A Rhodamine solution with only PMS (no sponge) showed 12.9% of Rh B degradation. This indicates that without the activation by a catalyst, PMS cannot effectively degrade dyes. However, when PMS was activated by PI/PAN@ZIF-67 sponge, the Rh B dye was degraded up to 97.4% within 5 min and completely degraded within 30 min. These results indicate that PI/PAN@ZIF-67 sponge can efficiently activate PMS. In addition, we also studied the degradation of Rh B in the presence of ZIF-67 particles and PMS, and the results showed that 93.6% of Rh B degraded within 5 min. This shows that in comparison to ZIF-67 powder, the degradation effect of PI/PAN@ZIF-67 sponge is not compromised. In addition, the degradation kinetics of Rh B conform to the pseudo-first-order rate law-ln $C_t/C_0 = kt$, and the kinetic rate is shown in Figure S3, Supporting Information.

Dye solution of different concentrations (from 25 to 100 mg L^{-1}) was used to study the degradation by PI/PAN@ZIF-67 sponge-activated PMS (**Figure 6**a). When the initial concentration of the dye was reduced from 100 to 25 mg L^{-1}, the degradation of Rh B within 5 min increased from 68.8% to 100%. It is worth mentioning that when the dye concentration is 25 mg L^{-1}, the dye can be completely degraded within 20 s as shown in Figure S4, Supporting Information. However, when the dye concentration was 20 mg L^{-1} or below, the degradation was immediate. The degradation kinetics could not be followed due to the very fast rate of degradation for
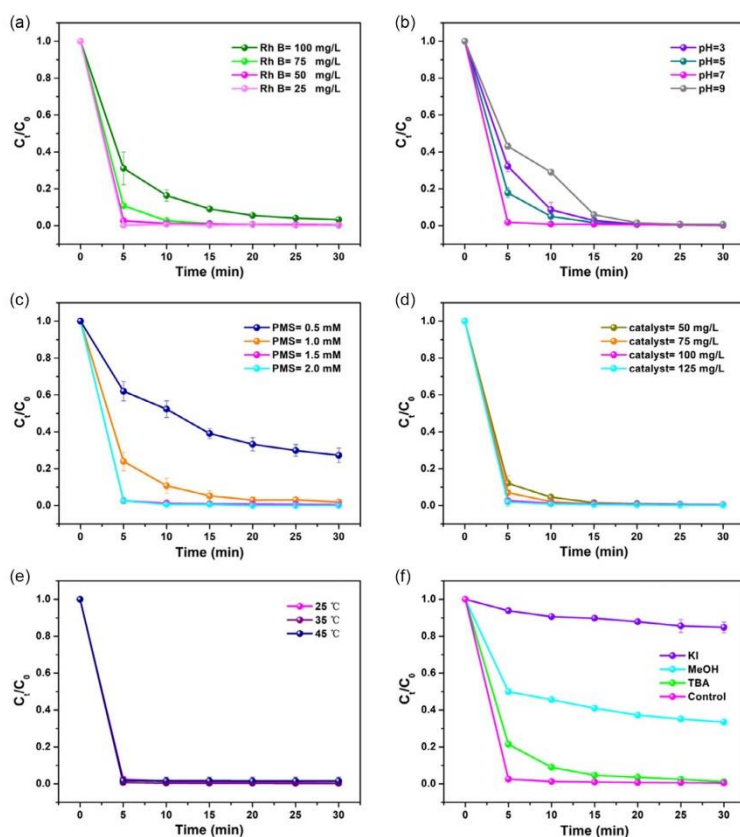
Figure 6. Plots of C_t/C_0 versus time for studying the effect of a) the dye (Rh B) concentration, b) pH, c) the concentration of PMS, d) the dosage of catalyst (PI/PAN@ZIF-67 sponge), e) temperature, and f) radical scavengers on the Rh B degradation. The data for (a) were collected using PMS concentration = 1.5 mM, catalyst amount = 100 mg L^{-1}, pH = 7, temperature = 25 °C. The data for (b) were collected using Rh B solution concentration = 50 mg L^{-1}, PMS concentration = 1.5 mM, catalyst amount = 100 mg L^{-1}, and temperature = 25 °C. The data for (c) were collected using Rh B solution concentration = 50 mg L^{-1}, catalyst amount = 100 mg L^{-1}, pH = 7, temperature = 25 °C. The data for (d) were collected using Rh B solution concentration = 50 mg L^{-1}, PMS concentration = 1.5 mM, PH = 7, and temperature = 25 °C. The data for (e) were collected using Rh B solution = 50 mg L^{-1}, PMS concentration = 1.5 mM, catalyst mount = 100 mg L^{-1}, pH = 7. The data for (f) were collected using Rh B solution concentration = 50 mg L^{-1}, PMS concentration = 1.5 mM, catalyst amount = 100 mg L^{-1}, pH = 7 and temperature = 25 °C.

concentrations below 20 mg L^{-1}. Therefore, 50 mg L^{-1} dye concentration was chosen as a benchmark for further experiments.

pH of the solution can have a significant effect on the degradation process. Figure 6b shows the effect of different pH (3.0–9.0) values on the degradation of dye by PI/PAN@ZIF-67 sponges. When pH = 3.0, only 67.8% of Rh B degraded within 5 min. This may be because, under acidic conditions, H$^+$ makes HSO$_5^-$ more stable, which inhibits the formation of free radicals and reduces the degradation rate.[25] When pH = 5.0, 82.1% of

Rh B was degraded within 5 min, which was close to that of pH = 7.0. However, when pH = 9.0, only 56.9% of Rh B could be degraded within 5 min. Under alkaline conditions, PMS self-decomposes, and the content of free radicals generated therefore decreases slowing down the degradation of dyes.[26] But fortunately, the degradation of Rh B can be as high as more than 99% under different pH values within 30 min. This indicated that PI/PAN@ZIF-67 sponge can activate PMS to degrade organic pollutant dyes in a wide pH range. When the pH is

3.0, 5.0, 7.0, and 9.0, the rate constant K values for degradation are 0.24, 0.30, 0.47, and 0.09 min^{-1}, respectively (Figure S5, Supporting Information).

As the main source of free radicals, the added amount of PMS is very important in the degradation process of dyes. The effect of PMS content on the degradation of Rh B is shown in Figure 6c. When the content of PMS was 0.5 mM, only 37.9% of the Rh B was degraded within 5 min, and only 72.7% of the dye was degraded within 30 min. However, when the content of PMS was increased to 1 mM, the degradation of dye increased to 76.1% within 5 min and Rhodamine degradation reached 98.1% within 30 min, which significantly improved the degradation situation. The results showed that an optimum amount of PMS is required so that sufficient free radicals are generated making the degradation occur effectively. This shows that the content of added PMS is very important to the degradation of the dye. Furthermore, when the content of PMS continued to increase to 2 mM, there was little difference compared to the time when PMS was 1.5 mM. This is because the content of the PI/PAN@ZIF-67 sponge was fixed, and the active sites of the PI/PAN@ZIF-67 sponge for activating PMS had reached saturation. Even if the content of PMS continues to increase, the catalyst cannot continue to activate the excess PMS. Therefore, the PMS content of 1.5 mM is the best choice. This result is also reflected in the kinetics. When the PMS content increases from 0.5 to 2.0 mM, the k values were 0.06, 0.22, 0.44 and 0.44 min^{-1}, respectively (Figure S6, Supporting Information).

Figure 6d shows the effect of the amount of catalyst (sponge) on the degradation of dyes. The degradation of the dye increased from 87.8% to 97.4% within 5 min on increasing the amount of catalyst from 50 to 100 mg L^{-1}. The k value increased from 0.31 to 0.44 min^{-1} (Figure S7, Supporting Information). On further increase in the catalyst content to increase to 125 mg L^{-1}, 98% of the Rh B was degraded within 5 min ($k = 0.44$ min^{-1}). Compared with the catalyst addition of 100 mg L^{-1}, there is no obvious increase. This suggests that at high catalyst dosage, the efficiency of PMS to utilize the excess active sites at the PI/PAN@ZIF-67 sponge to generate free radicals is limited. Therefore, 100 mg L^{-1} catalyst is the optimal input amount.

In addition, we also examined the effect of PI/PAN@ZIF-67 sponge-activated PMS on dye degradation at different temperatures (Figure 6e). There was no significant difference in the % degradation observed on raising the temperature from 25 to 45 °C (Figure S8, Supporting Information).

To understand the catalytic process of PI/PAN@ZIF-67 sponge, we explored the reaction mechanism. In previous reports, it has been proved that Co ions in ZIF-67 can undergo cyclic conversion in divalent and trivalent states, activating PMS to produce sulfate and hydroxide radicals, which have higher oxidation-reduction potential, can eventually oxidize the dye to water and carbon dioxide as in Equation (S1)–(S4), Supporting Information.[17] We conducted a series of reactive oxygen species (ROS) capture experiments to find out which radical is mainly taking part in the degradation process. It is known that potassium iodide (KI) can effectively capture both sulfate and hydroxide radicals, whereas methanol (MeOH) is selective in capturing sulfate radicals. On the other hand, tert-butanol (TBA) traps hydroxide radicals.[15] As shown in Figure 6f, when KI was added to the catalytic system, only 15.1% Rh B was degraded within

30 min. As KI captures both types of radicals, it could not be said which radical played the major role in the degradation process. When methanol was added to the catalytic system, only 66.5% of the dye was degraded within 30 min. When TBA was added, the Rh B can be degraded up to 99%. The addition of TBA quencher has little effect on the degradation of dye. The results indicated that sulfate radical played major role in the degradation of Rh B. The mechanism of activating PMS by PI/PAN@ZIF-67 sponge to generate free radical degradation of Rh B is shown in Figure S9, Supporting Information. The degradation mechanism of Rh B by the attack of ROS generating several different intermediates through de-ethylation, followed by deamination, dealkylation, decarboxylation, and chromophore cleavage to form other smaller molecule intermediates, is described in the literature. Finally, these small molecules are further mineralized by ROS into H_2O and CO_2.[27]

For any practical sustainable application, it is important that the catalysts are stable and reusable. **Figure 7** shows the degradation efficiency after reusing the regenerated PI/PAN@ZIF-67 sponge. After the first degradation cycle, the PI/PAN@ZIF-67 sponge only needs to be removed from the reaction solution with tweezers. There is no need for elaborate centrifugation or filtration. It is very simple and convenient. Then wash it three times with water and methanol respectively. After vacuum drying at 80 °C, it is directly used for the next cycle. As a result, after five cycles of use, degradation of the dye was negligibly reduced by only 3%. The XRD patterns of the PI/PAN@ZIF-67 sponge before and after use are also shown in Figure S10, Supporting Information. Through comparison, it can be found that the diffraction peaks of the used PI/PAN@ZIF-67sponge and fresh PI/PAN@ZIF-67 sponge are basically consistent, indicating that the PI/PAN@ZIF-67 sponge exhibits good stability during the degradation process of Rh B.

In addition, in order to further expand the application of PI/PAN@ZIF-67 sponge in real-life application, we constructed the PI/PAN@ZIF-67 sponge as a simple filtration device to evaluate its performance for the continuous treatment of dye wastewater solutions (**Figure 8**a). Thanks to the multilevel hierarchical porous structure of the PI/PAN@ZIF-67 sponge, the Rh B
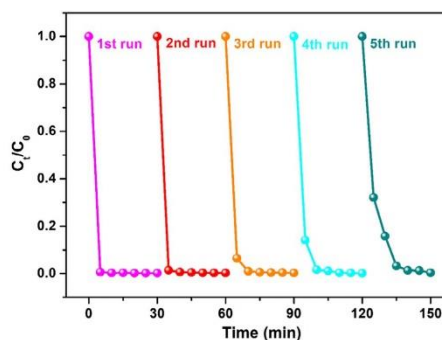
Figure 7. Reusability test of PI/PAN@ZIF-67 sponge.

2300218 (6 of 9)
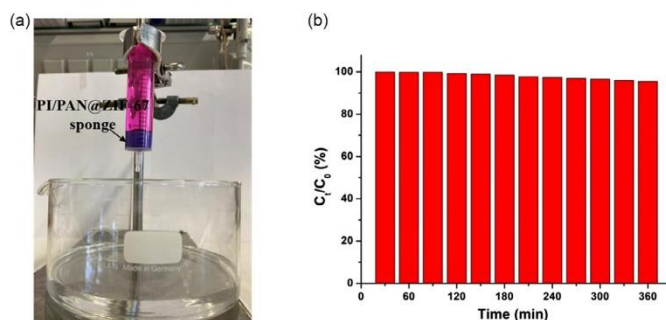
Figure 8. a) Photograph of the assembly showing degradation of Rh B by filtration process. PI/PAN@ZIF-67 sponge was fitted in a syringe for use as a catalytic filter to degrade Rh B. b) Continuous degradation experiment of Rh B with PI/PAN@ZIF-67 sponge as a filter. Reaction condition: pH = 7.0, 25 °C, dye (Rh B) concentration = 25 mg L^{-1}, PMS concentration = 1.5 mM.

solution can quickly pass through the PI/PAN@ZIF-67 sponge under self-gravity and its catalytic action provided a clear solution after passing through the sponge. The removal efficiency of Rh B is still as high as 95% after the filter device continuously treats the Rh B solution for 6 h (as shown in Figure 8b, Video 1, Supporting Information). As a result, the PI/PAN@ZIF-67 sponge can also be used as a catalytic filter to activate PMS for the degradation of dyes which makes it promising for scaling up in the future.

Although the present work was carried out using Rh B as an exemplary dye, our system should be valid for the degradation of other dyes, such as methylene blue, acid yellow-17 (AY), and orange II (AO7) that are known to undergo degradation by PMS activation.[28]

3. Conclusion

In this work, we prepared PI/PAN@ZIF-67 sponges with high ZIF-67 loading (up to 72 wt%), multilayered, and hierarchical macro–microporous honeycomb structure by in situ growth of ZIF-67 on the surface of PI short fibers. The 3D porous framework and high ZIF-67 loading provided the sponge with excellent mechanical properties and compression resistance, making the PI/PAN@ZIF-67 sponge reusable for practical use. The PI/PAN@ZIF-67 sponge exhibited high efficiency in the removal of organic dye by PMS activation. We explored that the optimal conditions for PI/PAN@ZIF-67 sponge to activate PMS to degrade Rh B organic dye were pH = 7, PMS = 1.5 mM, catalyst (PI/PAN@ZIF-67 sponge) = 100 mg L^{-1}, and the initial concentration of dye was 50 mg L^{-1}. Also, filtration experiments using PI/PAN@ZIF-67 sponge as a catalytic filter were very promising. This study opens new opportunities to explore MOF-based materials in the form of porous robust 3D sponges for water remediation. Furthermore, this strategy can also be applied to prepare monolithic materials of other types of MOFs and is expected to be suitable for other applications as well.

4. Experimental Section

Materials: PAN ($M_w = 80\,000$) and PI electrospun nonwovens were provided by Jiangxi Xiancai Nanofiber Technology Co., Ltd; cobaltous nitrate hexahydrate (Co(NO$_3$)$_2$·6H$_2$O) and KI were purchased from Alfa Aesar. 2-MeIM and Oxone (2KHSO$_5$·KHSO$_4$·K$_2$SO$_4$) were brought from Thermo Fisher Scientific. Rh B was purchased from Sigma–Aldrich. DMSO ($\geq$99.7%), MeOH ($\geq$99.7%), and TBA ($\geq$99.7%) were supplied by Fisher Chemical company. All reagents were used without further purification.

Preparation of PI Short Fibers: PI short fibers were prepared by cutting PI electrospun nonwoven through a mechanical cutting process. Briefly, 10 g of PI electrospun nonwovens were first cut with scissors into small pieces and put into 1 L of solvent consisting of isopropanol/water (v/v = 3/1). The mixture was cooled using liquid nitrogen and then cut with a mechanical cutter (Robot Coupe Blixer 4, Rudolf Lange GmbH & Co. KG) at 3000 rpm for 25 h. Then, short PI fibers were filtered and freeze-dried for 24–36 h.

Preparation ZIF-67 Particles: ZIF-67 particles were prepared based on the literature that has been reported with a little modification.[29] In brief, 0.145 g cobaltous nitrate hexahydrate was dissolved in 10 mL of Milli-Q water (designated as solution A); 2.37 g 2-methylimidazole was dissolved in 10 mL of Milli-Q water (designated as solution B). Then solution B was quickly poured into solution A and stirred at room temperature for 24 h to obtain purple particles. The purple particles were collected by centrifugation, washed three times with water and methanol, respectively, and finally, dried at 80 °C in the oven to obtain ZIF-67 particles.

Preparation of Template PI/PAN Sponge: 0.5 g PI short fibers and 0.5 g PAN were dissolved in 12.5 mL DMSO in a 25 mL flask. The mixture was cooled to −20 °C in a refrigerator for 2 h. Afterward, it was freeze-dried to get the PI/PAN sponge.

Preparation of PI/PAN@ZIF-67 Sponge: In the first step, a PI/PAN@Co^{2+} sponge was prepared using the same method as described above for PI/PAN sponge. Briefly, 0.1 g PI short fibers, 0.1 g PAN, and 0.1 g Co(NO$_3$)$_2$·6H$_2$O were dissolved in 25 mL DMSO in a 50 mL flask. Then free-drying after cooling to −20 °C provided PI/PAN@Co^{2+} sponge. 0.145 g of Co nitrate was dissolved in 10 mL of Mili-Q water, which was designated as solution A. Subsequently, the PI/PAN@Co^{2+} sponge was placed in solution A and allowed to stand for 2 h. 2.32 g of 2-methylimidazole was dissolved in Mili-Q 10 mL of water (designated as solution B). Afterward, solution B was quickly poured into solution A. The mixed solution with the sponge inside was stirred at room temperature for 24 h to

2300218 (7 of 9)

give a purple sponge. Finally, the sponge was washed with water and methanol several times to remove excess of unreacted materials and dried at 80 °C to obtain PI/PAN@ZIF-67 sponge.

Catalytic Batch Experiments: All degradation experiments were carried out in 150 mL glass containers with magnetic stirring at 300 rpm. The pH value of the solution was adjusted by adding 0.1 M HCl and 0.1 M NaOH, respectively. Typically, a known amount of PI/PAN@ZIF-67 sponge was added to 100 mL of 50 mg L^{-1} Rh B solution. Subsequently, a certain amount of PMS was added to the solution and the time was noted. Every 5 min 1 mL sample was pipetted out, quenched with 0.5 mL methanol. Then, the degradation of the Rh B was measured using a UV–vis spectrophotometer at a wavelength of 555 nm. The degradation efficiency of Rh B was calculated according to Equation (1)

$$R\% = \frac{100\% \times (C_0 - C_t)}{C_0} \tag{1}$$

where R is the degradation efficiency of Rh B (%), and C_0 and C_t are the concentrations of Rh B at time 0 and time t (mg L^{-1}), respectively. And the kinetics of Rh B degradation process was investigated according to the pseudo first-order kinetics Equation (2)

$$-\ln(C_t/C_0) = kt \tag{2}$$

in which k is a rate constant and t is the degradation time (min). Besides, all batch experiments were repeated, and the average value with the standard deviation was presented for the results.

Reusability of Sponges: After the initial degradation experiment, the PI/PAN@ZIF-67 sponge was taken out from the reaction solution using tweezers, followed by simple cleaning with water and methanol. It was directly used for the next cycle after drying.

Continuous Flow Catalytic Test Using Sponge as Catalytic Filter: The sponge was also tested as a catalytic filter. For this, the PI/PAN@ZIF-67 sponge with a diameter of 2.5 cm and a height of 1.5 cm was loaded in a 20 mL plastic syringe, and the Rh B solution (25 mg L^{-1}) containing PMS (1.5 mM) was filtered under the action of gravity, during which the Rh B solution was continuously added to ensure that it can be continuously filtered, and the filtered solution was collected and analyzed to determine the concentration as described above.

Supporting Information

Supporting Information is available from the Wiley Online Library or from the author.

Acknowledgements

Conflict of Interest

The authors declare no conflict of interest.

Data Availability Statement

The data that support the findings of this study are available in the Supporting Information of this article.

2300218 (8 of 9)

[1] a) J. Wang, M. Gao, T. Shen, M. Yu, Y. Xiang, J. Liu, *J. Hazard. Mater.* **2019**, *366*, 501; b) D. Yaseen, M. Scholz, *Int. J. Environ. Sci. Technol.* **2019**, *16*, 1193; c) B. Zhu, H. Cheng, J. Ma, Y. Qin, Y. Kong, S. Komarneni, *Mater. Lett.* **2020**, *261*, 127099; d) Y. Lv, C. Zhang, A. He, S. J. Yang, G. P. Wu, S. B. Darling, Z. K. Xu, *Adv. Funct. Mater.* **2017**, *27*, 1700251.

[2] a) Z. H. Zhu, Y. Liu, C. Song, Y. Hu, G. Feng, B. Z. Tang, *ACS Nano* **2021**, *16*, 1346; b) D. Lan, H. Zhu, J. Zhang, S. Li, Q. Chen, C. Wang, T. Wu, M. Xu, *Chemosphere* **2022**, *293*, 133464; c) P. Chanikya, P. Nidheesh, D. S. Babu, A. Gopinath, M. S. Kumar, *Sep. Purif. Technol.* **2021**, *254*, 117570; d) Y. Chen, D. Zhao, T. Sun, C. Cai, Y. Dong, *J. Environ. Chem. Eng.* **2023**, *11*, 110353.

[3] a) Y. Kang, J. Jang, S. Kim, J. Lim, Y. Lee, I. S. Kim, *ACS Appl. Mater. Interfaces* **2020**, *12*, 36148; b) F. Yang, M. Du, K. Yin, Z. Qiu, J. Zhao, C. Liu, G. Zhang, Y. Gao, H. Pang, *Small* **2022**, *18*, 2105715; c) Z. Yin, C. Cui, H. Chen, X. Yu, W. Qian, *Small* **2020**, *16*, 1902301; d) G. Wu, Q. Liu, J. Wang, S. Xia, X. Huang, J. Han, W. Xing, *Colloids Surf. A Physicochem. Eng. Asp.* **2022**, *653*, 130048.

[4] a) J. Rostami, T. Benselfelt, L. Maddalena, C. Avci, F. A. Sellman, G. Cinar Ciftci, P. A. Larsson, F. Carosio, F. Akhtar, W. Tian, *Adv. Mater.* **2022**, *34*, 2204800; b) F. Haase, P. Hirschle, R. Freund, S. Furukawa, Z. Ji, S. Wuttke, *Angew. Chem. Int. Ed.* **2020**, *59*, 22350.

[5] X. Li, B. Wang, Y. Cao, S. Zhao, H. Wang, X. Feng, J. Zhou, X. Ma, *ACS Sustainable Chem. Eng.* **2019**, *7*, 4548.

[6] a) R. Guo, X. Cai, H. Liu, Z. Yang, Y. Meng, F. Chen, Y. Li, B. Wang, *Environ. Sci. Technol.* **2019**, *53*, 2705; b) F. Ahmadijokani, H. Molavi, A. Bahi, R. Fernández, P. Alaee, S. Wu, M. Arjmand, *Adv. Funct. Mater.* **2022**, *32*, 2207723.

[7] M. Peydayesh, T. Suta, M. Usuelli, S. Handschin, G. Canelli, M. Bagnani, R. Mezzenga, *Environ. Sci. Technol.* **2021**, *55*, 8848.

[8] a) V. K. Sharma, M. Feng, *J. Hazard. Mater.* **2019**, *372*, 3; b) A. Yusuf, A. Giwa, J. O. Eniola, H. K. Amusa, M. R. Bilad, *J. Hazard. Mater.* **2022**, 100108; c) L. Zhu, J. Ji, J. Liu, J. Zhang, *Angew. Chem. Int. Ed.* **2020**, *132*, 14072; d) J. Wang, Z. Zhang, F. Wu, W. Sun, F. Wang, J. Han, G. Wu, *Opt. Mater.* **2023**, *143*, 114156.

[9] a) X. Du, M. Zhou, *Chem. Eng. J.* **2021**, *403*, 126346; b) Z. Xiong, Y. Jiang, Z. Wu, G. Yao, B. Lai, *Chem. Eng. J.* **2021**, *421*, 127863; c) U. Ushani, X. Lu, J. Wang, Z. Zhang, J. Dai, Y. Tan, S. Wang, W. Li, C. Niu, T. Cai, *Chem. Eng. J.* **2020**, *402*, 126232.

[10] a) A. Hassani, J. Scaria, F. Ghanbari, P. J. Nidheesh, *Environ. Res.* **2022**, 114789; b) W.-D. Oh, Z. Dong, T.-T. Lim, *Appl. Catal. B* **2016**, *194*, 169; c) L. Ismail, C. Ferronato, L. Fine, F. Jaber, J.-M. Chevelon, *Appl. Catal. B* **2017**, *201*, 573; d) G. Tai, G. Li, Z. Cai, Y. Pan, J. Han, J. Shi, G. Wu, *Colloids Surf. A Physicochem. Eng. Asp.* **2023**, 131925.

[11] a) C. Wang, J. Kim, V. Malgras, J. Na, J. Lin, J. You, M. Zhang, J. Li, Y. Yamauchi, *Small* **2019**, *15*, 1900744; b) G. Li, Z. Cai, K. Su, Y. Zhao, Y. Zhu, J. Han, G. Wu, *Colloids Surf. A Physicochem. Eng. Asp.* **2023**, *677*, 132353.

[12] a) J. Guo, Y. Qin, Y. Zhu, X. Zhang, C. Long, M. Zhao, Z. Tang, *Chem. Soc. Rev.* **2021**, *50*, 5366; b) G. Cai, P. Yan, L. Zhang, H.-C. Zhou, H.-L. Jiang, *Chem. Rev.* **2021**, *121*, 12278; c) Y. Ye, L. Gong, S. Xiang, Z. Zhang, B. Chen, *Adv. Mater.* **2020**, *32*, 1907090;

d) R. Banerjee, A. Phan, B. Wang, C. Knobler, H. Furukawa, M. O'Keeffe, O. M. Yaghi, *Science* **2008**, *319*, 939;

[13] a) X.-W. Zhang, M.-Y. Lan, F. Wang, X.-H. Yi, C.-C. Wang, *J. Environ. Chem. Eng.* **2022**, *10*, 107997; b) M. Zhang, C. Xiao, C. Zhang, J. Qi, C. Wang, X. Sun, L. Wang, Q. Xu, J. Li, *ACS Est. Eng.* **2021**, *1*, 249.

[14] a) W. Ren, J. Gao, C. Lei, Y. Xie, Y. Cai, Q. Ni, J. Yao, *Chem. Eng. J.* **2018**, *349*, 766; b) A. Du, H. Fu, P. Wang, C. Zhao, C.-C. Wang, *J. Hazard. Mater.* **2022**, *426*, 128134.

[15] C. Wang, P. Cheng, Y. Yao, Y. Yamauchi, X. Yan, J. Li, J. Na, *J. Hazard. Mater.* **2020**, *392*, 122164.

[16] L. Peng, X. Gong, X. Wang, Z. Yang, Y. Liu, *RSC Adv.* **2018**, *8*, 26377.

[17] C.-H. Wu, W.-C. Yun, T. Wi-Afedzi, K.-Y. Lin, *J. Colloid. Interface Sci.* **2018**, *514*, 262.

[18] a) X. Jia, M. Peydayesh, Q. Huang, R. Mezzenga, *Small* **2022**, *18*, 2105502; b) K. Ma, Y. H. Cheung, K. O. Kirlikovali, H. Xie, K. B. Idrees, X. Wang, T. Islamoglu, J. H. Xin, O. K. Farha, *Adv. Mater.* **2023**, 2300951.

[19] a) Q. Gao, T. Tran, X. Liao, S. Rosenfeldt, C. Gao, H. Hou, M. Retsch, S. Agarwal, A. Greiner, *ACS Appl. Mater. Interfaces* **2022**, *14*, 19918; b) S. Jiang, B. Uch, S. Agarwal, A. Greiner, *ACS Appl. Mater. Interfaces*

[20] **2017**, *9*, 32308; c) C. Ding, Y. Du, S. Agarwal, *Adv. Funct. Mater.* **2023**, 2309938.

[20] J. Y. Cheong, L. Benker, J. Zhu, D.-Y. Youn, H. Hou, S. Agarwal, I.-D. Kim, A. Greiner, *Carbon* **2019**, *154*, 363.

[21] C. Ding, M. Breunig, J. Timm, R. Marschall, J. Senker, S. Agarwal, *Adv. Funct. Mater.* **2021**, *31*, 2106507.

[22] Q. Yang, S. Ren, Q. Zhao, R. Lu, C. Hang, Z. Chen, H. Zheng, *Chem. Eng. J.* **2018**, *333*, 49.

[23] C. A. Pryde, *Polym. Chem.* **1989**, *27*, 711.

[24] Y. Du, C. Ding, J. Timm, R. Marschall, S. Agarwal, *Chemcatchem.* **2022**, *14*, e202201040.

[25] K.-Y. A. Lin, H.-A. Chang, *J. Taiwan Inst. Chem. Eng.* **2015**, *53*, 40.

[26] K.-Y. A. Lin, F.-K. Hsu, W.-D. Lee, *J. Mater. Chem. A* **2015**, *3*, 9480.

[27] a) Y. Tian, Y. Wu, Q. Yi, L. Zhou, J. Lei, L. Wang, J. Zhang, *Chem. Eng. J.* **2021**, *425*, 128644; b) F. Wu, C. Zhou, G. Tai, Y. Ma, X. Yang, Y. Pan, G. Wu, *ACS Appl. Nano Mater.* **2023**, *6*, 17814.

[28] a) C. Wang, H. Wang, R. Luo, C. Liu, J. Li, X. Sun, J. Shen, W. Han, L. Wang, *Chem. Eng. J.* **2017**, *330*, 262; b) S. Zhang, M. Zhao, H. Li, C. Hou, M. Du, *Cellulose.* **2021**, *28*, 3585; c) D. Liu, J. Yin, H. Tang, H. Wang, S. Liu, T. Huang, Z. Xie, *Sep. Purif. Technol.* **2021**, *279*, 119755.

[29] J. Qian, F. Sun, L. Qin, *Mater. Lett.* **2012**, *82*, 220.

WILEY-VCH

Supporting Information

Sustainable Hierarchically Porous Reusable Metal–Organic Framework Sponge as a Heterogeneous Catalyst and Catalytic Filter for Degradation of Organic Dyes

Yingying Du, Chenhui Ding, Seema Agarwal*

Y. Du, C. Ding, Prof. S. Agarwal
Macromolecular Chemistry and Bavarian Polymer Institute
University of Bayreuth
Universitätsstrasse 30, 95440 Bayreuth, Germany
E-mail: agarwal@uni-bayreuth.de

Characterization and instruments

The morphology and structure of the samples were investigated by scanning electron microscopy (SEM, FEI Quanta FEG 250) with a Zeiss LEO 1530, operating at an acceleration voltage of 3 kV employing an Everhart-Thornley secondary electron detector. The X-ray diffraction (XRD) patterns of all the samples were obtained on a Bragg-Brentano type diffractometer (XPERT-PRO, PANalytical B.V.) with Cu-Kα X-ray radiation ($\lambda = 1.540598$ Å), and each XRD pattern was scanned over a range of $2\theta = 2°$ to $40°$ at a rate of $0.5°$ min^{-1}. The functional groups and chemical structures of all the samples were performed using Fourier transform infrared spectra (FT-IR). The FT-IR spectroscopy was measured using a spectrometer (Digilab Excalibur FTS-3000) in the wavelength range of 4000 cm^{-1} to 400 cm^{-1}. The degradation of Rhodamine B was evaluated using a UV-vis spectrophotometer (Jasco Spectrometer V-670) in the range of 480-650 nm (scan speed 200 nm min^{-1}). The characteristic peak of Rhodamine B in UV-vis spectrophotometer is at 555 nm. The mechanical properties of the PI/PAN sponge and PI/PAN@ZIF-67 sponge were investigated by the tensile tester. machine (ZwickiLine Z0.5; BT1-FR0.5TN.D14; Zwick / Roell, Germany). The compression testing and cyclic compression testing of the composite sponges at a compression rate of 8 mm min^{-1}.

1

WILEY-VCH
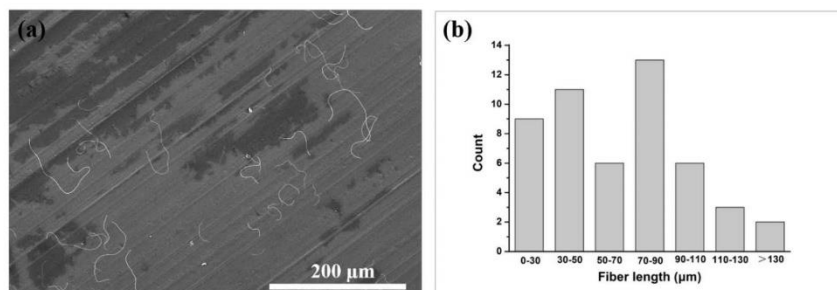
Figure S1. (a) SEM image of PI short fibers. Fibers average diameter (d) = 521 ± 143.0 nm and fibers length (L) = 77 ± 33 μm. (b) Fiber length distribution of the PI short fibers.
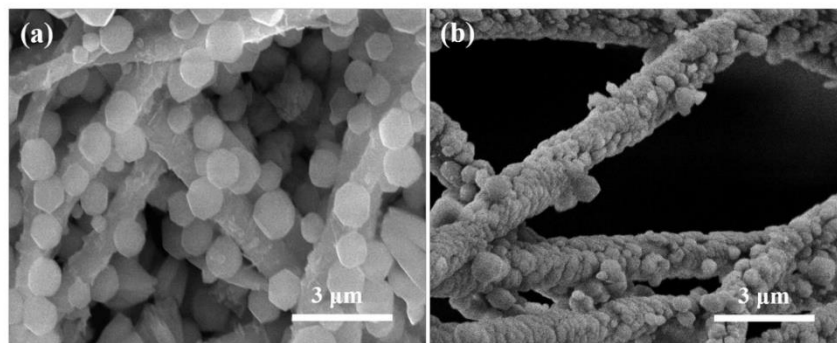
Figure S2. SEM image of PI/PAN@ZIF-67 sponge (a) During synthesis the solution was not stirred (b) During synthesis the solution was stirred.

2
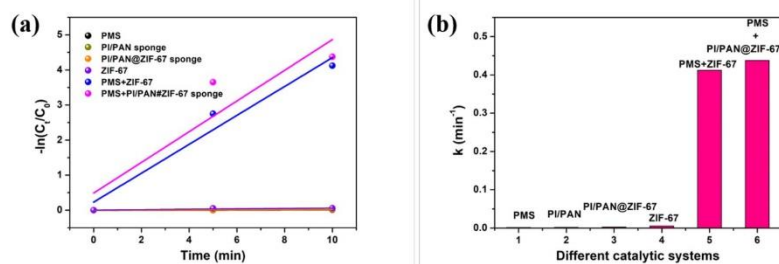
Figure S3. (a) The kinetic rates and (b) the first kinetic constants of Rh B degradation under different catalytic conditions.
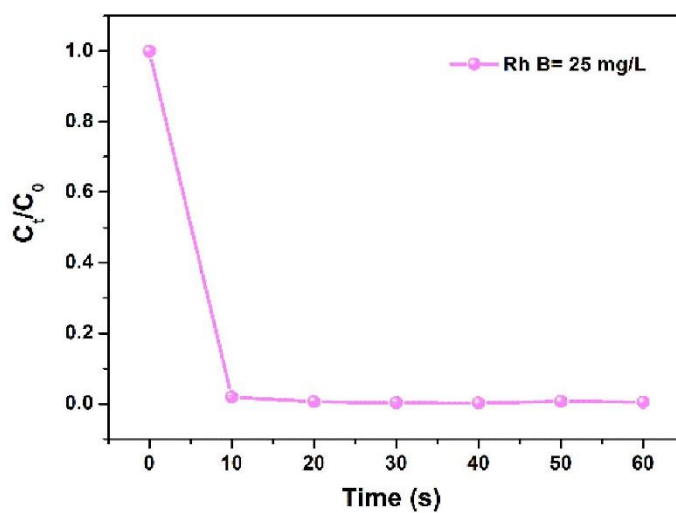
Figure S4. Degradation of Rh B. Reaction condition: Rh B = 25 mg L^{-1}, PMS = 1.5 mM, PI/PAN@ZIF-67 sponge =100 mg L^{-1} , pH=7.0 and temperature =25 °C.

3

WILEY-VCH
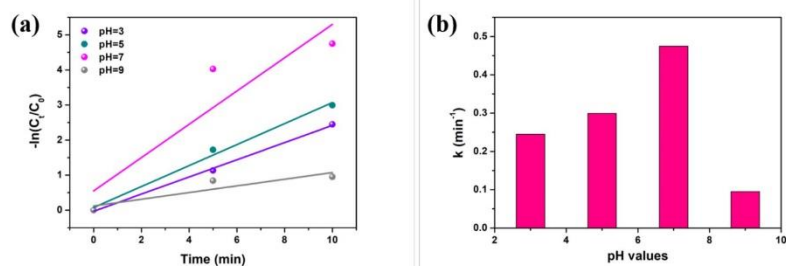
Figure S5. (a) The kinetic rates and (b) the first kinetic constants of Rh B degradation under different pH values.
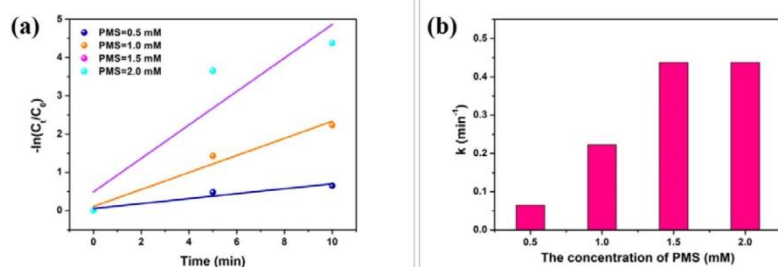
Figure S6. (a) The kinetic rates and (b) the first kinetic constants of Rh B degradation under different concentrations of PMS.

4
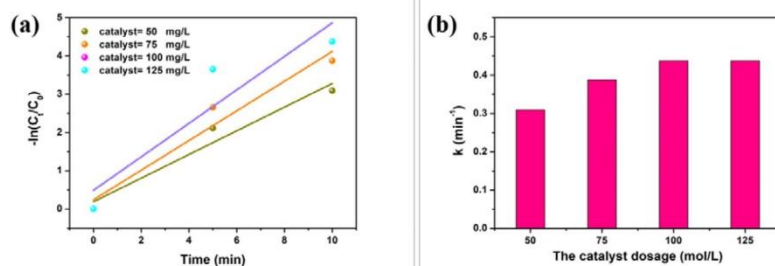
Fig. S7. (a) The kinetic rates and (b) the first kinetic constants of Rh B degradation under different catalyst dosage.
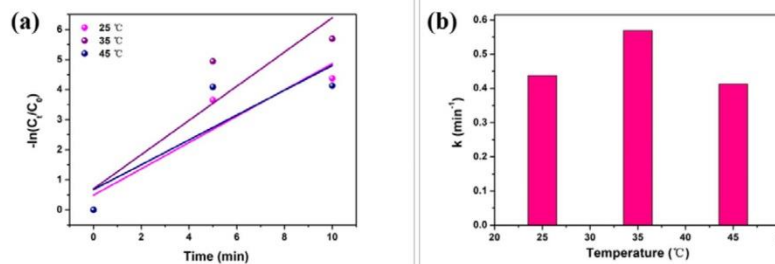
Fig. S8. (a) The kinetic rates and (b) the first kinetic constants of Rh B degradation under different temperatures.

5

154

$$\text{Co}^{2+} + \text{HSO}_5^- \rightarrow \text{Co}^{3+} + \text{SO}_4{}^{\bullet-} + \text{OH}^- \tag{1}$$

$$\text{SO}_4{}^{\bullet-} + \text{OH}^- \rightarrow \cdot\text{OH} + \text{SO}_4{}^{2-} \tag{2}$$

$$\text{Co}^{3+} + \text{HSO}_5^- \rightarrow \text{Co}^{2+} + \text{SO}_4{}^{\bullet-} + \text{H}^+ \tag{3}$$

$$\text{SO4}^{\bullet-} + \cdot\text{OH} + \text{dye} \rightarrow \dots \text{H}_2\text{O} + \text{CO}_2 \tag{4}$$
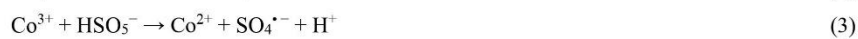
Equation S(1)-S(4). Cyclic transformation of cobalt ion (divalent and trivalent) in ZIF-67 activates PMS to generate sulfate radicals and hydroxide radicals that degrades organic dyes.
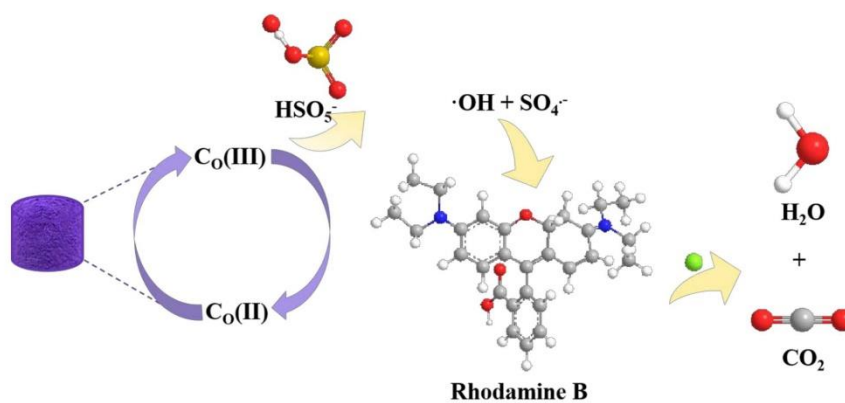
Fig. S9. Schematic diagram of the mechanism of PI/PAN@ZIF-67 sponge to activated PMS to degrade Rhodamine B.

6

155

WILEY-VCH
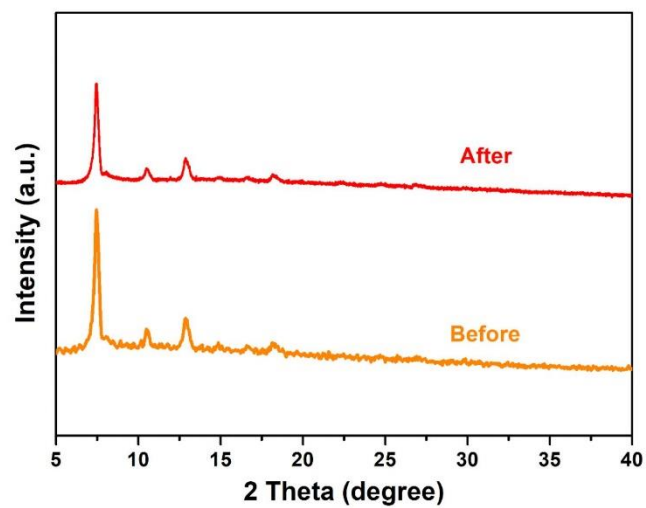
Figure S10. The XRD patterns of PI/PAN@ZIF-67 sponge before and after use.

7

Table S1. The kinetic constant values under different conditions.

Sample/Condition	Kinetic constant (min^{-1})
PMS	0.00158
PI/PAN sponge	0.00263
PI/PAN@ZIF-67 sponge	0.00263
ZIF-67	0.00565
PMS+ZIF-67 particles	0.41227
PMS+ PI/PAN@ZIF-67 sponge	0.43764
pH=3.0	0.24498
pH=5.0	0.29919
pH=7.0	0.47467
pH=9.0	0.09529
PMS content = 0.5 mM	0.06483
PMS content= 1.0 mM	0.22303
PMS content = 1.5 mM	0.43764
PMS content = 2.0 mM	0.43764
Catalyst dosage = 50 mg/L	0.30922
Catalyst dosage = 75 mg/L	0.38776
Catalyst dosage = 100 mg/L	0.43764
Catalyst dosage = 125 mg/L	0.43764
Dye solution = 25 mg/L	0.49879
Dye solution = 50 mg/L	0.43764
Dye solution = 75 mg/L	0.36378
Dye solution = 100 mg/L	0.18084
T= 25 ℃	0.43764
T= 35 ℃	0.56899
T= 45 ℃	0.41308

8

157

158

5. Acknowledgments

atmosphere allows me to work happily every day.

Last but not least, I would also like to thank my family, thanks to them for their tolerance, companionship, and support along the way, which enabled me to better complete my studies. I would also like to thank my special colleague Chenhui Ding. He is not only my colleague but also my husband. As a colleague, I am very grateful for all his help and topic discussions during my doctoral. As a husband, I would like to thank him for his encouragement, support, and companionship in life, which makes my life abroad rich and interesting.

6. Eidesstattliche Versicherungen und Erklärungen

(§ 9 Satz 2 Nr. 3 PromO BayNAT)

Hiermit versichere ich eidesstattlich, dass ich die Arbeit selbstständig verfasst und keine anderen als die von mir angegebenen Quellen und Hilfsmittel benutzt habe (vgl. Art. 97 Abs. 1 Satz 8 BayHIG).

(§ 9 Satz 2 Nr. 3 PromO BayNAT)

Hiermit erkläre ich, dass ich die Dissertation nicht bereits zur Erlangung eines akademischen Grades eingereicht habe und dass ich nicht bereits diese oder eine gleichartige Doktorprüfung endgültig nicht bestanden habe.

(§ 9 Satz 2 Nr. 4 PromO BayNAT)

Hiermit erkläre ich, dass ich Hilfe von gewerblichen Promotionsberatern bzw. -vermittlern oder ähnlichen Dienstleistern weder bisher in Anspruch genommen habe noch künftig in Anspruch nehmen werde.

(§ 9 Satz 2 Nr. 7 PromO BayNAT)

Hiermit erkläre ich mein Einverständnis, dass die elektronische Fassung meiner Dissertation unter Wahrung meiner Urheberrechte und des Datenschutzes einer gesonderten Überprüfung unterzogen werden kann.

(§ 9 Satz 2 Nr. 8 PromO BayNAT)

Hiermit erkläre ich mein Einverständnis, dass bei Verdacht wissenschaftlichen Fehlverhaltens Ermittlungen durch universitätsinterne Organe der wissenschaftlichen Selbstkontrolle stattfinden können.

…………………………………………………………………………….
Ort, Datum, Unterschrift